

Proper Motions, Orbits, and Tidal Influences of Milky Way Dwarf Spheroidal Galaxies

ANDREW B. PACE ¹, DENIS ERKAL ², AND TING S. LI ³

¹*McWilliams Center for Cosmology, Carnegie Mellon University, 5000 Forbes Ave, Pittsburgh, PA 15213, USA*

²*Department of Physics, University of Surrey, Guildford GU2 7XH, UK*

³*Department of Astronomy and Astrophysics, University of Toronto, 50 St. George Street, Toronto ON, M5S 3H4, Canada*

(Received October 11, 2022; Revised October 11, 2022; Accepted October 11, 2022)

Submitted to ApJ

ABSTRACT

We combine *Gaia* EDR3 astrometry with accurate photometry and utilize a probabilistic mixture model to measure the systemic proper motion of 52 dwarf spheroidal (dSph) satellite galaxies of the Milky Way (MW). For the 46 dSphs with literature line-of-sight velocities we compute orbits in both a MW and a combined MW + Large Magellanic Cloud (LMC) potential and identify Car II, Car III, Hor I, Hyi I, Phx II, and Ret II as likely LMC satellites. 40% of our dSph sample has a $> 25\%$ change in pericenter and/or apocenter with the MW + LMC potential. For these orbits, we Monte Carlo sample over the observational uncertainties for each dSph and the uncertainties in the MW and LMC potentials. We predict that Ant II, Boo III, Cra II, Gru II, and Tuc III should be tidally disrupting by comparing each dSph's average density relative to the MW density at its pericenter. dSphs with large ellipticity (CVn I, Her, Tuc V, UMa I, UMa II, UMi, Wil 1) show a preference for their orbital direction to align with their major axis even for dSphs with large pericenters. We compare the dSph radial orbital phase to subhalos in MW-like N-body simulations and infer that there is not an excess of satellites near their pericenter. With projections of future *Gaia* data releases, we find dSph orbital precision will be limited by uncertainties in the distance and/or MW potential rather than proper motion precision. Finally, we provide our membership catalogs to enable community follow-up.

Keywords: editorials, notices — miscellaneous — catalogs — surveys

1. INTRODUCTION

The Milky Way (MW) dwarf spheroidal (dSph) satellite galaxies are a diverse set of galaxies spanning a wide range of stellar masses, sizes, dynamical masses, star formation histories, and orbital histories (e.g. [McConnachie 2012](#); [Simon 2019](#)). dSphs are near enough that their 6D phase space can be measured although the tangential motion is the most difficult, generally requiring space based astrometry. For many years, this was the exclusive domain of the Hubble Space Telescope (e.g., [Piatek et al. 2007](#); [Sohn et al. 2017](#)).

The tangential and orbital motion of MW dSphs has been revolutionized by astrometry from the *Gaia* mission. With the release of the first proper motion *Gaia* catalogs (i.e., *Gaia* DR2), the measurement of systemic

proper motion of nearly all the MW dSphs has been possible (e.g., [Gaia Collaboration et al. 2018](#); [Simon 2018](#); [Fritz et al. 2018a](#); [Pace & Li 2019](#); [McConnachie & Venn 2020a](#)) and has led to the determination of their orbital motion within the MW (e.g., [Gaia Collaboration et al. 2018](#); [Simon 2018](#); [Fritz et al. 2018a](#)). This has also led to measurements of the orbital anisotropy of the dSph system ([Riley et al. 2019](#)), satellite infall times ([Fillingham et al. 2019](#)), updates on potential planes of satellites in the MW (also known as, the vast polar structure, [Fritz et al. 2018a](#)), a potential excess of dSph near their orbital pericenter ([Simon 2018](#); [Fritz et al. 2018a](#)), and measurements of the mass of the MW ([Callingham et al. 2019](#); [Li et al. 2020](#); [Fritz et al. 2020](#)).

The recent discovery of MW satellites in the Dark Energy Survey (DES) and other southern surveys has revealed a new population of dSphs and several are likely LMC/SMC satellites (e.g., [Koposov et al. 2015a](#); [Bechtol et al. 2015](#); [Torrealba et al. 2018](#)). With radial veloci-

ties and *Gaia* proper motions a handful of satellites have been associated with the LMC (Kallivayalil et al. 2018; Erkal & Belokurov 2020; Patel et al. 2020). In addition to bringing in its own satellite population, the LMC also perturbs the orbits of dSphs in the MW (e.g. Gómez et al. 2015; Erkal & Belokurov 2020; Patel et al. 2020). While satellites which pass close to the LMC are directly accelerated, satellites with more distant passages can be indirectly affected by the reflex motion of the MW (e.g. Leo I and Antlia 2, Erkal et al. 2020; Ji et al. 2021; Correa Magnus & Vasiliev 2022). This reflex motion of $\sim 40 \text{ km s}^{-1}$ has also been measured in the MW’s stellar halo (Erkal et al. 2021; Petersen & Peñarrubia 2021).

With *Gaia* EDR3 the systemic proper motions of the dSphs have significantly improved (e.g. McConnachie & Venn 2020b; Li et al. 2021; Martínez-García et al. 2021; Vitral 2021; Battaglia et al. 2022). This is due to both the reduced statistic errors with an additional year of data and the reduction of the systematic errors by roughly a factor of two relative to DR2. As a result, the orbital properties have improved (Li et al. 2021; Battaglia et al. 2022) and the internal rotation has been observed in a few dSphs with *Gaia* EDR3 data (Martínez-García et al. 2021).

Here we measure the systemic proper motion and identity candidate members of 52 dwarfs (46 with line-of-sight velocities), compute the orbits both with and without the influence of the LMC, and discuss the tidal influences of the MW. In Section 2, we give an overview of the astrometric *Gaia* EDR3 data, the photometric data sets we complement the *Gaia* data with, and describe our initial quality selection and color-magnitude selection. In Section 3, we present our methodology for measuring the systemic proper motions and for computing orbits. In Section 4, we present the systemic proper motions and the orbital properties. In Section 5, we compare the orbital properties to indicators of tidal influences, discuss the orientation and orbital direction of the dSphs, discuss LMC association, discuss the potential excess of satellites near pericenter, and make projections for errors of the orbital parameters of future measurements. We summarize and conclude in Section 6.

2. DATA

We list the 54 MW dwarf galaxies and ultra-faint dwarf galaxies analyzed in this work along with relevant properties in Table 1. We restrict our sample to MW satellites, the most distant being Eri II. Throughout this analysis we will refer to the objects as dwarf spheroidal galaxies (dSphs) even though several objects do not have spectroscopic confirmation or have an ambiguous classification (e.g., Dra II, Sgr II, Tuc III). We do not include

the recently discovered dSphs Eridanus IV and Pegasus IV as similar methods were used derive the systemic proper motion and only Pegasus IV has a line-of-sight velocity measurement (Cerny et al. 2021, 2022). We will refer to the dSphs by their shorted acronyms throughout the paper which are listed in Table 1 along with their full names.

We group the satellites with $M_V < -7.7$ as ‘bright’ satellites and fainter satellites as ultra-faints (UFDs) following Simon (2019). This groups the more recently discovered satellites, Ant II, Cra II, and CVn I with the traditionally labelled classical satellites (Cra, Dra, For, Leo I, Leo II, Scl, Sxt, UMi). Until the advent of large CCD photometric surveys, the former escaped detection due to their low surface brightness (e.g., Zucker et al. 2006; Koposov et al. 2008; Torrealba et al. 2016a).

2.1. Astrometric Data

We use the astrometric *Gaia* EDR3 catalog (Gaia Collaboration et al. 2021a) for our systemic proper motion measurements. We consider two samples with different quality cuts which we refer to as ‘clean’ and ‘complete.’ The former is more restrictive and selects higher quality astrometry which we will use for our sytemic proper motion measurements whereas the latter is more inclusive and we will to maximize the number of candidate stars.

The quality selection for the clean sample is as follows (Lindgren et al. 2021; Riello et al. 2021):

- `astrometric_params_solved` > 3
- $G < G_{\text{max}}$,
- `astrometric_excess_noise_sig` < 2,
- `ruwe` < 1.3,
- $|C^*| \leq 3\sigma_{C^*}(G)$,
- `ipd_frac_multi_peak` < 2,
- `ipd_gof_harmonic_amplitude` < 0.1, however this cut is only applied to some of the dSphs¹,
- $\varpi - 3 \times \sigma_\varpi < 0$,

¹ For two-thirds of the satellites analyzed, this cut removes $\sim 2\%$ of stars within 1° of the satellite. However, for satellites with fewer visibility periods, this cut removes a large portion of the stars ($\sim 5 - 32\%$ for `visibility_periods_used` < 15). In particular, this cut would remove all known spectroscopic members in Aquarius II and removes $\sim 30\%$ of the stars around the Crater II and Sextans dSphs. The following dwarfs do not have the `ipd_gof_harmonic_amplitude` cut applied: Aqu II, Cet III, CB I, Cra II, Leo I, Leo II, Leo IV, Leo V, Peg III, Psc II, Sgr II, Seg 1, Seg 2, Sxt, Tri II, and Vir I.

- $v_{\text{tangential}} - 3 \times \sigma_{v_{\text{tangential}}} < v_{\text{escape}}$,
- `visibility_periods_used` > 10,
- `duplicated_source` = False.

G_{max} is determined based on the approximate magnitude where 90% of stars have an astrometric solution and varies between $G_{\text{max}} = 20.35 - 20.85$ for the dSph sample. Here $|C^*|$ is the corrected BP and RP flux excess factor (see Equation 6 of Riello et al. 2021). We compute the tangential velocity ($v_{\text{tangential}}$) of each star by converting the proper motions into Galactic coordinates in the Galactic Standard of Rest (GSR) frame after accounting for the Sun’s reflex motion, assuming $(U_{\odot}, V_{\odot}, W_{\odot}) = (11.1, 12.24, 7.25) \text{ km s}^{-1}$, a circular velocity of 220 km s^{-1} (Schönrich et al. 2010), and assume each star is at the satellite’s heliocentric distance. v_{esc} is computed with the potential `MWPotential2014` (with a slightly increased halo mass, $M_{\text{vir}} = 1.6 \times 10^{12} M_{\odot}$) from `galpy` (Bovy 2015). The escape velocity is a conservative cut to remove high proper motion stars that are nearby foreground MW stars. We remove AGN/QSOs galaxies from the sample with the *Gaia* catalog `gaiaedr3.agn_cross_id`.

For the complete sample, the following cuts are modified to be less restrictive: $G_{\text{max}} = 21$, `ruwe` < 1.4, $\varpi - 3.5 \times \sigma_{\varpi} < 0$, and $v_{\text{tangential}} - 3.5 \times \sigma_{v_{\text{tangential}}} < v_{\text{escape}}$. We remove the selection cuts on `ipd_gof_harmonic_amplitude`, `ipd_frac_multi_peak`, and `visibility_periods_used`.

We compute the systematic proper motion errors following Lindegren et al. (2021). The proper motion covariance function is:

$$V_{\mu}(\theta) = 292 \exp(-\theta/12^{\circ}) + 258 \exp(-\theta/0.25^{\circ}) \mu\text{as}^2 \text{ yr}^{-2}, \quad (1)$$

where θ is the angular separation between data points. We treat $\sigma_{\mu, \text{sys}} = \sqrt{V_{\mu}(\theta)}$ as the systematic error for each dSph. We use the half-light radius (r_h) of each dSph as the characteristic angular scale. We list $\sigma_{\mu, \text{sys}}$ values in Table 2. For our sample the proper motion systematic errors varied between $\sim 16 - 23 \mu\text{as yr}^{-1}$ and the median value is $22 \mu\text{as yr}^{-1}$. An alternative form is presented in Vasiliev & Baumgardt (2021) that has values of $V_{\mu}(\theta)$ that are 15% to 40% larger than Equation 1.

2.2. Photometry

We utilize several different photometric catalogs to improve the separation between dSph member stars and

MW interlopers. This is primarily composed of Dark Energy Camera (DECam; Flaugher et al. 2015) based data and Pan-STARRS1 DR1 (PS1) (Chambers et al. 2016) in the Northern sky. For the ‘bright’ dSphs we use *Gaia* EDR3 G , G_{RP} photometry. The DECam based catalogs include: the Dark Energy Survey (DES) DR2 (Abbott et al. 2021), the Dark Energy Camera Legacy Survey (DECaLS) DR9 (Dey et al. 2019), Survey of the Magellanic Stellar History DR2 (Nidever et al. 2021a), DECam Local Volume Exploration Survey DR1 (Drlica-Wagner et al. 2021), and the NOIRLab Source Catalog (NSC) DR2 (Nidever et al. 2021b). At faint magnitudes ($G \gtrsim 20$), the *Gaia* $G - G_{RP}$ color has significant errors and utilizing accurate auxiliary photometry significantly improves the separation between MW foreground and the dSph (see Figure 1 of Pace & Li 2019).

We opt to not apply any star/galaxy separation from the photometric surveys and instead use the *Gaia* astrometry as our stellar selection. In particular, there are several bright stars in DES DR2 that are considered galaxies (`extended_class_coadd=3`, e.g. the brightest member in Tuc III, Hansen et al. 2017 and a bright candidate member in Cet II) and the inclusion of these stars are key to determine the systemic proper motion.

We apply empirical isochrone based filters in the color-magnitude diagrams to improve dSph member selection. The isochrone filter is created based on spectroscopic members (see citations in Tables 1 & 4) and starts from an old, metal-poor isochrone. The DECam based selection is similar to Pace & Li (2019) but includes the red horizontal branch. This selection is based primarily on a g-r color selection of 0.12-0.15 around a $[\text{Fe}/\text{H}] = -2$ and age = 12 Gyr Dartmouth isochrone (Dotter et al. 2008) and around the ridgeline of the M92 globular cluster for horizontal branch stars (since Dartmouth isochrone does not contain a horizontal branch). For the DECam based photometry we do not increase the filter due to photometric errors as they are generally small at the limiting *Gaia* magnitude. The PS1 isochrone filter is created in a similar manner except we use PARSEC isochrone from Bressan et al. (2012). In contrast to the DECam based selection, we increase the width of the filter at faint magnitudes with an additional error term based on the median errors at a given magnitude, added in quadrature with the constant width of 0.15-0.16 in g-r color. For the bright satellites, we construct a wide *Gaia* $G - R_{RP}$ color-magnitude box based on spectroscopic members. The box width increases with magnitude to account for the large errors in color for fainter *Gaia* stars. We show the spectroscopic selection in Figure 1 along with the spectroscopic members used to construct the filter.

Table 1. dSph Properties

Name (Abbreviation)	RA deg	DEC deg	r_h arcmin	ϵ	θ	d kpc	M_V	v_{los} km s ⁻¹	σ_{los} km s ⁻¹	Ref
Antlia II(Ant II)	143.8868	-36.7673	76.20 ± 7.20	0.38 ± 0.08	156.0 ± 6.0	132.0 ± 6.0	-9.03 ± 0.15	290.7 ± 0.5	5.71 ± 1.08	a
Aquarius II(Aqu II)	338.4813	-9.3274	5.10 ± 0.80	0.39 ± 0.09	121.0 ± 9.0	107.9 ± 3.3	-4.36 ± 0.14	-71.1 ± 2.5	5.4 ± 2.15	b
Boötes I(Boo I)	210.0200	14.5135	9.97 ± 0.27	0.3 ± 0.03	6.0 ± 3.0	66.0 ± 3.0	-6.02 ± 0.25	101.8 ± 0.7	4.6 ± 0.7	c,d,e
Boötes II(Boo II)	209.5141	12.8553	3.17 ± 0.42	0.25 ± 0.11	-68.0 ± 27.0	42.0 ± 2.0	-2.94 ± 0.74	-117.0 ± 5.2	10.5 ± 7.4	f,e,g
Boötes III(Boo III)	209.3000	26.8000	33.03 ± 2.50	0.33 ± 0.085	-81.0 ± 8.0	46.5 ± 2.0	-5.75 ± 0.5	197.5 ± 3.8	14.0 ± 3.2	h,i,j
Boötes IV(Boo IV)	233.6890	43.7260	7.60 ± 0.80	0.64 ± 0.05	3.0 ± 4.0	209.0 ± 19.0	-4.53 ± 0.22			k
Canes Venatici I(CVn I)	202.0091	33.5521	7.12 ± 0.21	0.44 ± 0.03	80.0 ± 2.0	210.0 ± 6.0	-8.8 ± 0.06	30.9 ± 0.6	7.6 ± 0.4	l,e,m
Canes Venatici II(CVn II)	194.2927	34.3226	1.52 ± 0.24	0.4 ± 0.13	9.0 ± 15.0	160.0 ± 4.5	-5.17 ± 0.32	-128.9 ± 1.2	4.6 ± 0.8	n,e,m
Carina(Car)	100.4065	-50.9593	10.10 ± 0.10	0.36 ± 0.01	60.0 ± 1.0	105.6 ± 5.4	-9.43 ± 0.05	222.9 ± 0.1	6.6 ± 1.2	o,e,p
Carina II(Car II)	114.1066	-57.9991	8.69 ± 0.75	0.34 ± 0.07	170.0 ± 9.0	37.4 ± 0.4	-4.57 ± 0.1	477.2 ± 1.2	3.4 ± 1.0	q,r
Carina III(Car III)	114.6298	-57.8997	3.75 ± 1.00	0.55 ± 0.18	150.0 ± 14.0	27.8 ± 0.6	-2.4 ± 0.2	284.6 ± 3.25	5.6 ± 3.2	q,r
Centaurus I(Cen I)	189.5850	-40.9020	2.90 ± 0.45	0.4 ± 0.1	20.0 ± 11.0	116.3 ± 1.1	-5.55 ± 0.11			s
Cetus II(Cet II)	19.4700	-17.4200	1.90 ± 0.75	0.0 ± 0.0	0.0 ± 0.0	30.0 ± 3.0	0.0 ± 0.68			t
Cetus III(Cet III)	31.3310	-4.2700	1.23 ± 0.30	0.76 ± 0.07	101.0 ± 5.5	251.0 ± 17.5	-2.45 ± 0.565			u
Columba I(Col I)	82.8570	-28.0425	2.20 ± 0.20	0.3 ± 0.1	24.0 ± 9.0	183.0 ± 10.0	-4.2 ± 0.2	153.7 ± 4.9		v,w
Coma Berenices(CB)	186.7454	23.9069	5.64 ± 0.30	0.37 ± 0.05	-57.0 ± 4.0	42.0 ± 1.5	-4.38 ± 0.25	98.1 ± 0.9	4.6 ± 0.8	e,x,m
Crater II(Cra II)	177.3100	-18.4130	31.20 ± 2.50	0.0 ± 0.0	0.0 ± 0.0	117.5 ± 1.1	-8.2 ± 0.1	87.5 ± 0.4	2.7 ± 0.3	y,z
Draco(Dra)	260.0684	57.9185	9.67 ± 0.09	0.29 ± 0.01	87.0 ± 1.0	75.8 ± 5.4	-8.71 ± 0.05	-290.7 ± 0.75	9.1 ± 1.2	aa,e,ab
Draco II(Dra II)	238.1983	64.5653	3.00 ± 0.60	0.23 ± 0.15	76.0 ± 27.0	21.5 ± 0.4	-0.8 ± 0.7	-342.5 ± 1.15		ac
Eridanus II(Eri II)	56.0925	-43.5329	2.31 ± 0.12	0.48 ± 0.04	72.6 ± 3.3	366.0 ± 17.0	-7.1 ± 0.3	75.6 ± 1.3	6.9 ± 1.05	ad,ae
Fornax(For)	39.9583	-34.4997	19.90 ± 0.06	0.29 ± 0.02	42.7 ± 0.3	147.2 ± 8.4	-13.46 ± 0.14	55.2 ± 0.1	12.1 ± 0.2	e,af,p,ag
Grus I(Gru I)	344.1660	-50.1680	4.16 ± 0.64	0.44 ± 0.09	153.0 ± 7.5	127.0 ± 6.0	-4.3 ± 0.3	-140.5 ± 2.0		ah,ai,aj
Grus II(Gru II)	331.0250	-46.4420	5.90 ± 0.50	0.0 ± 0.0	0.0 ± 0.0	55.0 ± 2.0	-3.5 ± 0.3	-110.0 ± 0.5		ai,ak
Hercules(Her)	247.7722	12.7852	5.63 ± 0.46	0.69 ± 0.03	-73.0 ± 2.0	130.6 ± 6.1	-5.83 ± 0.17	45.0 ± 1.1	5.1 ± 0.9	e,al,m
Horologium I(Hor I)	43.8813	-54.1160	1.46 ± 0.07	0.16 ± 0.06	69.0 ± 11.0	79.0 ± 4.0	-3.4 ± 0.1	112.8 ± 2.55	4.9 ± 1.85	am,an,j
Horologium II(Hor II)	49.1077	-50.0486	2.09 ± 0.42	0.52 ± 15.0	127.0 ± 11.0	78.0 ± 8.0	-2.6 ± 0.25			ao
Hydra II(Hyd II)	185.4251	-31.9860	1.70 ± 0.25	0.01 ± 0.1	28.0 ± 37.5	151.0 ± 8.0	-5.1 ± 0.3	303.1 ± 1.4		ap,aq,ar
Hydrus I(Hy I)	37.3890	-79.3089	7.42 ± 0.58	0.21 ± 0.11	97.0 ± 14.0	27.6 ± 0.5	-4.71 ± 0.08	80.4 ± 0.6	2.7 ± 0.45	as

PACE, ERKAL, & LI

Table 1 continued

Table 1 (*continued*)

Name (Abbreviation)	RA deg	DEC deg	r_h arcmin	ϵ	θ	d kpc	M_V	v_{los} km s $^{-1}$	σ_{los} km s $^{-1}$	Ref
Leo I(Leo I)	152.1146	12.3059	3.65 \pm 0.03	0.3 \pm 0.1	78.0 \pm 1.0	258.2 \pm 9.5	-11.78 \pm 0.28	282.9 \pm 0.5	9.2 \pm 0.4	at,e,au
Leo II(Leo II)	168.3627	22.1529	2.52 \pm 0.03	0.07 \pm 0.01	38.0 \pm 8.0	233.0 \pm 15.0	-9.74 \pm 0.04	78.5 \pm 0.6	7.4 \pm 0.4	av,e,aw
Leo IV(Leo IV)	173.2405	-0.5453	2.54 \pm 0.27	0.17 \pm 0.09	-28.0 \pm 38.0	151.4 \pm 4.4	-4.99 \pm 0.26	132.3 \pm 1.4	3.3 \pm 1.7	ax,e,m
Leo V(Leo V)	172.7857	2.2194	1.00 \pm 0.32	0.43 \pm 0.22	-71.0 \pm 26.0	169.0 \pm 4.4	-4.4 \pm 0.36	173.0 \pm 0.9	3.2 \pm 1.55	ay,ax,e
Pegasus III(Peg III)	336.1074	5.4150	1.67 \pm 0.23	0.37 \pm 0.085	83.0 \pm 7.5	215.0 \pm 12.0	-4.17 \pm 0.205	-222.9 \pm 2.6	5.4 \pm 2.75	az,ba
Phoenix II(Phx II)	354.9960	-54.4115	1.50 \pm 0.30	0.4 \pm 0.1	156.0 \pm 13.0	84.1 \pm 8.0	-2.7 \pm 0.4	32.4 \pm 3.75		w,bb
Pictor I(Pic I)	70.9475	-50.2831	0.90 \pm 0.09	0.46 \pm 0.08	58.0 \pm 6.0	125.9 \pm 5.0	-3.1 \pm 0.3			am,j
Pictor II(Pic II)	101.1800	-59.8970	3.80 \pm 1.25	0.13 \pm 17.5	14.0 \pm 63.0	45.0 \pm 4.5	-3.2 \pm 0.45			bc
Pisces II(Psc II)	344.6345	5.9526	1.12 \pm 0.16	0.34 \pm 0.1	78.0 \pm 20.0	183.0 \pm 15.0	-4.22 \pm 0.38	-226.5 \pm 2.7	5.4 \pm 3.1	ape,bd
Reticulum II(Ret II)	53.9203	-54.0513	6.30 \pm 0.40	0.6 \pm 0.1	68.0 \pm 2.0	31.4 \pm 1.4	-3.1 \pm 0.1	64.3 \pm 1.2	3.6 \pm 0.85	bb,be
Reticulum III(Ret III)	56.3600	-60.4500	2.40 \pm 0.85	0.0 \pm 0.0	0.0 \pm 0.0	92.0 \pm 13.0	-3.3 \pm 0.29	274.2 \pm 7.45		t,w
Sagittarius II(Sgr II)	298.1687	-22.0681	1.60 \pm 0.10	0.0 \pm 0.0	0.0 \pm 0.0	70.2 \pm 5.0	-5.2 \pm 0.1	-177.2 \pm 0.55	1.7 \pm 0.5	bf,bb
Sculptor(ScI)	15.0183	-33.7186	11.17 \pm 0.05	0.33 \pm 0.01	92.0 \pm 1.0	83.9 \pm 1.5	-10.82 \pm 0.14	111.4 \pm 0.1	9.2 \pm 1.1	bg,e,p
Segue 1(Seg 1)	151.7504	16.0756	3.62 \pm 0.42	0.33 \pm 0.1	77.0 \pm 15.0	23.0 \pm 2.0	-1.3 \pm 0.73	208.5 \pm 0.9	3.7 \pm 1.25	bh,e,bi
Segue 2(Seg 2)	34.8226	20.1624	3.76 \pm 0.28	0.22 \pm 0.07	164.0 \pm 14.0	36.6 \pm 2.45	-1.86 \pm 0.88	-40.2 \pm 0.9		bj,bk,e
Sextans(Sxt)	153.2628	-1.6133	16.50 \pm 0.10	0.3 \pm 0.01	57.0 \pm 1.0	92.5 \pm 2.5	-8.72 \pm 0.06	224.3 \pm 0.1	7.9 \pm 1.3	e,bl,p
Triangulum II(Tri II)	33.3252	36.1702	2.50 \pm 0.30	0.3 \pm 0.1	73.0 \pm 17.0	28.4 \pm 1.6	-1.6 \pm 0.4	-381.7 \pm 1.1		v,bm
Tucana II(Tuc II)	342.9796	-58.5689	12.89 \pm 1.85	0.39 \pm 0.15	107.0 \pm 18.0	58.0 \pm 3.0	-3.8 \pm 0.1	-129.1 \pm 3.5	8.6 \pm 3.55	am,aj
Tucana III(Tuc III)	359.1075	-59.5833	5.10 \pm 1.20	0.2 \pm 0.1	25.0 \pm 38.0	22.9 \pm 0.9	-1.3 \pm 0.2	-102.3 \pm 0.4		bb,bn
Tucana IV(Tuc IV)	0.7170	-60.8300	9.30 \pm 1.15	0.39 \pm 0.085	27.0 \pm 8.5	47.0 \pm 4.0	-3.0 \pm 0.35	15.9 \pm 1.75	4.3 \pm 1.35	ak
Tucana V(Tuc V)	354.3470	-63.2660	2.10 \pm 0.50	0.51 \pm 0.135	29.0 \pm 11.0	55.0 \pm 5.5	-1.1 \pm 0.55	-36.2 \pm 2.35		ak
Ursa Major I(UMa I)	158.7706	51.9479	8.31 \pm 0.35	0.59 \pm 0.03	67.0 \pm 2.0	97.3 \pm 5.85	-5.13 \pm 0.38	-55.3 \pm 1.4	7.0 \pm 1.0	bo,e,m
Ursa Major II(UMa II)	132.8726	63.1335	13.80 \pm 0.50	0.56 \pm 0.03	-76.0 \pm 2.0	34.7 \pm 2.1	-4.25 \pm 0.26	-116.5 \pm 1.9	6.7 \pm 1.4	bp,e,m
Ursa Minor(UMi)	227.2420	67.2221	18.30 \pm 0.11	0.55 \pm 0.01	50.0 \pm 1.0	76.2 \pm 4.2	-9.03 \pm 0.05	-247.0 \pm 0.4	8.6 \pm 0.3	bq,e,br
Virgo I(Vir I)	180.0380	-0.6810	1.76 \pm 0.45	0.59 \pm 0.13	62.0 \pm 10.5	91.0 \pm 6.5	-0.33 \pm 0.81			u
Willman 1(Wil 1)	162.3436	51.0501	2.51 \pm 0.22	0.47 \pm 0.06	73.0 \pm 4.0	38.0 \pm 7.0	-2.53 \pm 0.74	-12.8 \pm 1.0	4.5 \pm 0.9	e,bs,bt

Table 1 (*continued*)

Name (Abbreviation)	r_h	ϵ	θ	d	M_V	v_{los}	σ_{los}	Ref
RA	DEC							

[illegible]

3. METHODS

To measure the systemic proper motions of the MW satellites we construct proper motion based mixture models that build on the methodology presented in [Pace & Li \(2019\)](#) and [McConnachie & Venn \(2020a\)](#). Briefly, we model the proper motions and spatial positions of stars near a satellite as a mixture of a satellite and MW foreground/background components:

$$\mathcal{L} = (1 - f_{\text{MW}})\mathcal{L}_{\text{satellite}} + f_{\text{MW}}\mathcal{L}_{\text{MW}}, \quad (2)$$

where each individual component is decomposed into spatial and proper motion (PM) terms:

$$\mathcal{L}_{\text{satellite/MW}} = \mathcal{L}_{\text{spatial}}\mathcal{L}_{\text{PM}}. \quad (3)$$

For the satellite spatial term, we assume a projected Plummer stellar distribution ([Plummer 1911](#)):

$$\Sigma(R_e) = \frac{1}{\pi r_p^2(1 - \epsilon)}(1 + R_e^2/r_p^2)^{-2}, \quad (4)$$

where r_p , ϵ , and R_e are the Plummer half-light radius, the ellipticity, and the elliptical radius, respectively. In contrast to [Pace & Li \(2019\)](#), we vary the spatial parameters, r_p , ϵ , and θ . We assume Gaussian priors on these parameters based on literature measurements (listed in Table 1). For the MW spatial component we assume that the MW component is spatially constant in the small regions around the satellite.

For satellite proper motion component we model the proper motions as a multivariate distribution (e.g., [Pace & Li 2019](#)). We include the covariance in the proper motion errors (the cross term in the proper motion error) and intrinsic proper motion dispersion terms. While the proper motion errors have improved in EDR3, they are not precise enough to measure internal dispersions and we fix intrinsic dispersion terms for the satellite component as they are smaller than the proper motion uncertainties. For most bright satellites we fix $\sigma_\mu = 10 \text{ km s}^{-1}$ and for all UFDs (including Ant II and Cra II) we fix $\sigma_\mu = 5 \text{ km s}^{-1}$.

For the MW proper motion distribution, we utilize two models. The first ‘fixed’ background model, is created from the proper motion distribution of stars at radii much larger than the target ([McConnachie & Venn 2020a](#)). At a large distance from the target dSph, this sample will only include MW stars. Especially, we select stars between $R_{\text{max,sat}} < R < R_{\text{max,BG}}$ and set $R_{\text{max,sat}}$ based on r_h . For the smaller UFDs, the maximum radius varies between $25' < R_{\text{max,sat}} < 60'$ and for the bright satellites it varies between $60' < R_{\text{max,sat}} < 210'$. We set the limiting radius of the background model to $R_{\text{max,BG}} = 2.5^\circ$ for the UFDs

and for the bright satellites (including Boo III) we use $R_{\text{max,BG}} = R_{\text{max,sat}} + 1^\circ$. We apply the same color-magnitude selection and astrometric filtering to the distant MW sample to mimic the selection for candidate satellite stars. We note for several satellites we removed other known stellar systems, e.g., Boo II from the Boo I background (and vice versa), Palomar 3 and Sextans A from the Sxt background. The second ‘Gaussian’ background model, uses a multi-variate Gaussian distribution with free proper motion dispersion terms (e.g., [Pace & Li 2019](#)). Other models have been explored in the literature including multiple Gaussian distributions (e.g., [Pace & Li 2019](#); [Vasiliev & Baumgardt 2021](#)) or a Pearson VII distribution ([Vital 2021](#)).

To determine the membership of stars we compute the relative likelihood between the satellite and total likelihood: $p = (1 - f_{\text{MW}})\mathcal{L}_{\text{satellite}} / [(1 - f_{\text{MW}})\mathcal{L}_{\text{satellite}} + f_{\text{MW}}\mathcal{L}_{\text{MW}}]$ (e.g., [Martinez et al. 2011](#)). We take the median value to be the star’s membership probability (which we refer to as p_i , for the i -th star) and compute the membership error (based on 16% and 84% confidence intervals) which we use to assess the confidence of the population assignment for individual stars and any potential signal from dSphs with few candidate members.

3.1. Orbit Methods

In order to simulate the orbits of these dwarfs, we account for the potential of the MW and the LMC. This is done using the technique of [Erkal & Belokurov \(2020\)](#) where the MW and the LMC are treated as individual particles sourcing their respective potentials. For the Milky Way potential we use the results of [McMillan \(2017\)](#) where the MW consists of an NFW halo, a bulge, and four disks (thin, thick, HI, and H₂). In order to account for the uncertainties in the MW potential, we sample from the posterior chains in [McMillan \(2017\)](#) in our fiducial setup. For the LMC, we use a Hernquist profile as in [Erkal & Belokurov \(2020\)](#), with a mass of $1.38 \pm 0.255 \times 10^{11} M_\odot$ (from [Erkal et al. 2019](#)) and a scale radius chosen to match the enclosed mass at 8.7 kpc ([van der Marel & Kallivayalil 2014](#)). In the fiducial setup, we also account for the observed uncertainties in the radial velocity ([van der Marel et al. 2002](#)), proper motion ([Kallivayalil et al. 2013](#)), and distance to the LMC ([Pietrzyński et al. 2019](#)). Each dwarf is then re-wound in the presence of the Milky Way and LMC for 10 Gyr to estimate its orbital properties. We note that these models include the Milky Way’s reflex motion in response to the LMC which was initially highlighted in [Gómez et al. \(2015\)](#) and measured in [Erkal et al. \(2021\)](#); [Petersen & Peñarrubia \(2021\)](#).

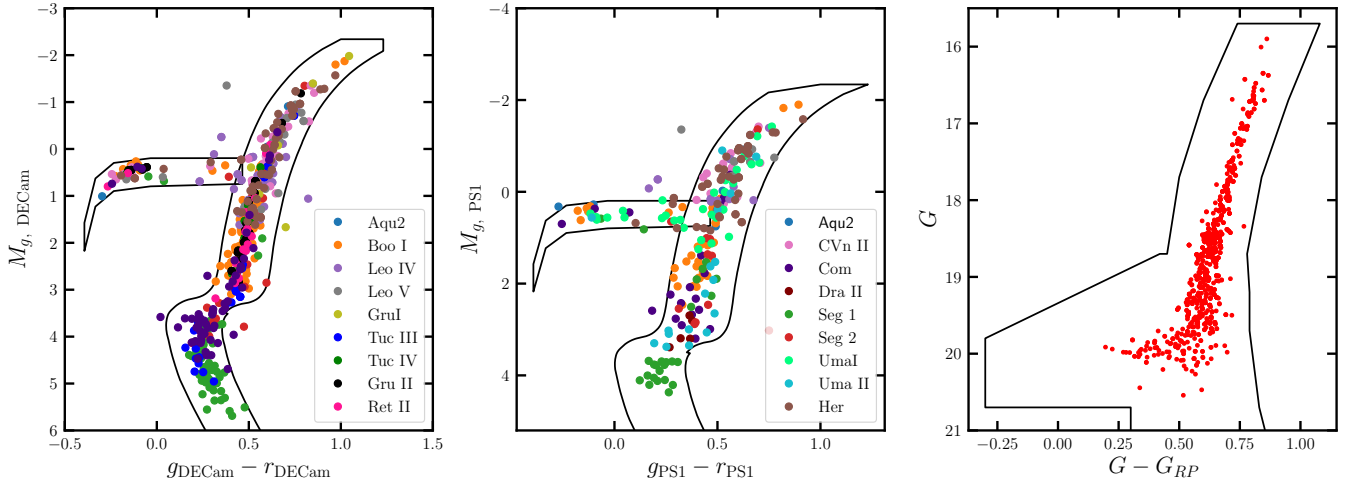


Figure 1. Color-magnitude selection based on spectroscopic members (see Tables 1,4 for citations). (Left) DECam based selection. The same filter is used for most of the DECam dSphs. (middle) PS1 based selection. The filter is expanded at faint magnitudes based on photometric errors. (right) *Gaia* based selection for Dra. A similar selection is made based on spectroscopic members for the other bright dSphs.

4. RESULTS

4.1. Proper Motions

We are able to measure the systemic proper motion of 52 of our 54 dSph sample of which 46 have line-of-sight velocities. We have the first confident detection of the systemic proper motion of Peg III and do not detect a signal in Cet III or Vir I. We identify between ~ 4 and ~ 16200 members in the 52 dSphs. To demonstrate the ability of our model to identify dwarf members, we show example results for four dSphs in Figure 2. The identified member stars cluster spatially, cluster in proper motion space, and cluster along metal-poor isochrones in color-magnitude space. In Table 2, we list our results for the systemic proper motion of the 52 dwarfs. We include our measurements and number of members with both the fixed and Gaussian background models with the clean sample. The systemic proper motions are in excellent agreement between the two background models, with differences $\lesssim 0.01 \text{ mas yr}^{-1}$.

For the majority of the UFDs there is excellent agreement in the total membership with both background models. Only in three UFDs, Hyi I, Boo III, and Tuc III, are there differences with $\Delta N \geq 5$. For the brighter dSphs, most show differences in total membership between the two background models. Ant II and Car in particular have large differences of ~ 140 and ~ 110 stars while other bright dwarfs have differences on the order $\sim 5 - 10$ stars. The individual stars with a large difference in membership between the two background models tend to be fainter stars with large proper motion errors. We note that for Car II, Car III, and Pic II we do not have results from the Gaussian background model,

this is discussed in more detail in Appendix B. We consider the results from the fixed background model as our default model.

We find that the two data samples, ‘clean’ and ‘complete,’ have excellent agreement between them. Results with the same background model finds similar membership for stars that overlap between the ‘clean’ and ‘complete’ samples. We base our primary results on the ‘clean’ sample in this analysis and provide membership for both samples and both background models in Appendix A. This will enable future spectroscopic follow-up. To enable the search for distant members, we recompute our membership analysis without the spatial component and only use the proper motion posterior (e.g., Chiti et al. 2020; Qi et al. 2022) and include these membership probabilities in Appendix A.

We are not able to measure the systemic motion of Cet III or Vir I and are only able to measure a signal in Psc II when spectroscopic information is included (see Appendix B). Neither Cet III nor Vir I have any spectroscopic follow-up and there are no stars with high membership probability. In order to measure the systemic proper motion with *Gaia* astrometry, members will need to be identified beforehand (i.e., with spectroscopy) and these systems may be faint enough that there are no stars above the *Gaia* magnitude limit. Boo IV, Hor II, Peg III, and Tuc V have the most uncertain detections with ~ 4 members in each. Only Tuc V has *Gaia* candidate stars that are spectroscopically confirmed.

Systematic proper motion errors computed using Equation 1 are presented in Table 2. There are 15 dSphs where the systematic proper motion error is larger than

Table 2. Systemic Proper Motion Measurements

Dwarf	N	$N_{mem,F}$	$\overline{\mu_{\alpha*F}}$	$\overline{\mu\delta_F}$	$N_{mem,G}$	$\overline{\mu_{\alpha*G}}$	$\overline{\mu\delta_G}$	$\sigma_{\mu,sys}$
Ant II	4889	558.2 ^{+25.6} _{-25.2}	-0.093 ^{+0.008} _{-0.008}	0.100 ^{+0.009} _{-0.009}	414.7 ^{+24.9} _{-24.6}	-0.090 ^{+0.009} _{-0.009}	0.100 ^{+0.010} _{-0.010}	0.016
Aqu II	51	16.3 ^{+1.8} _{-1.8}	-0.170 ^{+0.113} _{-0.119}	-0.466 ^{+0.096} _{-0.095}	14.3 ^{+2.1} _{-1.7}	-0.183 ^{+0.121} _{-0.122}	-0.446 ^{+0.099} _{-0.096}	0.022
Boo I	373	167.9 ^{+3.5} _{-3.6}	-0.385 ^{+0.017} _{-0.017}	-1.068 ^{+0.013} _{-0.013}	170.0 ^{+4.5} _{-4.5}	-0.387 ^{+0.017} _{-0.016}	-1.064 ^{+0.013} _{-0.013}	0.021
Boo II	88	20.9 ^{+1.0} _{-0.9}	-2.426 ^{+0.080} _{-0.077}	-0.414 ^{+0.061} _{-0.061}	20.2 ^{+1.1} _{-1.0}	-2.419 ^{+0.078} _{-0.080}	-0.413 ^{+0.061} _{-0.061}	0.022
Boo III	1073	73.6 ^{+6.0} _{-5.7}	-1.176 ^{+0.019} _{-0.019}	-0.890 ^{+0.015} _{-0.015}	90.8 ^{+7.1} _{-6.8}	-1.168 ^{+0.018} _{-0.018}	-0.890 ^{+0.014} _{-0.014}	0.018
Boo IV	43	4.2 ^{+0.5} _{-0.8}	0.469 ^{+0.180} _{-0.244}	0.489 ^{+0.256} _{-0.255}	4.1 ^{+0.5} _{-1.3}	0.445 ^{+0.195} _{-0.433}	0.500 ^{+0.311} _{-0.295}	0.021
CVn I	322	122.5 ^{+1.4} _{-1.4}	-0.096 ^{+0.030} _{-0.031}	-0.116 ^{+0.020} _{-0.020}	120.5 ^{+1.8} _{-1.8}	-0.093 ^{+0.030} _{-0.030}	-0.114 ^{+0.020} _{-0.020}	0.021
CVn II	15	11.1 ^{+0.6} _{-0.6}	-0.124 ^{+0.117} _{-0.115}	-0.254 ^{+0.082} _{-0.080}	11.8 ^{+1.1} _{-0.5}	-0.116 ^{+0.111} _{-0.109}	-0.264 ^{+0.080} _{-0.079}	0.023
Car	10273	2043.4 ^{+11.5} _{-11.4}	0.532 ^{+0.007} _{-0.006}	0.127 ^{+0.006} _{-0.006}	1952.8 ^{+11.8} _{-11.7}	0.534 ^{+0.007} _{-0.007}	0.124 ^{+0.006} _{-0.006}	0.020
Car II	5033	60.4 ^{+3.7} _{-3.7}	1.885 ^{+0.018} _{-0.019}	0.133 ^{+0.019} _{-0.019}				0.021
Car III	5033	9.5 ^{+1.3} _{-1.0}	3.095 ^{+0.040} _{-0.041}	1.395 ^{+0.045} _{-0.045}				0.022
Cen I	282	19.0 ^{+1.8} _{-1.8}	-0.074 ^{+0.062} _{-0.065}	-0.199 ^{+0.054} _{-0.055}	17.9 ^{+1.8} _{-1.7}	-0.063 ^{+0.063} _{-0.065}	-0.198 ^{+0.056} _{-0.056}	0.022
Cet II	151	4.9 ^{+0.1} _{-0.1}	2.844 ^{+0.061} _{-0.059}	0.474 ^{+0.064} _{-0.063}	5.0 ^{+0.0} _{-0.0}	2.845 ^{+0.060} _{-0.060}	0.475 ^{+0.063} _{-0.064}	0.023
Col I	54	5.7 ^{+0.3} _{-0.3}	0.169 ^{+0.071} _{-0.073}	-0.400 ^{+0.079} _{-0.079}	5.6 ^{+0.3} _{-0.3}	0.168 ^{+0.071} _{-0.073}	-0.400 ^{+0.081} _{-0.081}	0.023
CB	265	35.5 ^{+0.9} _{-0.9}	0.423 ^{+0.026} _{-0.027}	-1.721 ^{+0.024} _{-0.024}	35.7 ^{+1.0} _{-1.1}	0.423 ^{+0.026} _{-0.025}	-1.720 ^{+0.024} _{-0.024}	0.022
Cra II	9310	390.3 ^{+13.8} _{-13.4}	-0.072 ^{+0.020} _{-0.020}	-0.112 ^{+0.013} _{-0.013}	371.2 ^{+13.2} _{-12.9}	-0.053 ^{+0.020} _{-0.021}	-0.103 ^{+0.013} _{-0.013}	0.018
Dra	5678	1517.6 ^{+4.0} _{-4.0}	0.044 ^{+0.005} _{-0.006}	-0.188 ^{+0.006} _{-0.006}	1506.3 ^{+4.7} _{-4.7}	0.046 ^{+0.006} _{-0.006}	-0.188 ^{+0.006} _{-0.006}	0.021
Dra II	247	20.0 ^{+0.6} _{-0.8}	1.027 ^{+0.067} _{-0.065}	0.887 ^{+0.072} _{-0.072}	19.5 ^{+0.8} _{-1.1}	1.030 ^{+0.069} _{-0.068}	0.889 ^{+0.077} _{-0.072}	0.022
Eri II	23	19.5 ^{+0.5} _{-0.5}	0.125 ^{+0.101} _{-0.100}	0.013 ^{+0.123} _{-0.127}	19.5 ^{+2.1} _{-0.8}	0.136 ^{+0.098} _{-0.100}	0.003 ^{+0.125} _{-0.121}	0.023
For	17007	16222.9 ^{+5.6} _{-5.6}	0.381 ^{+0.001} _{-0.001}	-0.359 ^{+0.002} _{-0.002}	16198.2 ^{+9.8} _{-9.8}	0.381 ^{+0.001} _{-0.001}	-0.358 ^{+0.002} _{-0.002}	0.019
Gru I	74	9.3 ^{+0.3} _{-0.4}	0.069 ^{+0.051} _{-0.050}	-0.248 ^{+0.071} _{-0.072}	9.4 ^{+0.3} _{-0.4}	0.070 ^{+0.050} _{-0.050}	-0.246 ^{+0.073} _{-0.072}	0.022
Gru II	204	32.8 ^{+3.2} _{-3.1}	0.384 ^{+0.033} _{-0.033}	-1.484 ^{+0.039} _{-0.040}	34.4 ^{+3.5} _{-3.4}	0.384 ^{+0.033} _{-0.032}	-1.478 ^{+0.038} _{-0.040}	0.022
Her	184	40.9 ^{+1.4} _{-1.5}	-0.035 ^{+0.042} _{-0.042}	-0.339 ^{+0.035} _{-0.036}	41.0 ^{+1.3} _{-1.4}	-0.031 ^{+0.040} _{-0.041}	-0.334 ^{+0.034} _{-0.034}	0.022
Hor I	50	19.1 ^{+0.5} _{-0.4}	0.847 ^{+0.034} _{-0.035}	-0.607 ^{+0.035} _{-0.035}	19.2 ^{+0.6} _{-0.6}	0.846 ^{+0.034} _{-0.034}	-0.606 ^{+0.036} _{-0.036}	0.023
Hor II	40	3.9 ^{+0.3} _{-0.3}	0.967 ^{+0.173} _{-0.171}	-0.771 ^{+0.220} _{-0.230}	3.8 ^{+0.3} _{-0.4}	0.976 ^{+0.177} _{-0.179}	-0.762 ^{+0.233} _{-0.237}	0.023
Hyd II	82	17.5 ^{+0.4} _{-0.5}	-0.394 ^{+0.140} _{-0.140}	0.000 ^{+0.103} _{-0.104}	17.3 ^{+0.5} _{-0.6}	-0.395 ^{+0.139} _{-0.142}	0.001 ^{+0.106} _{-0.106}	0.023
Hyi I	1801	102.4 ^{+4.0} _{-4.0}	3.781 ^{+0.016} _{-0.016}	-1.496 ^{+0.015} _{-0.015}	92.3 ^{+3.9} _{-4.0}	3.783 ^{+0.016} _{-0.016}	-1.495 ^{+0.015} _{-0.015}	0.021
Leo I	1031	920.7 ^{+1.1} _{-1.1}	-0.050 ^{+0.014} _{-0.014}	-0.120 ^{+0.010} _{-0.010}	920.6 ^{+1.8} _{-1.8}	-0.047 ^{+0.014} _{-0.014}	-0.118 ^{+0.010} _{-0.010}	0.022
Leo II	343	264.4 ^{+0.5} _{-0.5}	-0.109 ^{+0.028} _{-0.028}	-0.150 ^{+0.026} _{-0.026}	263.9 ^{+1.0} _{-0.8}	-0.108 ^{+0.028} _{-0.028}	-0.149 ^{+0.027} _{-0.027}	0.023
Leo IV	11	6.2 ^{+0.2} _{-0.1}	-0.009 ^{+0.152} _{-0.152}	-0.279 ^{+0.115} _{-0.112}	6.2 ^{+0.8} _{-0.2}	-0.021 ^{+0.152} _{-0.150}	-0.279 ^{+0.110} _{-0.111}	0.023
Leo V	6	6.0 ^{+0.0} _{-0.0}	0.113 ^{+0.219} _{-0.215}	-0.391 ^{+0.155} _{-0.153}	6.0 ^{+0.0} _{-0.0}	0.115 ^{+0.213} _{-0.217}	-0.391 ^{+0.151} _{-0.154}	0.023
Peg III	25	3.9 ^{+0.3} _{-0.4}	-0.030 ^{+0.210} _{-0.210}	-0.580 ^{+0.213} _{-0.208}	3.8 ^{+0.3} _{-0.4}	-0.019 ^{+0.212} _{-0.218}	-0.567 ^{+0.217} _{-0.217}	0.023
Phx II	45	9.5 ^{+0.3} _{-0.3}	0.507 ^{+0.047} _{-0.048}	-1.199 ^{+0.058} _{-0.057}	9.5 ^{+0.3} _{-0.3}	0.507 ^{+0.047} _{-0.048}	-1.198 ^{+0.058} _{-0.059}	0.023
Pic I	68	8.3 ^{+0.3} _{-0.3}	0.153 ^{+0.086} _{-0.088}	0.096 ^{+0.118} _{-0.114}	8.2 ^{+0.3} _{-0.4}	0.150 ^{+0.087} _{-0.087}	0.097 ^{+0.119} _{-0.117}	0.023
Pic II	455	6.1 ^{+3.5} _{-1.5}	1.091 ^{+0.113} _{-0.423}	1.179 ^{+0.116} _{-0.087}				0.022
Psc II	3		0.681 ^{+0.309} _{-0.307}	-0.645 ^{+0.215} _{-0.209}				0.022
Ret II	465	50.2 ^{+1.4} _{-1.4}	2.377 ^{+0.023} _{-0.024}	-1.379 ^{+0.026} _{-0.025}	49.4 ^{+1.4} _{-1.5}	2.375 ^{+0.023} _{-0.023}	-1.378 ^{+0.027} _{-0.026}	0.021
Ret III	67	5.7 ^{+0.8} _{-1.5}	0.260 ^{+0.140} _{-0.144}	-0.502 ^{+0.222} _{-0.226}	4.9 ^{+1.1} _{-2.2}	0.260 ^{+0.163} _{-0.173}	-0.524 ^{+0.330} _{-0.318}	0.023
Sgr II	769	65.2 ^{+1.3} _{-1.3}	-0.769 ^{+0.035} _{-0.035}	-0.903 ^{+0.022} _{-0.023}	63.1 ^{+1.3} _{-1.3}	-0.771 ^{+0.036} _{-0.035}	-0.902 ^{+0.023} _{-0.023}	0.023
Scl	7362	6184.2 ^{+3.5} _{-3.6}	0.100 ^{+0.002} _{-0.002}	-0.158 ^{+0.002} _{-0.002}	6195.5 ^{+6.6} _{-6.5}	0.101 ^{+0.003} _{-0.003}	-0.156 ^{+0.002} _{-0.002}	0.020
Seg 1	302	17.9 ^{+1.9} _{-1.9}	-2.102 ^{+0.051} _{-0.051}	-3.375 ^{+0.044} _{-0.046}	16.5 ^{+1.9} _{-1.9}	-2.099 ^{+0.053} _{-0.054}	-3.375 ^{+0.047} _{-0.047}	0.022
Seg 2	201	16.4 ^{+0.7} _{-0.7}	1.446 ^{+0.059} _{-0.059}	-0.322 ^{+0.049} _{-0.050}	15.9 ^{+0.7} _{-0.7}	1.445 ^{+0.059} _{-0.061}	-0.321 ^{+0.050} _{-0.051}	0.022
Sxt	4359	1361.0 ^{+6.5} _{-6.5}	-0.409 ^{+0.009} _{-0.008}	0.037 ^{+0.009} _{-0.009}	1333.0 ^{+8.2} _{-8.2}	-0.409 ^{+0.009} _{-0.009}	0.041 ^{+0.009} _{-0.009}	0.019
Tri II	799	10.7 ^{+1.5} _{-1.3}	0.575 ^{+0.060} _{-0.060}	0.112 ^{+0.069} _{-0.067}	11.1 ^{+1.5} _{-1.3}	0.571 ^{+0.058} _{-0.058}	0.109 ^{+0.065} _{-0.067}	0.023
Tuc II	277	40.6 ^{+4.7} _{-4.6}	0.911 ^{+0.024} _{-0.026}	-1.280 ^{+0.029} _{-0.029}	42.5 ^{+5.0} _{-5.0}	0.905 ^{+0.024} _{-0.026}	-1.277 ^{+0.029} _{-0.030}	0.020
Tuc III	881	46.8 ^{+5.1} _{-4.7}	-0.048 ^{+0.035} _{-0.036}	-1.638 ^{+0.039} _{-0.039}	54.3 ^{+5.9} _{-5.7}	-0.040 ^{+0.034} _{-0.034}	-1.629 ^{+0.038} _{-0.038}	0.022
Tuc IV	344	11.0 ^{+2.2} _{-1.9}	0.534 ^{+0.050} _{-0.053}	-1.707 ^{+0.054} _{-0.055}	12.1 ^{+2.3} _{-2.1}	0.540 ^{+0.049} _{-0.051}	-1.697 ^{+0.053} _{-0.055}	0.021
Tuc V	62	4.6 ^{+1.7} _{-4.6}	-0.161 ^{+0.087} _{-0.176}	-1.157 ^{+0.150} _{-0.195}	5.6 ^{+1.2} _{-3.1}	-0.152 ^{+0.057} _{-0.068}	-1.151 ^{+0.074} _{-0.079}	0.023
UMa I	122	44.0 ^{+0.9} _{-1.0}	-0.401 ^{+0.036} _{-0.036}	-0.613 ^{+0.040} _{-0.042}	42.9 ^{+1.2} _{-1.3}	-0.398 ^{+0.036} _{-0.038}	-0.614 ^{+0.042} _{-0.043}	0.021
UMa II	812	47.0 ^{+2.3} _{-2.3}	1.731 ^{+0.021} _{-0.021}	-1.906 ^{+0.024} _{-0.025}	42.6 ^{+2.6} _{-2.6}	1.734 ^{+0.022} _{-0.022}	-1.902 ^{+0.025} _{-0.025}	0.020
UMi	5113	1909.1 ^{+6.9} _{-6.9}	-0.120 ^{+0.005} _{-0.005}	0.071 ^{+0.005} _{-0.005}	1890.2 ^{+8.0} _{-8.1}	-0.119 ^{+0.005} _{-0.005}	0.072 ^{+0.005} _{-0.005}	0.019
Wil 1	76	7.7 ^{+0.9} _{-0.6}	0.255 ^{+0.077} _{-0.087}	-1.110 ^{+0.095} _{-0.091}	7.6 ^{+1.1} _{-0.5}	0.241 ^{+0.082} _{-0.085}	-1.108 ^{+0.096} _{-0.096}	0.023

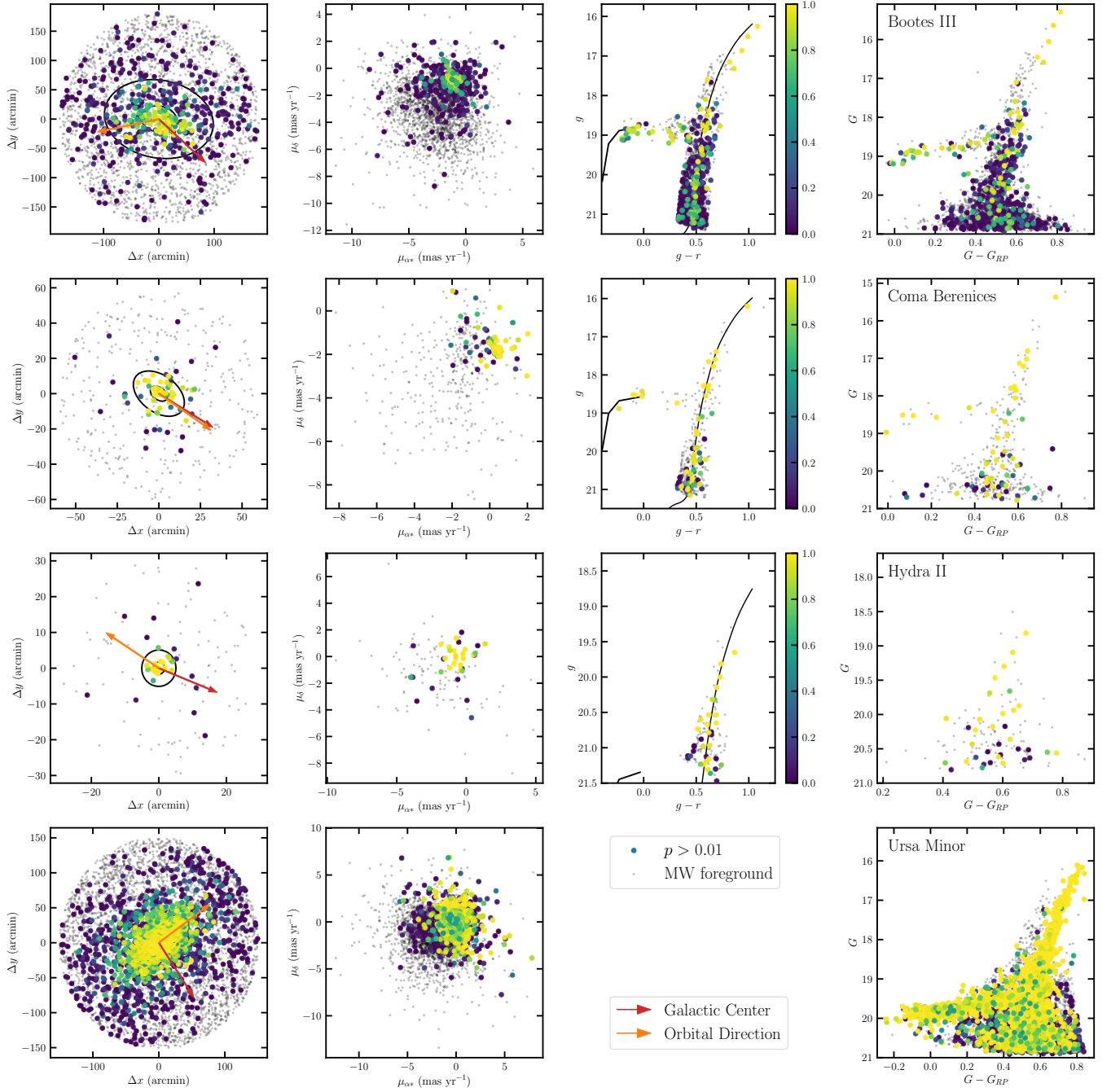


Figure 2. Results of the mixture model for 4 dSphs, from top to bottom: Boo III, CB, Hyd II, and UMi. The four rows are the spatial distribution (tangent plane), the proper motion (vector point diagram), a DECam based color-magnitude diagram (not included for UMi), and a *Gaia* color-magnitude diagram. Points with membership probability $p > 0.01$ are colored according to their probability; the rest are considered MW foreground stars and are shown as grey points. The red arrow points toward the Galactic center and the orange arrow is the direction of the reflex-corrected proper motion which is approximately equal to the orbital motion. Two ellipses are included in the spatial distribution at one and three times the half-light radius.

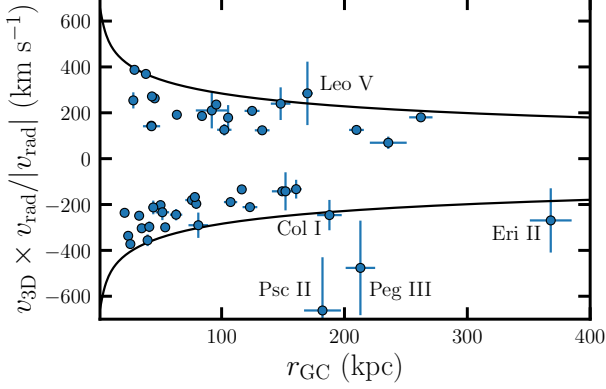


Figure 3. Phase-space diagram for the MW dSphs where the x-axis shows the distance to the Galactic center (GC) and the y-axis shows the total velocity in 3D, where positive (negative) indicates that the dSph is moving away from (towards) the GC. The black lines represent the escape velocity of the MW.

the statistical error. This includes all ‘bright’ dSphs except for Leo II, and five UFDs, Boo I, Boo III, Car II, Hyi I, and Sgr II. Excluding Leo II, dSphs with more than ~ 60 members are dominated by systematic errors whereas systems with fewer members are dominated by statistical errors. We note that because of Leo II’s distance it has a larger statistical error than other systems with a similar number of stars.

In Figure 3, we show the phase-space diagram for the 46 MW dSphs with systemic proper motion measurements and line-of-sight velocity data. For comparison we include the escape velocity of the MW. The 5 dSphs outside of the MW escape velocity are labeled but we note that they have the largest tangential velocity errors and their total velocity may be overestimated.

4.2. Orbits

Next, we explore the orbits of these dwarfs in the Milky Way as described in Section 3.1. In our fiducial setup, we include the LMC and Monte Carlo over the uncertainties in the observational properties of each dwarf (i.e. proper motions, radial velocity, and distance), as well as the potential parameters of the Milky Way and the LMC (see Sec. 3.1 for more details). This Monte Carlo process is repeated 10,000 times for each dwarf to sample the uncertainties. In addition to this fiducial run, we also have an ‘nL’ run where the LMC’s effect is not included. This allows us to see how much the orbital properties are influenced by the LMC. We note that we have also repeated the same suite several times with different assumptions about the observational, Milky Way potential, and LMC potential errors in order to explore

the dominant contribution to the error. We discuss this analysis in Section 5.7.

For the 46 dwarfs with line-of-sight velocities we compute their orbital properties with and without the presence of the LMC. For the 16 dwarfs whose orbits are significantly affected ($> 25\%$ change in either pericenter or apocenter), we show the orbital properties with and without the LMC in Figure 4. This shows that in order to get precise orbits, the LMC must be accounted for.

In Table 3, we list the pericenter, apocenter, eccentricity, and probability of being an LMC satellite. We include the ratio of pericenter and apocenter with and without the influence of the LMC to highlight which dwarfs are significantly affected by the inclusion of the LMC. We note that we define the pericenter and apocenter respectively as the first local minimum and maximum in the distance from the Milky Way during the backwards rewinding of each satellite. This is motivated by the results of D’Souza & Bell (2022) who showed that while the most recent pericenter and apocenter can be reliably determined during backwards integration, subsequent pericenters and apocenters are more poorly constrained. As a result, if a satellite is unbound from the Milky Way, it may not have a pericenter or an apocenter. We note that we only compute orbital uncertainties in pericenter and apocenter for the subset of realizations which respectively reach their pericenter and apocenter during the integration. We find that $\sim 2\%$, 6% , 15% , 34% , 46% , 77% , 87% , 88% , 89% , and 89% of the samples in Psc II, Peg III, Eri II, Col I, Leo V, Hyd II, Leo IV, CVn II, Phx II, and Ret II respectively, reach their pericenters and/or apocenters during our orbit integration and these samples might not be bound to the MW. The first 5 of these dSphs have the largest proper motion errors of the sample. The reminder of satellites have pericenters and apocenters for $> 90\%$ of the sample.

The following dwarfs have a significant change ($> 25\%$) to their orbital pericenter due to the presence of the LMC: Ant II, Aqu II, Cvn I, Car, Cra II, Dra, Eri II, Gru I, Hyi I, Ret II, Sgr II, Tuc III, and UMi. These updated orbits may have a significant effect on the tidal disruption of these satellites. Indeed, for Ant II and Cra II, the effect of these updated orbits on the dwarf’s tidal disruption has already been studied (i.e. Ji et al. 2021).

Several dwarfs have a significant change to their orbital apocenter due to the presence of the LMC: Aqu II, Col I, Leo V, Ret II, Ret III, Scl, Sxt, and Tuc II. While some of these are believed to be LMC satellites which would naturally affect their apocenters (i.e. Ret II), the change in the orbits of the remaining dwarfs may signif-

Table 3. dSph Orbital Properties

Dwarf	r_{peri} kpc	r_{apo} kpc	ecc	f_{peri}	$r_{\text{peri}}^{\text{nL}}$ kpc	$r_{\text{apo}}^{\text{nL}}$ kpc	ecc ^{nL}	$f_{\text{peri}}^{\text{nL}}$	$r_{\text{peri}}/r_{\text{peri}}^{\text{nL}}$	$r_{\text{apo}}/r_{\text{apo}}^{\text{nL}}$	p_{LMC}
Ant II	38.2 ^{+10.0} _{-7.8}	137.2 ^{+7.6} _{-6.8}	0.56 ^{+0.06} _{-0.07}	0.96 ^{+0.04} _{-0.05}	50.7 ^{+12.9} _{-9.7}	144.7 ^{+9.2} _{-7.7}	0.48 ^{+0.07} _{-0.07}	0.88 ^{+0.03} _{-0.07}	0.75	0.95	0.00
Aqu II	55.1 ^{+40.8} _{-32.7}	145.9 ^{+53.6} _{-17.4}	0.49 ^{+0.23} _{-0.13}	0.57 ^{+0.18} _{-0.46}	77.9 ^{+23.2} _{-41.2}	115.6 ^{+81.3} _{-7.8}	0.31 ^{+0.24} _{-0.13}	0.75 ^{+0.20} _{-0.72}	0.71	1.26	0.00
Boo I	37.9 ^{+7.5} _{-6.8}	71.7 ^{+8.3} _{-5.5}	0.31 ^{+0.05} _{-0.04}	0.77 ^{+0.09} _{-0.17}	35.3 ^{+7.1} _{-6.1}	80.9 ^{+11.0} _{-7.1}	0.40 ^{+0.04} _{-0.03}	0.62 ^{+0.09} _{-0.15}	1.07	0.89	0.00
Boo II	35.8 ^{+2.9} _{-2.5}	176.3 ^{+122.5} _{-56.0}	0.65 ^{+0.10} _{-0.10}	0.03 ^{+0.02} _{-0.02}	39.0 ^{+1.9} _{-1.9}	203.0 ^{+178.1} _{-75.4}	0.68 ^{+0.10} _{-0.11}	0.00 ^{+0.00} _{-0.00}	0.92	0.87	0.00
Boo III	7.8 ^{+2.3} _{-2.0}	97.9 ^{+17.1} _{-10.9}	0.86 ^{+0.03} _{-0.03}	0.42 ^{+0.05} _{-0.07}	7.5 ^{+2.2} _{-1.9}	108.1 ^{+21.4} _{-12.8}	0.87 ^{+0.03} _{-0.03}	0.38 ^{+0.05} _{-0.07}	1.04	0.91	0.00
CVn I	84.5 ^{+53.6} _{-37.2}	229.8 ^{+31.7} _{-13.2}	0.46 ^{+0.18} _{-0.13}	0.87 ^{+0.08} _{-0.28}	68.7 ^{+42.7} _{-31.0}	256.5 ^{+34.2} _{-16.0}	0.58 ^{+0.15} _{-0.12}	0.76 ^{+0.08} _{-0.20}	1.23	0.90	0.10
CVn II	47.5 ^{+46.8} _{-29.7}	234.0 ^{+92.5} _{-27.1}	0.66 ^{+0.19} _{-0.14}	0.62 ^{+0.13} _{-0.29}	46.0 ^{+45.5} _{-27.6}	201.1 ^{+55.2} _{-15.0}	0.64 ^{+0.20} _{-0.16}	0.75 ^{+0.09} _{-0.29}	1.03	1.16	0.01
Car	77.9 ^{+24.1} _{-17.9}	108.1 ^{+7.9} _{-5.7}	0.18 ^{+0.10} _{-0.12}	1.00 ^{+0.00} _{-0.09}	104.6 ^{+7.5} _{-22.5}	114.4 ^{+49.7} _{-11.8}	0.10 ^{+0.11} _{-0.07}	0.10 ^{+0.89} _{-0.10}	0.74	0.94	0.28
Car II	29.2 ^{+0.6} _{-0.6}	176.0 ^{+170.7} _{-43.5}	0.72 ^{+0.13} _{-0.07}	0.06 ^{+0.03} _{-0.03}	28.9 ^{+0.6} _{-0.6}	227.1 ^{+143.4} _{-55.4}	0.78 ^{+0.08} _{-0.06}	0.05 ^{+0.02} _{-0.02}	1.01	0.78	1.00
Car III	28.8 ^{+0.6} _{-0.6}	230.1 ^{+121.2} _{-44.3}	0.78 ^{+0.07} _{-0.04}	0.00 ^{+0.00} _{-0.00}	28.7 ^{+0.6} _{-0.6}	185.7 ^{+122.5} _{-50.3}	0.74 ^{+0.09} _{-0.08}	0.00 ^{+0.00} _{-0.00}	1.00	1.24	1.00
Col I	165.5 ^{+15.0} _{-57.2}	303.0 ^{+248.4} _{-112.3}	0.24 ^{+0.15} _{-0.11}	0.20 ^{+0.77} _{-0.15}	175.0 ^{+17.5} _{-65.1}	232.9 ^{+253.9} _{-102.2}	0.25 ^{+0.14} _{-0.09}	0.26 ^{+0.67} _{-0.22}	0.95	1.30	0.01
CB	42.5 ^{+1.6} _{-1.6}	68.1 ^{+17.1} _{-11.0}	0.23 ^{+0.09} _{-0.07}	0.03 ^{+0.03} _{-0.01}	42.4 ^{+1.5} _{-1.6}	80.4 ^{+23.4} _{-14.3}	0.31 ^{+0.10} _{-0.08}	0.02 ^{+0.02} _{-0.01}	1.00	0.85	0.00
Cra II	24.0 ^{+5.6} _{-5.2}	138.1 ^{+7.9} _{-4.9}	0.71 ^{+0.05} _{-0.05}	0.81 ^{+0.04} _{-0.06}	35.8 ^{+8.4} _{-6.8}	137.1 ^{+7.0} _{-4.5}	0.59 ^{+0.06} _{-0.06}	0.80 ^{+0.04} _{-0.07}	0.67	1.01	0.36
Dra	58.0 ^{+11.4} _{-9.5}	106.3 ^{+20.4} _{-13.1}	0.30 ^{+0.04} _{-0.04}	0.37 ^{+0.16} _{-0.21}	40.4 ^{+6.5} _{-5.4}	95.6 ^{+12.0} _{-9.1}	0.41 ^{+0.03} _{-0.02}	0.65 ^{+0.08} _{-0.12}	1.43	1.11	0.55
Dra II	21.4 ^{+1.7} _{-1.1}	90.8 ^{+28.5} _{-14.3}	0.62 ^{+0.06} _{-0.04}	0.04 ^{+0.02} _{-0.02}	19.9 ^{+0.5} _{-0.5}	80.5 ^{+19.1} _{-10.8}	0.60 ^{+0.06} _{-0.04}	0.06 ^{+0.02} _{-0.02}	1.07	1.13	0.96
Eri II	114.4 ^{+80.9} _{-67.6}	440.9 ^{+158.3} _{-57.3}	0.57 ^{+0.22} _{-0.19}	0.85 ^{+0.07} _{-0.15}	212.9 ^{+69.1} _{-59.1}	454.5 ^{+160.5} _{-68.0}	0.64 ^{+0.19} _{-0.16}	0.75 ^{+0.08} _{-0.13}	0.54	0.97	0.03
For	76.7 ^{+43.1} _{-27.9}	152.7 ^{+9.7} _{-9.1}	0.33 ^{+0.17} _{-0.18}	0.96 ^{+0.02} _{-0.07}	85.2 ^{+38.6} _{-29.3}	160.0 ^{+24.7} _{-12.3}	0.31 ^{+0.14} _{-0.10}	0.87 ^{+0.07} _{-0.32}	0.90	0.95	0.00
Gru I	48.9 ^{+27.0} _{-22.9}	204.7 ^{+58.1} _{-23.9}	0.62 ^{+0.14} _{-0.09}	0.48 ^{+0.12} _{-0.21}	28.0 ^{+15.9} _{-13.4}	268.4 ^{+99.1} _{-45.0}	0.82 ^{+0.08} _{-0.07}	0.40 ^{+0.10} _{-0.12}	1.75	0.76	0.00
Gru II	27.2 ^{+8.4} _{-6.4}	64.6 ^{+5.3} _{-4.1}	0.41 ^{+0.08} _{-0.08}	0.62 ^{+0.08} _{-0.14}	24.8 ^{+5.1} _{-4.8}	72.4 ^{+10.6} _{-6.9}	0.50 ^{+0.04} _{-0.03}	0.54 ^{+0.09} _{-0.12}	1.10	0.89	0.00
Her	67.4 ^{+15.5} _{-16.1}	253.8 ^{+115.6} _{-53.1}	0.60 ^{+0.06} _{-0.04}	0.31 ^{+0.17} _{-0.15}	56.8 ^{+15.8} _{-15.0}	237.5 ^{+84.3} _{-40.0}	0.63 ^{+0.06} _{-0.05}	0.37 ^{+0.14} _{-0.16}	1.19	1.07	0.00
Hor I	67.6 ^{+13.5} _{-14.6}	81.3 ^{+5.5} _{-4.4}	0.09 ^{+0.11} _{-0.07}	0.84 ^{+0.10} _{-0.75}	68.0 ^{+10.5} _{-16.8}	91.2 ^{+35.8} _{-11.0}	0.19 ^{+0.10} _{-0.04}	0.49 ^{+0.37} _{-0.40}	0.99	0.89	0.60
Hyd II	99.2 ^{+30.6} _{-55.7}	237.3 ^{+191.2} _{-57.6}	0.56 ^{+0.14} _{-0.10}	0.41 ^{+0.35} _{-0.31}	80.4 ^{+27.5} _{-51.8}	214.6 ^{+208.6} _{-73.9}	0.61 ^{+0.11} _{-0.08}	0.34 ^{+0.32} _{-0.23}	1.23	1.11	0.06
Hyi I	45.8 ^{+16.1} _{-6.0}	142.8 ^{+191.5} _{-46.9}	0.46 ^{+0.22} _{-0.15}	0.00 ^{+0.00} _{-0.00}	25.3 ^{+0.5} _{-0.5}	132.4 ^{+63.6} _{-29.2}	0.68 ^{+0.09} _{-0.07}	0.00 ^{+0.00} _{-0.00}	1.81	1.08	1.00
Leo I	47.5 ^{+30.9} _{-24.0}	401.5 ^{+83.2} _{-45.8}	0.79 ^{+0.10} _{-0.09}	0.61 ^{+0.10} _{-0.14}	42.9 ^{+28.9} _{-23.2}	532.8 ^{+109.6} _{-86.3}	0.86 ^{+0.06} _{-0.06}	0.39 ^{+0.08} _{-0.08}	1.11	0.75	0.01
Leo II	61.4 ^{+62.3} _{-34.7}	230.0 ^{+17.6} _{-17.1}	0.58 ^{+0.22} _{-0.28}	1.00 ^{+0.00} _{-0.00}	54.3 ^{+55.7} _{-31.6}	240.1 ^{+16.7} _{-15.3}	0.63 ^{+0.20} _{-0.25}	0.98 ^{+0.01} _{-0.03}	1.13	0.96	0.03
Leo IV	66.8 ^{+60.7} _{-44.1}	153.7 ^{+87.1} _{-8.8}	0.44 ^{+0.30} _{-0.20}	1.00 ^{+0.00} _{-0.77}	81.8 ^{+73.2} _{-51.6}	153.7 ^{+87.0} _{-5.6}	0.38 ^{+0.34} _{-0.26}	1.00 ^{+0.00} _{-0.99}	0.82	1.00	0.05
Leo V	165.8 ^{+5.8} _{-49.2}	189.1 ^{+264.3} _{-30.5}	0.35 ^{+0.25} _{-0.22}	0.38 ^{+0.62} _{-0.37}	137.9 ^{+6.5} _{-55.4}	0.0 ^{+253.7} _{-35.0}	0.40 ^{+0.21} _{-0.16}	0.41 ^{+0.51} _{-0.39}	1.20		0.01
Peg III	141.0 ^{+87.8} _{-79.3}	251.5 ^{+234.0} _{-34.6}	0.25 ^{+0.31} _{-0.16}	0.79 ^{+0.15} _{-0.79}	162.6 ^{+49.4} _{-75.4}	252.6 ^{+267.4} _{-64.6}	0.35 ^{+0.26} _{-0.07}	0.68 ^{+0.23} _{-0.49}	0.87	1.00	0.01
Phx II	84.6 ^{+91.3} _{-35.6}	174.2 ^{+166.5} _{-95.1}	0.06 ^{+0.55} _{-0.05}	0.00 ^{+0.39} _{-0.00}	76.5 ^{+6.6} _{-10.0}	181.3 ^{+250.7} _{-106.9}	0.42 ^{+0.20} _{-0.20}	0.02 ^{+0.18} _{-0.02}	1.11	0.96	0.93
Pis II	130.5 ^{+70.1} _{-72.3}	265.7 ^{+304.3} _{-72.7}	0.27 ^{+0.31} _{-0.14}	0.53 ^{+0.32} _{-0.53}	147.3 ^{+26.2} _{-47.8}	248.6 ^{+250.8} _{-116.3}	0.39 ^{+0.10} _{-0.07}	0.32 ^{+0.48} _{-0.25}	0.89	1.07	0.01
Ret II	37.0 ^{+2.9} _{-5.3}	69.6 ^{+51.1} _{-20.9}	0.28 ^{+0.18} _{-0.09}	0.00 ^{+0.00} _{-0.00}	25.3 ^{+2.8} _{-3.1}	52.7 ^{+12.1} _{-7.8}	0.36 ^{+0.04} _{-0.02}	0.27 ^{+0.14} _{-0.11}	1.46	1.32	0.96
Ret III	55.1 ^{+32.8} _{-32.7}	164.1 ^{+127.4} _{-40.3}	0.59 ^{+0.16} _{-0.11}	0.37 ^{+0.24} _{-0.30}	55.5 ^{+30.0} _{-37.5}	117.1 ^{+124.7} _{-27.2}	0.47 ^{+0.22} _{-0.13}	0.54 ^{+0.29} _{-0.49}	0.99	1.40	0.00
Sgr II	68.7 ^{+9.6} _{-9.8}	93.1 ^{+24.3} _{-15.6}	0.16 ^{+0.09} _{-0.07}	0.00 ^{+0.11} _{-0.00}	46.9 ^{+8.5} _{-9.6}	116.3 ^{+63.7} _{-29.5}	0.44 ^{+0.09} _{-0.04}	0.24 ^{+0.20} _{-0.14}	1.47	0.80	0.00
Scl	44.9 ^{+4.3} _{-3.9}	145.7 ^{+25.2} _{-14.2}	0.54 ^{+0.04} _{-0.03}	0.39 ^{+0.08} _{-0.10}	55.0 ^{+5.5} _{-5.2}	105.3 ^{+11.4} _{-5.9}	0.32 ^{+0.02} _{-0.02}	0.58 ^{+0.11} _{-0.16}	0.82	1.38	0.00
Seg 1	19.8 ^{+4.2} _{-4.8}	47.9 ^{+20.1} _{-10.0}	0.44 ^{+0.06} _{-0.03}	0.29 ^{+0.19} _{-0.16}	19.5 ^{+4.3} _{-4.9}	48.5 ^{+20.3} _{-10.8}	0.45 ^{+0.06} _{-0.03}	0.29 ^{+0.20} _{-0.16}	1.02	0.99	0.00
Seg 2	18.0 ^{+3.8} _{-3.1}	48.2 ^{+3.5} _{-3.2}	0.45 ^{+0.05} _{-0.06}	0.82 ^{+0.03} _{-0.05}	17.4 ^{+3.9} _{-2.9}	46.0 ^{+3.3} _{-3.0}	0.45 ^{+0.05} _{-0.06}	0.88 ^{+0.03} _{-0.04}	1.04	1.05	0.00
Sxt	82.2 ^{+3.8} _{-4.3}	143.7 ^{+48.2} _{-25.7}	0.27 ^{+0.11} _{-0.07}	0.22 ^{+0.20} _{-0.11}	82.8 ^{+3.7} _{-4.0}	196.4 ^{+82.4} _{-38.5}	0.41 ^{+0.12} _{-0.08}	0.11 ^{+0.08} _{-0.06}	0.99	0.73	0.00
Tri II	12.2 ^{+1.5} _{-1.3}	85.6 ^{+12.7} _{-7.7}	0.75 ^{+0.03} _{-0.02}	0.31 ^{+0.04} _{-0.05}	12.6 ^{+1.1} _{-1.1}	100.1 ^{+21.8} _{-11.8}	0.78 ^{+0.03} _{-0.02}	0.25 ^{+0.04} _{-0.05}	0.97	0.86	0.00
Tuc II	44.8 ^{+12.3} _{-10.1}	114.4 ^{+35.8} _{-20.6}	0.45 ^{+0.05} _{-0.05}	0.13 ^{+0.15} _{-0.13}	35.6 ^{+4.5} _{-4.8}	178.9 ^{+104.1} _{-48.0}	0.67 ^{+0.08} _{-0.05}	0.13 ^{+0.07} _{-0.06}	1.26	0.64	0.00
Tuc III	1.0 ^{+0.4} _{-0.4}	42.0 ^{+3.3} _{-2.7}	0.95 ^{+0.02} _{-0.02}	0.49 ^{+0.02} _{-0.03}	3.2 ^{+0.2} _{-0.2}	38.5 ^{+2.5} _{-2.1}	0.85 ^{+0.01} _{-0.01}	0.51 ^{+0.02} _{-0.03}	0.32	1.09	0.00
Tuc IV	32.1 ^{+18.5} _{-12.6}	52.7 ^{+5.7} _{-4.2}	0.25 ^{+0.18} _{-0.18}	0.59 ^{+0.15} _{-0.59}	28.7 ^{+9.4} _{-9.1}	60.4 ^{+22.3} _{-10.6}	0.38 ^{+0.08} _{-0.04}	0.50 ^{+0.21} _{-0.27}	1.12	0.87	0.25
Tuc V	30.8 ^{+14.3} _{-9.4}	70.5 ^{+16.6} _{-9.5}	0.40 ^{+0.09} _{-0.07}	0.52 ^{+0.13} _{-0.28}	24.4 ^{+10.4} _{-8.5}	94.1 ^{+47.6} _{-20.4}	0.61 ^{+0.07} _{-0.04}	0.39 ^{+0.17} _{-0.20}	1.26	0.75	0.00
UMa I	49.9 ^{+46.2} _{-15.6}	103.5 ^{+7.6} _{-7.4}	0.35 ^{+0.13} _{-0.20}	0.98 ^{+0.02} _{-0.08}	46.5 ^{+26.0} _{-16.0}	102.1 ^{+6.2} _{-5.8}	0.37 ^{+0.15} _{-0.18}	1.00 ^{+0.00} _{-0.00}	1.07	1.01	0.00
UMa II	41.4 ^{+3.4} _{-3.6}	83.3 ^{+31.7} _{-19.2}	0.34 ^{+0.11} _{-0.08}	0.00 ^{+0.04} _{-0.00}	39.3 ^{+2.3} _{-2.6}	102.1 ^{+55.4} _{-28.8}	0.44 ^{+0.14} _{-0.11}	0.02 ^{+0.03} _{-0.01}	1.05	0.82	0.00
UMi	55.7 ^{+8.4} _{-7.0}	99.8 ^{+13.0} _{-8.4}	0.29 ^{+0.03} _{-0.03}	0.51 ^{+0.13} _{-0.20}	41.8 ^{+5.3} _{-4.5}	91.4 ^{+7.4} _{-5.8}	0.37 ^{+0.03} _{-0.03}	0.74 ^{+0.06} _{-0.10}	1.33	1.09	0.65
Wil 1	16.2 ^{+5.2} _{-3.0}	41.9 ^{+6.7} _{-6.6}	0.42 ^{+0.08} _{-0.09}	1.00 ^{+0.00} _{-0.00}	18.7 ^{+6.4} _{-3.7}	43.1 ^{+7.1} _{-7.0}	0.38 ^{+0.08} _{-0.09}	0.99 ^{+0.00} _{-0.01}	0.86	0.97	0.00

NOTE—Columns with the superscript ‘nL’ are orbital parameters without the influence of the LMC.

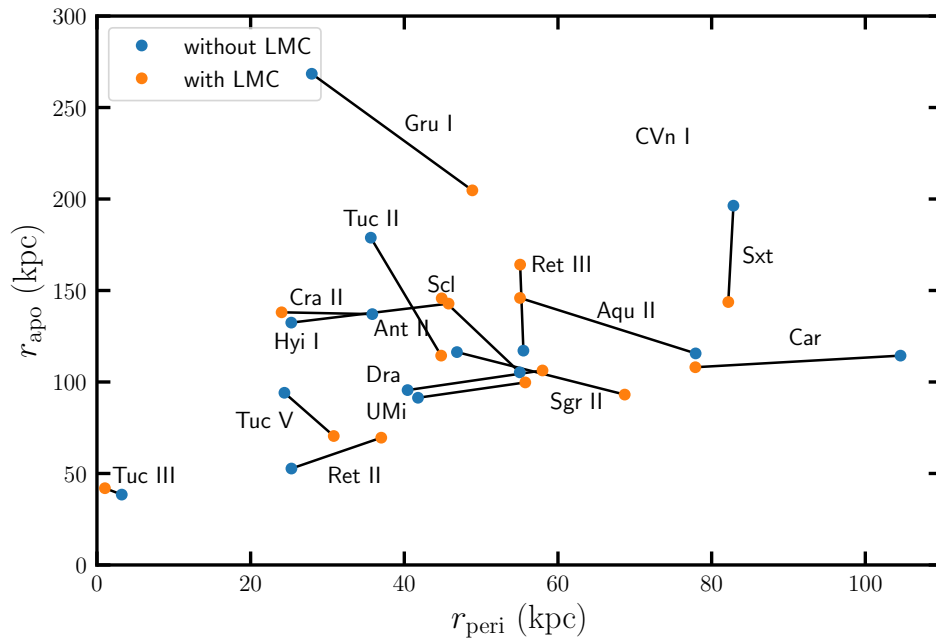


Figure 4. Comparison of the orbital pericenter and apocenter of dSphs with a large relative change ($> 25\%$ in either) in Milky Way potentials with (orange points) and without (blue points) the presence of the LMC.

icantly affect models of when they were accreted. Col I and Leo V meet this criteria, but Col I contains a much larger pericenter and apocenter than the other dSphs and Leo V is unbound without the presence of the LMC.

For the probability of being an LMC satellite, we use the approach of Patel et al. (2020): for each dwarf we determine whether it was within the escape velocity of the LMC at its most recent closest approach to the LMC. We note that we also tried the method of Erkal & Belokurov (2020) who instead evaluated whether the satellite was energetically bound to the LMC 5 Gyr ago. Since we are sampling over a wide range of Milky Way potentials and LMC masses, as opposed to Erkal & Belokurov (2020) who used a single Milky Way potential and a discrete set of LMC masses, this method does not seem to be as robust as the approach of Patel et al. (2020). This also agrees with the results of D’Souza & Bell (2022) who show that the accuracy of orbits decrease with increased lookback time. We discuss the LMC connection of the satellites in more detail in Section 5.4.

5. DISCUSSION

5.1. Tidal influence of the Milky Way

There has been extensive discussion on the tidal influence of the MW on its dSph population and here we compare our orbital parameters to some commonly used diagnostics. To directly address whether a satellite can be tidally influenced, we compare the average dSph density within the half-light radii to twice the average MW density at the orbital pericenter in Figure 5. This follows from the tidal radius assuming a flat rotation curve for the Milky Way and that the dwarf is on a circular orbit (King 1962):

$$r_t = r \left(\frac{m}{2M(< r)} \right)^{\frac{1}{3}}, \quad (5)$$

where r_t is the tidal radius, r is the distance from the Milky Way, m is the mass of the dwarf, and $M(< r)$ is the enclosed Milky Way’s mass within r . Re-arranging this and re-calling that we expect strong disruption when the half-light radius is similar to the tidal radius, the condition is:

$$\frac{m_{1/2}}{r_{1/2}^3} = \frac{2M(< r)}{r^3} \quad (6)$$

which implies our condition of $\rho_{1/2} = 2\bar{\rho}_{MW}$. To calculate $m_{1/2}$ for the dSphs, we use the dynamical mass estimator from Wolf et al. (2010). We additionally in-

clude the Sagittarius (Sgr) dSph² in Figure 5 and our tidal disruption analysis. Sgr is undergoing tidal disruption (e.g., Vasiliev et al. 2021) and was excluded from our mixture model analysis due to its large angular size and low Galactic latitude.

In Figure 5, there are a total of 11 dSphs with $\rho_{1/2}/\rho_{MW}(r = r_{\text{peri}}) \lesssim 10$ that could have tidal influences. Two of these, Car II and Hyi I, are likely LMC satellites (see Section 5.4) and we exclude them from this discussion as their past dynamical evolution has primarily been influenced by the LMC and they are on near their first pericenter in the MW. Three of the dSphs below the average MW density are clearly tidally disrupting based on independent literature analysis (Ant II, Sgr, and Tuc III) and we denote them with orange symbols in Figure 5. Tuc III has clear tidal tails extending $\sim 2^\circ$ from the satellite (Drlica-Wagner et al. 2015; Shipp et al. 2018) and there is velocity gradient along the tidal tails (Li et al. 2018b). Ant II has a velocity gradient that aligns with the orbital direction and there is qualitative agreement between tidal stripping models and Ant II’s kinematic and spatial properties (Ji et al. 2021; Vivas et al. 2022).

We denote the other six dSphs with $\rho_{1/2}/\rho_{MW}(r = r_{\text{peri}}) \lesssim 10$ as potentially disrupting (Boo I, Boo III, Cra II, Gru II, Seg 2, and Tuc IV) and more observational evidence and/or detailed dynamical modeling is required to confidently assess the tidally disrupting scenario. Boo III has been argued to be tidally disrupting based on its large velocity dispersion (Carlin et al. 2009), its small pericenter ($r_{\text{peri}} \sim 12$ kpc) and possible connection to the Styx stream (Carlin & Sand 2018). Simon et al. (2020) noted that the tidal radius of Gru II is just larger than its physical size and may be vulnerable to tidal stripping. There is a tentative velocity gradient in Cra II and the tidal radius is less than the half-light radius but the predicted tidal features are beyond the range of current spectroscopic samples (Ji et al. 2021). For Boo I there is a potential velocity gradient (Longeard et al. 2021b) and there are several blue horizontal branch star candidates at large distances, outside the King limiting radius (Filion & Wyse 2021) which are both consistent with tidal stripping models (Longeard et al. 2021b; Filion & Wyse 2021). Tuc IV has had a recent, direct ($\Delta d \sim 4$ kpc) collision with the LMC (Simon et al. 2020). Tidal stripping has been used as

² Sgr is not in our primary sample and the systemic proper motion and orbital motion was not derived in this work. For reference, we use $r_{\text{peri}} \sim 16$ kpc (Vasiliev et al. 2021), $\sigma \sim 15$ km s⁻¹ (Vasiliev & Belokurov 2020), and $r_h \sim 2500$ pc and $\epsilon \sim 0.64$ (McConnachie 2012).

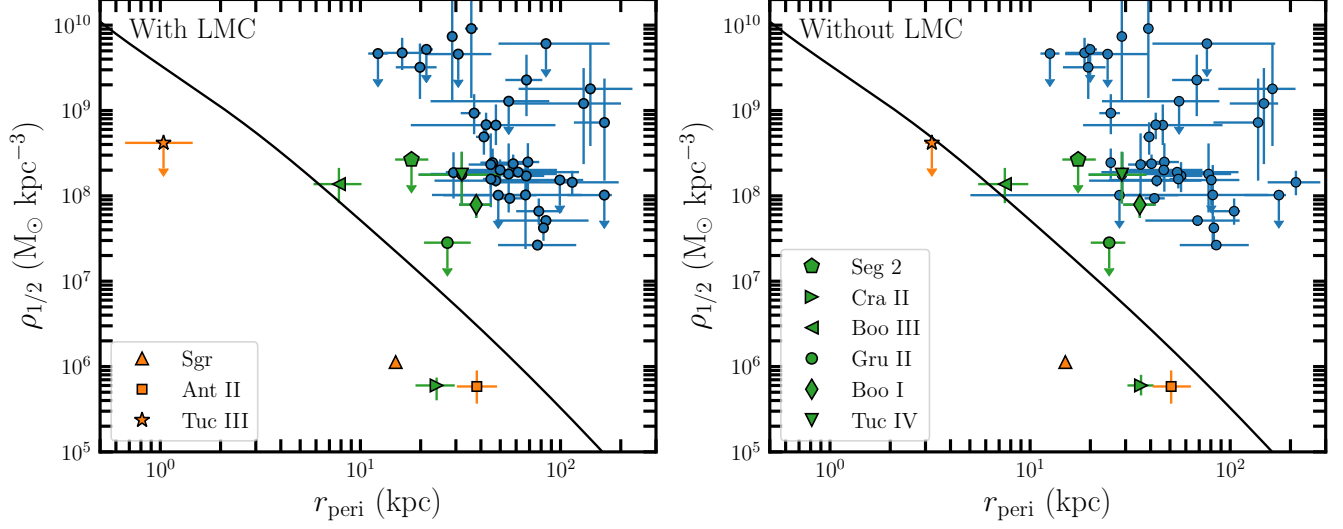


Figure 5. Comparison of the pericenter (r_{peri}) with and without the LMC influence (left panel and right panel, respectively) versus the average density within the half-light radius calculated from the stellar kinematics ($\rho_{1/2}$). The black line shows twice the enclosed MW density as a function of radius. If the satellite sits below this line, its Jacobi radius will be larger than the half-light radius and it will likely be tidal disrupting. Satellites near or below the curve are labeled. Orange symbols denote dSphs which are clearly tidally disrupting: Ant II, Sgr, and Tuc III. Whereas green symbols denote dSphs that are potentially undergoing tidal disruption and near the MW average density: Boo I, Boo III, Cra II, Gru II, Seg 2, and Tuc IV (see text for details).

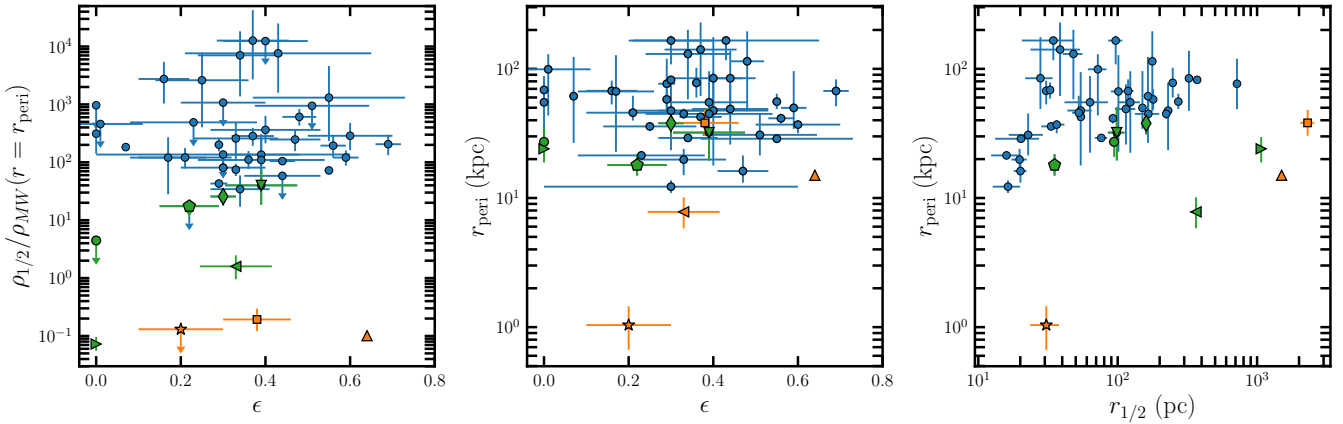


Figure 6. Correlation plots of dSphs in terms of their densities, ellipticities, pericenters, and half-light radii. Symbols and colors are the same as Figure 5. **Left panel:** Ellipticity (ϵ) versus the average dSph density divided by the average MW density at the dSph's pericenter ($\rho_{1/2}/\rho_{\text{MW}}(r = r_{\text{peri}})$). **Center panel:** Ellipticity (ϵ) versus pericenter (r_{peri}). **Right panel:** Half-light radius ($r_{1/2}$) vs pericenter (r_{peri}). There is no clear trend for pericenter or the average density ratio with ellipticity (left and middle panel). The dSphs with evidence of tidal disruption and the smallest $\rho_{1/2}/\rho_{\text{MW}}(r = r_{\text{peri}})$ ratios have larger half-light radii at a fixed pericenter than the general dSph population (right panel).

an explanation for why is offset from the stellar mass-metallicity relation (Kirby et al. 2013). No detailed tidal stripping models have been carried out for Boo III, Gru II, Seg 2, or Tuc IV. These dSphs are prime targets for searches for direct evidence of tidal disruption and/or detailed dynamical modeling.

There are other satellites that have small pericenters ($r_{\text{peri}} < 30$ kpc; Car III, Dra II, Seg 1, Tri II, and Wil 1), but they all have larger average densities and are therefore resilient to the tidal influence of the MW. We note that if the velocity dispersion was over-estimated these satellites could be undergoing tidal disruption by the MW (e.g., from unresolved binaries Minor et al. 2019,

or from small sample sizes). Some of the dSphs have upper limits on their velocity dispersion and if we assume a value of $\sigma_{\text{los}} \sim 1 \text{ km s}^{-1}$, we would infer density ratios of $\rho_{1/2}/\rho_{\text{MW}}(r = r_{\text{peri}}) \sim 2, 8, 9$ for Gru II, Seg 2, and Tri II, respectively and they would be considered prime candidates for tidal influence.

A large ellipticity has previously been used as evidence for tidal disruption (e.g., [Muñoz et al. 2010](#); [Küpper et al. 2017](#)). In Figure 6, we compare the ellipticity, the stellar half-light radius, the ratio of average dSph density to MW density, and the orbital pericenters. We see no clear trend with the average density ratio or pericenter with the ellipticity. This agrees with conclusions from N -body simulations that high ellipticity does not imply tidal disruption ([Muñoz et al. 2008](#)). It is interesting that roughly half the dSphs with low density ratios are nearly spherical (Cra II, Gru II, Seg 2, Tuc III) while the other half are elongated (Ant II, Boo I, Boo III, Sgr, Tuc IV). Clearly, there is some additional dependence on orbital phase for whether a large ellipticity would be observed in a disrupting satellite. The right-hand panel of Figure 6 compares the spherically averaged half-light radius and the pericenter. At a fixed pericenter, dSphs that have some indications (Boo III and Cra II) or are likely tidally disrupting (Ant II, Sgr, and Tuc III) have larger sizes than the general dSph population. The exceptions to this trend (Boo I, Gru II, Seg 2, and Tuc IV) may be in an earlier stage of disruption than the other likely disrupting dwarfs. We similarly examined the mass-to-light ratio of the dSphs and did not see any trends when comparing to orbital properties and direct tidal indicators.

5.2. Is Orientation a Signature of Tidal Disruption?

Next, we explore the relationship between the direction of the orbital motion and the orientation of each satellite. Specially, we compute the difference between the position angle (θ_{xy}) and the direction of the reflex-corrected proper motion (i.e., the orbital direction, θ_{μ}). In the left and center left panels of Figure 7, we compare $|\theta_{\mu} - \theta_{\text{xy}}|$ to the pericenter and ellipticity, respectively. We have excluded dSphs where the orbital direction and/or position angle are poorly measured ($\sigma_{\theta_{\mu}}, \sigma_{\theta_{\text{xy}}} > 25^{\circ}$).

The right-hand panels of Figure 7 show the $|\theta_{\mu} - \theta_{\text{xy}}|$ distribution of the dSph sample. To construct the global satellite $|\theta_{\mu} - \theta_{\text{xy}}|$, we have sampled each dSph's $|\theta_{\mu} - \theta_{\text{xy}}|$ distribution 1000 times with an error determined by adding the error from the position angle and reflex-corrected proper motion in quadrature. The center right panel shows the dSph sample ($\sigma_{\theta_{\mu}}, \sigma_{\theta_{\text{xy}}} < 25^{\circ}$) and a subset (black bins) with more precise measurements

($\sigma_{\theta_{\mu}}, \sigma_{\theta_{\text{xy}}} < 15^{\circ}$). There is an excess of satellites whose shape is aligned with their orbital motion and this correlation becomes more significant when poorly measured dSphs are removed. The right hand panel splits the same sample by ellipticity (at $\epsilon = 0.4$). dSphs with large ellipticities are in general aligned with their orbital motion whereas less elliptical dSphs have uniform orientations. In particular, there are six dSphs with $|\theta_{\mu} - \theta_{\text{xy}}| < 15^{\circ}$ (Her, Phx II, UMa I, UMa II, UMi, and Wil 1). The two dSphs with high ellipticity that are not aligned, Car III and Ret II, are both highly likely to be LMC satellites and the LMC association likely affects their orientation relative to the MW.

Several of the disrupting dSphs are excluded from the orientation sample due to their sphericity (Cra II, Gru II, and Tuc III) and most of the elliptical disrupting dSphs are aligned with the orbital motion. The exception in Figure 7, is Seg 2 which has a low ellipticity ($\epsilon \sim 0.2$). The core of Tuc III is spherical ($\epsilon \sim 0.2$), and the Tuc III tidal tails are aligned with the reflex-corrected proper motion ([Shipp et al. 2019](#)). Ant II, Boo I, Boo III, and Tuc IV all have the orbital motion aligned with the major axis. Similarly, the orientation of the Sgr dSph is aligned with its orbital motion though it is not in our nominal sample (e.g., [del Pino et al. 2021](#)).

We have further compared the orientation of each satellite to the direction of the Galactic center and the orbital direction with the direction to the Galactic center. The only trend is an excess of satellites with an orbital direction that is perpendicular to the direction to the Galactic center. If the likely LMC satellites are removed this excess is removed.

Thus, the only alignment that we find is that satellites with large ellipticity tend to be oriented along their orbit. While tidal disruption would be a natural explanation for this, there is no corresponding trend with small pericenters or low average density compared to the average MW density. A possible explanation for this alignment is tidal torques. Based on numerical simulations, there is an expected radial alignment between satellite orientation and the Galactic center due to tidal torques ([Pereira et al. 2008](#)). However, the orientation changes throughout orbit and we do not have a complete sample of MW satellites. Previous work has found that the MW dSphs share a common orientation and that it may be related to the Vast Polar Orbital structure ([Sanders & Evans 2017](#)). The Vast Polar Orbital structure and orbital poles alignment may be caused by the LMC ([Garavito-Camargo et al. 2021](#)) but [Pawlowski et al. \(2021\)](#) show the magnitude of the LMC perturbation is too small to fully explain the Vast Polar Orbital structure.

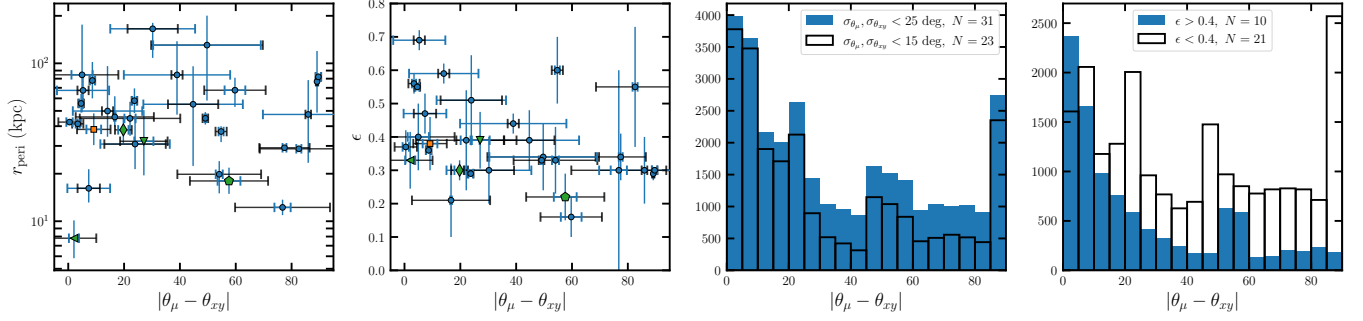


Figure 7. Comparison between the orbital direction and spatial orientation of the dSphs. Symbols and colors follow Figure 5. (left) Difference between the reflex-corrected proper motion (i.e. the orbital direction) and the position angle (i.e. spatial orientation) $|\theta_\mu - \theta_{xy}|$ versus the pericenter. When $|\theta_\mu - \theta_{xy}| \sim 0$ the orbit and major axis of the dSph are aligned. The blue error bar is from the reflex corrected proper motion and the black error bar is due to the distribution in the position angle. (center left) $|\theta_\mu - \theta_{xy}|$ versus the ellipticity of the dSph. (center right) Histogram of $|\theta_\mu - \theta_{xy}|$ for the same sample. To simulate errors we draw from each dSph’s $|\theta_\mu - \theta_{xy}|$ distribution 1000 times. The black bins are a subset of dSphs with smaller uncertainties. There is an excess of dSphs aligned with their orbital motion. (right) Histogram of $|\theta_\mu - \theta_{xy}|$ but separated by ellipticity. The blue bins are the elongated sample ($\epsilon > 0.4$). There is a clear preference for systems with large ellipticity to align with their orbital direction.

5.3. Comparison to Previous Results and Spectroscopic Catalogs

Overall, we find excellent agreement between our results and other *Gaia* EDR3 proper motion results³ (McConnachie & Venn 2020b; Li et al. 2021; Martínez-García et al. 2021; Vitral 2021; Battaglia et al. 2022; Qi et al. 2022). In particular, McConnachie & Venn (2020b); Battaglia et al. (2022) apply similar mixture models based on spatial position and proper motion with an additional color-magnitude component based on *Gaia* photometry. Similar to Pace & Li (2019) with *Gaia* DR2 data, we advocate for the use of auxiliary photometry especially for faint stars to assist with the identification of dSph members but acknowledge that the addition of a color-magnitude likelihood term is valuable to identify dSph stars. The distribution of MW stars is not uniform in color-magnitude space and including that information in the mixture model is valuable. McConnachie & Venn (2020b) include a prior on the systemic proper

motions that requires the corresponding tangential velocity to be bound to the MW. For *Gaia* DR2 measurements this affected a large number of dwarfs relative to other measurements (McConnachie & Venn 2020a). With EDR3, this prior generally only affects more distant satellites (> 100 kpc) with a low number of members (e.g. Boo IV, Leo IV, Leo V, Psc II, Peg III) and some distant dSphs have smaller proper motion errors than our results due to this prior. Previous *Gaia* DR2 results are commonly offset from the EDR3 results due to zero-point proper motion systematics in DR2 that have roughly decreased by a factor of two in EDR3 (Gaia Collaboration et al. 2021b). The EDR3 proper motions are more precise than previous *HST* measurements for Leo I and Leo II in contrast to the DR2 results.

Ultra-faint dwarfs have spectroscopic samples varying between 3 and ~ 70 members. We have compared current spectroscopic samples to our membership catalogs to assist in validating the method (i.e. to check we are correctly identifying known dSph members and MW foreground stars) and to identify the most promising targets for future followup. Here we consider a candidate as any stars with $p > 0.1$. In Table 4, we show the results of this exercise. In particular we list the number of expected members (N_{expected}) if all stars with $p > 0.1$ are targeted (N_{targets}). For almost all dSphs, we find excellent agreement between known spectroscopic dSph members and a high mixture model membership probability and a corresponding agreement between known spectroscopic MW foreground stars and a low or zero membership probability from our mixture model. One object with disagreement is Wil 1 as several previously identified spectroscopic members are identified as MW

³ We have also compared our proper motion results to previous *Gaia* DR2 results (Torrealba et al. 2019; Chakrabarti et al. 2019; McConnachie & Venn 2020a; Kallivayalil et al. 2018; Fritz et al. 2018a; Gaia Collaboration et al. 2018; Simon 2018; Carlin & Sand 2018; Massari & Helmi 2018; Mau et al. 2020; Pace & Li 2019; Fritz et al. 2019; Fu et al. 2019; Walker et al. 2019; Longeard et al. 2018; Simon et al. 2021, 2020; Gregory et al. 2020; Mutlu-Pakdil et al. 2019; Longeard et al. 2020; Massari et al. 2018; Chiti et al. 2021; Pace et al. 2020) and to non-*Gaia* proper motion measurements (Piatek et al. 2003; Walker et al. 2008; Pryor et al. 2015; Casetti-Dinescu & Girard 2016; Sohn et al. 2017; Piatek et al. 2002; Dinescu et al. 2004; Piatek et al. 2007; Méndez et al. 2011; Sohn et al. 2013; Lépine et al. 2011; Piatek et al. 2016, 2006; Fritz et al. 2018b; Casetti-Dinescu et al. 2018; Piatek et al. 2005). We include more details of this comparison in Appendix A.

Table 4. Summary of known spectroscopic members and potential targets of UFD galaxies

Dwarf	$N_{mem,F}$	$N_{targets}$	$N_{expected}$	$N_{mem,Gaia}$	$N_{mem,total}$	Spectroscopy citations
Aqu II	$17.5^{+2.1}_{-2.0}$	23	13.8	3	9	a
Boo I	$187.6^{+3.8}_{-3.9}$	202	140.0	46	100	b,c,d,e
Boo II	$23.2^{+1.2}_{-1.2}$	23	16.7	6	6	f,g
Boo III	$114.6^{+10.0}_{-9.4}$	256	129.7	13	20	h
Boo IV	$6.7^{+0.6}_{-1.5}$	7	6.8	0	0	
CVn II	$16.3^{+0.4}_{-0.5}$	4	2.3	14	25	i
Car II	$65.1^{+4.0}_{-4.0}$	72	39.4	17	18	j,k
Car III	$10.0^{+1.9}_{-1.4}$	9	4.6	5	5	j,k
Cen I	$28.1^{+2.3}_{-2.3}$	37	26.6	0	0	
Cet II	$7.9^{+0.5}_{-0.6}$	9	7.6	0	0	
Col I	$7.6^{+0.4}_{-0.3}$	3	2.9	5	9	l
CB	$42.2^{+1.2}_{-1.2}$	38	28.4	14	59	i
Dra II	$24.2^{+1.0}_{-1.2}$	19	14.3	10	14	m,n
Eri II	$21.6^{+0.5}_{-0.5}$	10	7.6	14	92	o,p
Gru I	$12.6^{+0.6}_{-0.6}$	6	5.5	7	7	q
Gru II	$40.1^{+3.7}_{-3.6}$	40	16.3	19	21	r
Her	$46.0^{+1.9}_{-2.1}$	27	16.3	28	59	i
Hor I	$18.9^{+0.5}_{-0.5}$	17	12.8	6	6	s,t
Hor II	$4.0^{+0.3}_{-0.3}$	4	3.9	0	3	l
Hyd II	$21.5^{+0.7}_{-0.8}$	17	15.0	6	13	u
Hyi I	$118.5^{+4.8}_{-4.8}$	133	77.8	31	31	v
Leo IV	$8.5^{+0.3}_{-0.2}$	3	1.5	7	25	i,e
Leo V	$8.4^{+0.2}_{-0.2}$	0	0.0	9	15	w,x,e
Peg III	$3.9^{+0.3}_{-0.4}$	4	3.9	0	7	y
Phx II	$12.7^{+0.5}_{-0.5}$	8	6.6	6	7	l
Pic I	$8.2^{+0.4}_{-0.4}$	9	8.2	0	0	
Pic II	$6.4^{+3.5}_{-2.5}$	8	6.0	0	0	
Ret II	$56.1^{+1.7}_{-1.6}$	32	22.2	29	29	z,aa,s
Ret III	$7.1^{+1.0}_{-1.6}$	6	4.0	2	3	l
Sgr II	$69.3^{+1.5}_{-1.5}$	55	42.0	24	39	ab
Seg 1	$26.7^{+3.0}_{-3.0}$	9	3.1	12	72	ac,ad
Seg 2	$19.7^{+0.9}_{-0.9}$	2	0.3	12	26	ae,af
Tri II	$11.8^{+1.7}_{-1.5}$	8	4.1	7	14	ag,ah
Tuc II	$43.3^{+5.2}_{-5.2}$	53	19.0	22	22	q,ai,aj
Tuc III	$56.3^{+5.8}_{-5.3}$	72	33.9	22	52	ak,al
Tuc IV	$12.2^{+2.5}_{-2.2}$	12	4.0	7	11	r
Tuc V	$6.5^{+1.2}_{-2.3}$	6	2.8	3	3	r
UMa I	$50.5^{+1.3}_{-1.3}$	32	24.2	24	40	am,c,i
UMa II	$51.8^{+2.5}_{-2.5}$	53	34.0	14	29	c,i
Wil 1	$9.0^{+1.1}_{-0.7}$	2	0.5	9	44	c,an

NOTE— $N_{mem,F}$ —total membership of each dSph with the complete sample, $N_{targets}$ —number of unobserved stars with $p > 0.1$, $N_{expected}$ —expected number of members if all targets are observed, $N_{mem,Gaia}$ —number of known members with astrometric solutions, $N_{mem,total}$ —total number of spectroscopic numbers. Citations: (a) (Torrealba et al. 2016b) (b) (Muñoz et al. 2006) (c) (Martin et al. 2007) (d) (Koposov et al. 2011) (e) (Jenkins et al. 2021) (f) (Koch et al. 2009) (g) (Ji et al. 2016) (h) (Carlin et al. 2009) (i) (Simon & Geha 2007) (j) (Li et al. 2018a) (k) (Ji et al. 2020) (l) (Fritz et al. 2019) (m) (Martin et al. 2016a) (n) (Longeard et al. 2018) (o) (Li et al. 2017) (p) (Zoutendijk et al. 2021) (q) (Walker et al. 2016) (r) (Simon et al. 2020) (s) (Koposov et al. 2015b) (t) (Nagasawa et al. 2018) (u) (Kirby et al. 2015) (v) (Koposov et al. 2018) (w) (Collins et al. 2017) (x) (Mutlu-Pakdil et al. 2019) (y) (Kim et al. 2016) (z) (Walker et al. 2015a) (aa) (Simon et al. 2015) (ab) (Longeard et al. 2020) (ac) (Norris et al. 2010) (ad) (Simon et al. 2011) (ae) (Kirby et al. 2013) (af) (Belokurov et al. 2009) (ag) (Martin et al. 2016b) (ah) (Kirby et al. 2017) (ai) (Chiti et al. 2018) (aj) (Chiti et al. 2021) (ak) (Simon et al. 2017) (al) (Li et al. 2018b) (am) (Kleyna et al. 2005) (an) (Willman et al. 2011)

stars based on *Gaia* astrometry. This disagreement is partly due to the difficulty in identifying spectroscopic members as the Wil 1 line-of-sight velocity overlaps with the MW distribution. Based on the total membership, there are several dwarfs where future spectroscopic observations with *Gaia* selected observations can double or triple the sample sizes (e.g., Aqu II, Boo II, Boo III, Dra II, Hyi I, Phx II, Ret II, Sgr II, UMa II). In addition, there are a number of bright candidates ($g < 18.5$) that are excellent targets for high resolution spectroscopic follow-up for detailed chemical abundance studies.

5.4. Association with the Large Magellanic Cloud

With full phase space information, it is possible to determine which dSphs were previously associated with the LMC prior to their infall into the MW (Deason et al. 2015; Jethwa et al. 2016; Sales et al. 2017; Kallivayalil et al. 2018; Fritz et al. 2019; Patel et al. 2020; Battaglia et al. 2022; Erkal & Belokurov 2020; Santos-Santos et al. 2021; Correa Magnus & Vasiliev 2022). To determine LMC association, we compute the fraction of orbits, p_{LMC} , where a dSph’s relative velocity ($v_{\text{LMC}, \text{min}}$) at its most recent approach to the LMC ($r_{\text{LMC}, \text{min}}$) is less than the LMC’s escape velocity. We include the p_{LMC} values for each dSph in Table 3. We show each dSph’s $r_{\text{LMC}, \text{min}}$ and $v_{\text{LMC}, \text{min}}$ in Figure 8, along with each dSphs current position and velocity relative to the LMC.

Based on our orbit modeling, we identify Car II, Car III, Hor I, Hyi I, Phx II, and Ret II as likely LMC satellites ($p_{\text{LMC}} > 0.5$). While five of the six dSphs we identify as LMC satellites are currently within the LMC’s escape velocity (Car II is currently $< 10 \text{ km s}^{-1}$ outside of the escape velocity), we note that the LMC’s Jacobi radius is likely lower today than in the past due to the proximity of the MW (Battaglia et al. 2022). The same six dSphs have been identified as likely LMC satellites in other studies with different methodology for determining association (Kallivayalil et al. 2018; Erkal & Belokurov 2020; Patel et al. 2020; Battaglia et al. 2022). For example, Erkal & Belokurov (2020) determine LMC association by computing the binding energy relative to the LMC after rewinding for 5 Gyr, or when the LMC reaches apocenter if that is earlier. Similarly, Correa Magnus & Vasiliev (2022) define a LMC satellite as one which was energetically bound to the LMC at some point between 1 to 3 Gyr ago. Battaglia et al. (2022) determine LMC association if the satellite was inside the LMC Jacobi radius at the time of closest approach. However, we note Correa Magnus & Vasiliev (2022) only consider five of the six to be likely associated and find Ret II to have a low probability of being associated. The different methodology used to identify

LMC satellites generally does not make a difference for these six objects (Car II, Car III, Hor I, Hyi I, Phx II, and Ret II) and they were likely previously associated with the LMC.

We find that Tuc IV has had a close encounter ($r_{\text{LMC}, \text{min}} \sim 3 \text{ kpc}$) with the LMC⁴ with a large relative velocity and is currently within the LMC escape velocity. Several studies have considered Tuc IV to have a low probability of being associated with the LMC (Simon et al. 2020; Battaglia et al. 2022). Similar to Tuc IV, we find that Sgr II, Tuc III, and Tuc V have had close encounters ($r_{\text{LMC}, \text{min}} \sim 10\text{--}20 \text{ kpc}$) but with much larger relative velocities ($v_{\text{LMC}, \text{min}} \sim 300\text{--}400 \text{ km s}^{-1}$). Of these, Sgr II is currently near the LMC’s escape velocity, however it is unlikely to be associated as it is closer to the MW.

While Dra, Dra II, and UMi also pass our association criteria based on their relative velocity being less than the LMC escape velocity at their closest approach, they were closer to the MW at this time and their Milky Way apocenters are less than $r_{\text{min}, \text{LMC}}$. Thus, the low relative velocity is just fortuitous. Dra II has been noted to have a potential LMC association if the LMC was on its second pericenter, a scenario which is increasingly unlikely (Kallivayalil et al. 2018). Similarly, in some orbits the relative velocity of Car and Cra II are less than the LMC escape velocity at $r_{\text{LMC}, \text{min}}$ but both are more distant than 100 kpc from the LMC at this time and the MW has had a larger influence on them. Finally, Gru II is the next closest satellite in phase space relative to the LMC, both at the present day and during its closest approach. It is considered a recently captured satellite by Battaglia et al. (2022).

5.5. On the Excess of Satellites near Pericenter

Once systemic proper motions of most MW satellites were measured with *Gaia* DR2, subsequent orbital analysis revealed an excess of satellites near their orbital pericenter (Simon 2018; Fritz et al. 2018a). This is unexpected as a satellite spends more time near its orbital apocenter than its pericenter. To assess this issue with our data set, we follow Fritz et al. (2018a) and evaluate the ratio, $f_{\text{peri}} = (r_{\text{GC}} - r_{\text{peri}})/(r_{\text{apo}} - r_{\text{peri}})$, which is a proxy for the orbital phase in the radial direction. $f_{\text{peri}} = 0, 1$ corresponds to the satellite being at its pericenter or apocenter, respectively. With DR2 measurements, roughly half the dSph sample had $f_{\text{peri}} < 0.1$, however, the f_{peri} distribution becomes less extreme with a heavier MW (Fritz et al. 2018a).

⁴ Tuc IV has possibly undergone a three-body interaction with LMC and SMC (Simon et al. 2020).

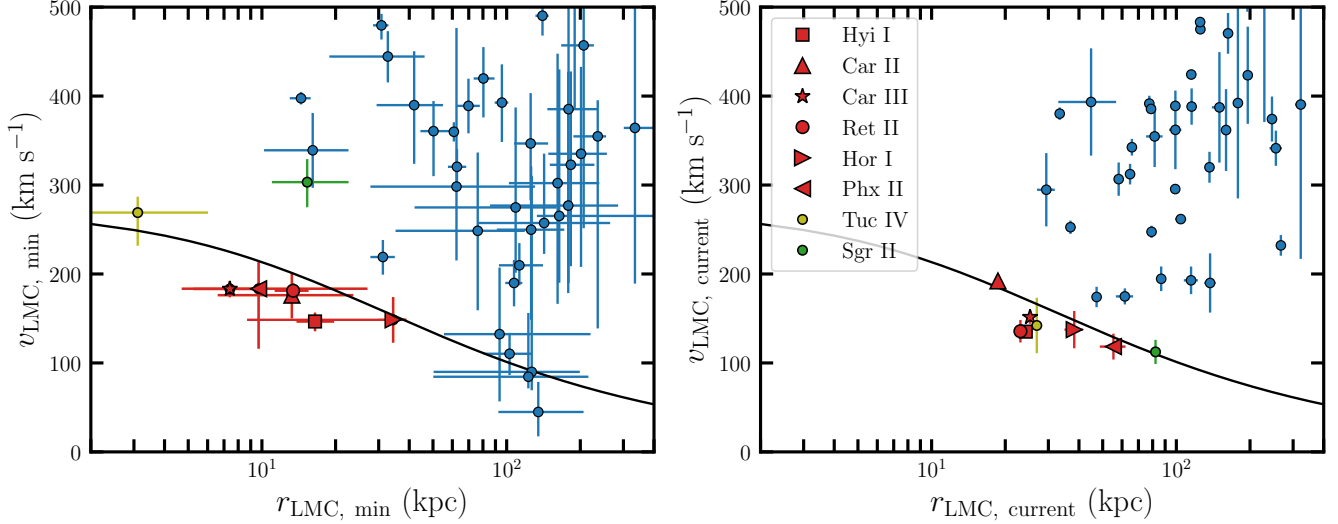


Figure 8. The distance to the LMC versus the relative velocity at each satellite’s previous closest LMC approach (left) and the current distance versus the current relative velocity (right). Red symbols denote the candidate LMC satellite population (Car II, Car III, Hyi I, Hor I, Phx II, Ret II). The black line is the LMC escape velocity curve with $M_{\text{LMC}} = 13.8 \times 10^{10} M_{\odot}$. The satellite with the closest approach is Tuc IV (gold circle) which is not considered an LMC satellite due to its large relative velocity. Currently, Sgr II (green symbol) is closer to the MW than the LMC and is more likely to be associated with the MW. The five satellites at large distances with low relative velocities (they are Dra, Dra II, UMi, Cra II, Car I) are not bound to the LMC. Most of them are closer to the MW at the time of closest approach.

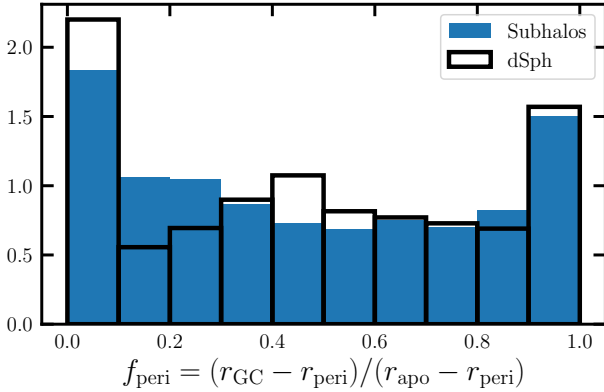


Figure 9. Pericenter fraction ($f_{\text{peri}} = (r_{\text{GC}} - r_{\text{peri}})/(r_{\text{apo}} - r_{\text{peri}})$) of observed dSphs (black) and subhalos (blue) from six MW-like N -body cosmological simulations. We exclude LMC dSphs and dSphs with large uncertainties from the observed sample (see text). For the observed sample, the bins are made from the Monte Carlo chains of each satellite. In both samples there are ‘excesses’ of satellites near pericenter and apocenter as the radial velocity is zero there and thus satellites spend relatively more time there.

We explore the f_{peri} distribution from our orbit modeling in Figure 9. We see an excess of MW satellites with $f_{\text{peri}} \sim 0$ and we see a secondary peak at $f_{\text{peri}} \sim 1$. We compute the fraction directly from the Monte Carlo samples. We exclude LMC satellites (Car II, Car III, Hor I, Hyi I, Phx II, Ret II) and dSphs with large tan-

gential velocity errors (Col I, Eri II, Hyd II, Leo IV, Leo V, Peg III, Psc II, and Ret III) following [Correa Magnus & Vasiliev \(2022\)](#). We note that in a number of cases there are satellites that are either closer than their previous pericenter⁵ (CB and UMa II) or more distant than their previous apocenter (Leo II, Sgr II, and Wil 1) and for these objects we use their current Galactocentric distance instead for the pericenter or apocenter. We note that this issue arises since we have defined the pericenter and apocenter as the local minimum and local maximum, respectively, and the dSphs have since had their orbits perturbed by the LMC. We note that both excluded samples (LMC satellites and large tangential errors) are preferentially near either their pericenter or apocenter.

To further examine this issue, we explore the f_{peri} distribution of subhalos in high-resolution cosmological N -body zoom-in simulations of MW-like halos. These simulations are described in detail in [Jethwa et al. \(2018\)](#). These simulations were run with the N -body part of GADGET-3 which is similar to GADGET-2 ([Springel 2005](#)). These simulations resolve Milky Way-like dark matter haloes with a particle mass of $2.27 \times 10^5 M_{\odot}$. From comparing with higher resolution runs, [Jethwa](#)

⁵ The LMC satellites, Car III, Hyi I, Phx II, and Ret II suffer from this issue but are already excluded from the analysis.

et al. (2018) found that the subhaloes in these simulations are complete down to a mass of $10^{7.5} M_\odot$, which is sufficient for comparing with the dwarfs in this work. Although these simulations are dark matter only, they include an analytical disk potential which is grown adiabatically from $z = 3$ to $z = 1$ (11 Gyr to 8 Gyr ago). This technique has been shown to mimic the depletion of subhaloes by baryonic disks (e.g., Garrison-Kimmel et al. 2017).

The subhaloes in this simulation are identified with ROCKSTAR (Behroozi et al. 2013a) and the merger trees are constructed with CONSISTENT TREES (Behroozi et al. 2013b). We measure the orbit of each subhalo by taking its position and velocity relative to the Milky Way in the final snapshot and computing the angular momentum and energy of its orbit. We then compute the turning points of the effective potential, $\phi_{\text{eff}}(r) = \frac{L^2}{2r^2} + \phi(r)$, where L is the total angular momentum and $\phi(r)$ is the gravitational potential of the Milky Way halo in the final snapshot. In total, there are 1576 subhalos with $r_{\text{GC}} < r_{\text{vir}}$ from six MW-like simulations.

The f_{peri} distribution of subhalos of MW-like dSphs is included in Figure 9. From the simulations, we see that the subhalo distribution peaks at both $f_{\text{peri}} \sim 0$ and $f_{\text{peri}} \sim 1$ which matches the dSph population. A pile-up at $f_{\text{peri}} \sim 0$ is not unexpected. These peaks occur as $\frac{d}{dt} f_{\text{peri}} \propto \frac{d}{dt} r_{\text{GC}} = 0$ at both pericenter and apocenter (Li et al. 2022). This is not a one-to-one comparison between the simulated subhalos and the observed dSph population, as there is no selection function applied to the simulated subhalos (e.g. Drlica-Wagner et al. 2020), and there are no observational errors applied to the simulations. Regardless, we find a general agreement between the f_{peri} distribution of the dSph and subhalo population. We leave a more detailed comparison between the orbital properties of the MW dSph population and simulated MW subhalo population to a future work.

The potential excess of satellites near their pericenter has been addressed by several other *Gaia* EDR3 based analyses. Li et al. (2021) examined the ratio of the time to reach or leave a satellite’s pericenter compared to half the total orbital period. Their analysis inferred an excess at lower values of this ratio while they expected a uniform distribution and they concluded that there remains a proximity-to-pericenter issue. Correa Magnus & Vasiliev (2022) examined the radial phase angle, the canonically conjugate variable to the radial action, and found that the dSph population is distributed uniformly in the radial phase angle. Correa Magnus & Vasiliev (2022) concluded that there is no proximity-to-pericenter issue due to the dSph population being well-

mixed in radial phase angle. Li et al. (2022) examined f_{peri} for the dSph population in a MW only potential and found a f_{peri} distribution similar to our analysis (see their Figure 5). They analyzed the globular cluster population and a dozen stellar streams and found peaks at $f_{\text{peri}} \sim 0, 1$, similar to the dSph population. Furthermore, Li et al. (2022) sampled dSph-like orbits uniformly in time at eccentricities of 0.2, 0.4, and 0.6 and found the f_{peri} distribution of these sampled orbits have peaks at $f_{\text{peri}} \sim 0, 1$. In summary, there is not an excess of satellites near their pericenter and the perceived excess was due to how the orbital phase was computed.

5.6. On the Anti-Correlation Between Pericenter and Density for Bright Satellites

There is a reported anti-correlation between the average dark matter density within 150 pc (ρ_{150}) and the pericenter (r_{peri}) in the classical dSphs + CVn I⁶ based on orbits computed with *Gaia* DR2 data (Kaplinghat et al. 2019). This correlation implies that only the densest dSphs can survive at small pericenters. In Figure 10, we update the pericenters with our results from EDR3 proper motions and include the effect of the LMC. For the dark matter distribution we use results from spherical Jeans dynamical models from Pace & Strigari (2019), which assume an NFW dark matter distribution (Navarro et al. 1996). Without the LMC, we find a general agreement with the previously reported correlation between r_{peri} and ρ_{150} . For the models with the LMC, we find the previously reported correlation is much weaker and steeper.

The dSphs, Ant II and CrA II, are in the same stellar mass range and should be included as they were likely initially hosted by similar mass haloes (given their similar stellar masses $> 10^5 M_\odot$) as the other classical dwarfs. They have much lower densities than the classical dwarfs pericenter which is likely a signature of their tidal disruption (Ji et al. 2021; Vivas et al. 2022) and their inclusion would similarly weaken the ρ_{150} - r_{peri} anti-correlation. However, the question remains, where are the dSphs with high density and a large pericenter.

A similar trend is observed in N -body simulations between the subhalo maximum circular velocity (V_{max}) and r_{peri} (Robles & Bullock 2021). At a fixed V_{max} , subhalos with smaller r_{peri} are more concentrated and more dense. Less concentrated halos are less resilient to tidal disruption. A similar trend has been observed when considering the distance to the host in that the closer subhalos have higher concentrations on average

⁶ This includes Car, CVn I, Dra, For, Leo I, Leo II, Scl, Sxt, and UMi.

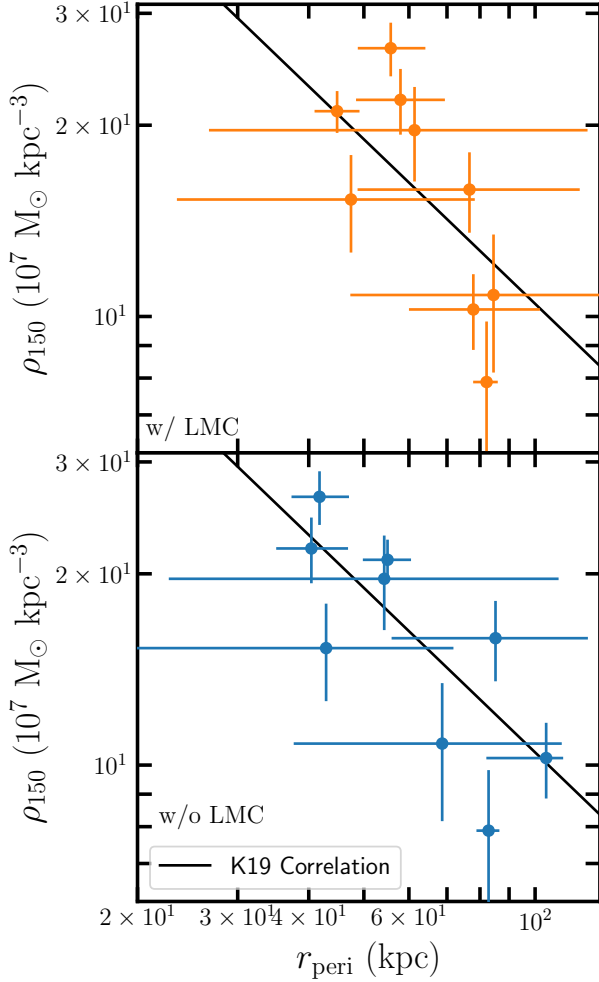


Figure 10. Total density within 150 pc (ρ_{150}) versus the pericenter (r_{peri}) for the classical satellites (Car, Dra, For, Leo I, Leo II, Scl, Sxt, and UMi.) and CVn I. The top and bottom panels show pericenter with and without the influence of the LMC. Overlaid is the correlation for a cuspy dark matter from [Kaplinghat et al. \(2019\)](#).

than more distant subhalos ([Moliné et al. 2021](#)). This observed trend between pericenter and dark matter density has been used to probe self-interacting dark matter (e.g., [Jiang et al. 2021](#)). Pericenter and orbital analysis will be useful priors for dynamical analysis ([Robles & Bullock 2021](#)) however, we caution that the LMC needs to be included for MW orbital analyses.

5.7. Dominant Source of Orbital Uncertainty

In this work we have considered many sources of error when evaluating the dwarf orbits: uncertainties in the present-day phase space coordinates of the dwarfs

(i.e. proper motions, distance, and radial velocity⁷), in the LMC model (i.e. its present day proper motions, distance, radial velocity, and mass), and the Milky Way potential. In order to explore which of these sources dominates the orbital uncertainty (i.e. in r_{peri} and r_{apo}), and thus which would be the most helpful to improve, we repeat our analysis and build three different suites with different assumptions about the uncertainties. We note that in this analysis, we use the Milky Way potential and associated uncertainties from [McMillan \(2017\)](#). In reality, there are larger uncertainties depending on what tracers and modelling techniques are used (e.g. [Wang et al. 2020](#)) and thus our Milky Way potential uncertainties should be seen as a conservative.

For the first suite, we start with the present day errors (i.e. the fiducial analysis of this work), and sequentially turn off each individual source of error, leaving the other errors at their present day values. We dub this the ‘present day’ suite. This results in 4 simulations where we (respectively) turn off the uncertainty in proper motion, distance, LMC, and MW potential. We show the present-day distance of each satellite compared to the relative reduction in orbital uncertainty when each source of uncertainty is fixed to zero (e.g., $\sigma_{r_{\text{peri}}, \text{fixed}}/\sigma_{r_{\text{peri}}}$) in Figure 11. The relative reduction in error on the pericenter and apocenter shows how much of the current error is due to the fixed quantity (i.e. if $\sigma_{r_{\text{peri}}, \text{fixed distance}}/\sigma_{r_{\text{peri}}}$ is close to 0 most of the error on the pericenter is due to the distance uncertainty and if it is close to 1 the uncertainty is due to other properties). In general for our dSph sample, the error in the pericenter is dominated by either the distance or systemic proper motion uncertainty. Whereas for the apocenter, the error is dominated by the distance or potential uncertainties. We note that we choose to plot this relative reduction in error versus distance to give a sense of where in the Milky Way each uncertainty dominates. We include the relative reduction in error for each dwarf in Table 5. We note that previous works have also explored the dominant source of uncertainty, but these have examined the uncertainty in the transverse velocity ([Battaglia et al. 2022](#)) instead of the orbital uncertainty as in this work.

In the second suite, we consider a future version of the first suite where the proper motions and distances are improved to a level we expect in the next 5 years. For the proper motions, we assume uncertainties based on 10 years of *Gaia* data (DR5). For the distances, we as-

⁷ The errors on the line-of-sight velocity and α , δ are minuscule compared to the listed properties.

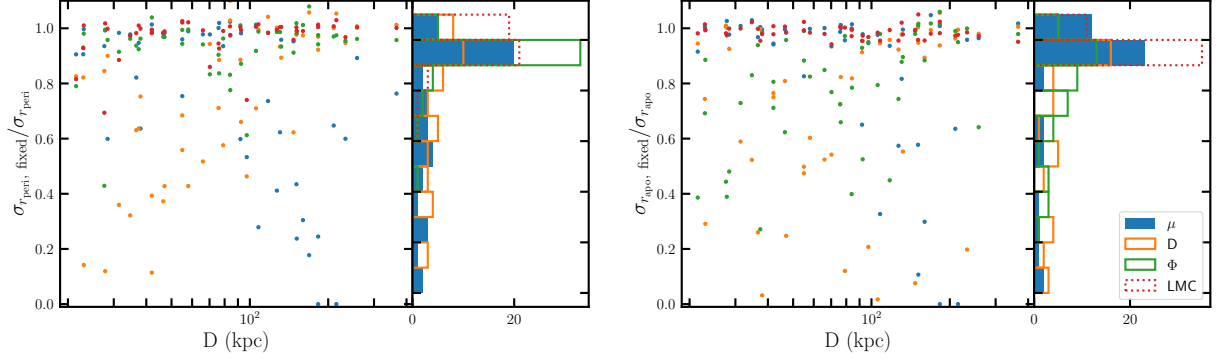


Figure 11. Relative fractional error compared to the distance for the pericenter ($\sigma_{r_{\text{peri}}}$; left panels) and apocenter ($\sigma_{r_{\text{apo}}}$; right panels) due to the fixing the error to zero for the systemic proper motion (blue points), distance (orange points), MW potential (green points), and LMC mass (red points). For each galaxy there are four entries and in each entry three of the previously mentioned errors are set to the current value and one is set to zero to analyze its impact. Low fractions correspond to the majority of current error being due to the fixed parameter and high fractions indicate that current error in the fixed property does not significantly affect the total error. The current error in the pericenter is dominated by the distance and/or proper motion uncertainties whereas the current error in the apocenter is dominated by the distance and/or potential uncertainties. To aid in interpreting the sources of error, we show a histogram of the fractional uncertainties next to each panel.

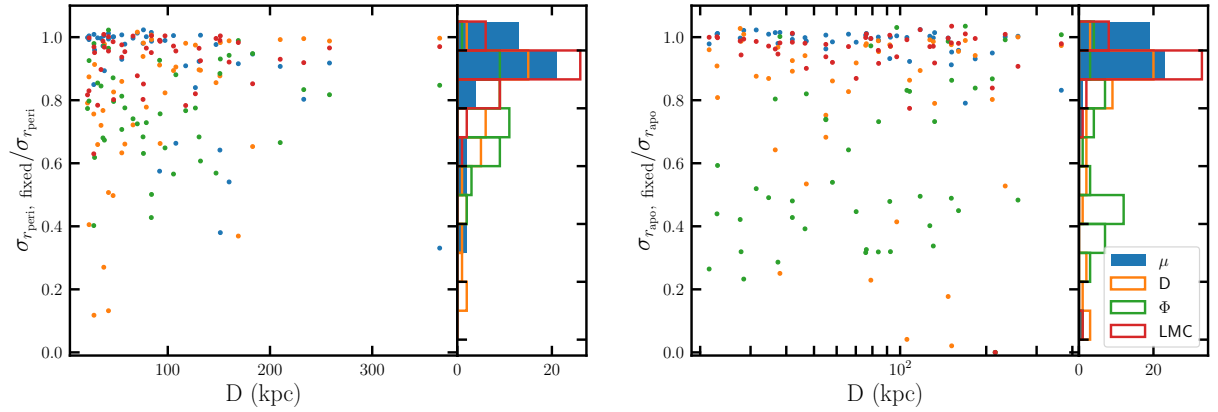


Figure 12. Similar to Figure 11 except here we start with the projected future errors and go to zero error for each component. The proper motion errors are based on *Gaia* DR5 projections, the errors on distance are assumed to be 2%, and the Milky Way and LMC uncertainties are left at their present-day values. The largest source of error in the future will be due to the distance and MW potential uncertainty which emphasizes the need to better measure the MW potential. Interestingly, some satellites near the LMC will be sensitive to improvements in the LMC.

sume a 2% error which is an obtainable projection given current systematics in the period-Wesenheit-metallicity relations of RR Lyrae stars (e.g., Nagarajan et al. 2021; Garofalo et al. 2022). We leave the uncertainties in the Milky Way potential and LMC potential at their present-day uncertainties to assess whether these need to be improved to make use of upcoming data. The results are shown in Figure 12. Due to improvements in the systemic proper motion in future *Gaia* data releases, the dominant errors in the future will be due to distance and/or MW potential uncertainties. This motivates the need for more precise measurements of the Milky Way potential in order to make optimal use of *Gaia* DR5

data. Measurements with stellar streams are excellent for this since they span a large range of radii and can disentangle the influence of the LMC (e.g. Küpper et al. 2015; Erkal et al. 2019; Vasiliev et al. 2021). Similarly, measurements based on distant tracers which include the effect of the LMC are also promising (e.g. Deason et al. 2021; Correa Magnus & Vasiliev 2022). Interestingly, we also see that there are some dwarfs which have a substantial uncertainty ($\gtrsim 20\%$) in their orbital properties due to the LMC uncertainties. We note that dwarfs with a small number of members in the *Gaia* data will be dominated by proper motion measurements.

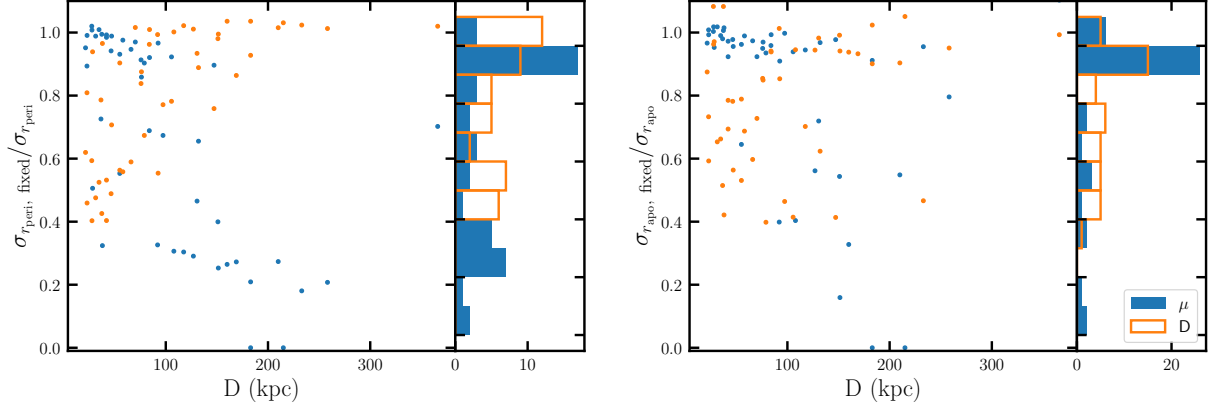


Figure 13. Similar to Figure 11 except the here we compare current proper motion errors to *Gaia* DR5 errors and compare 5% to 2% errors in the distance. For some objects 5% error in the distance is larger than their current error.

For the final suite, we take a slightly different approach where we start with current proper motion errors and 5% distance errors and (one at a time) improve these to projected 10-yr *Gaia* errors and 2% distance errors. We only include present-day uncertainties in the Milky Way potential in this test as it is difficult to make projections for the future uncertainties. The results of the orbital parameters are shown in Figure 13. For both the pericenter and apocenter errors, the closer dwarfs are dominated by distance errors whereas the more distant dwarfs are dominated by proper motion errors. We note that there are some dwarfs that currently have distance errors that are less than 5% and this exercise is done to compare how uniform improvement in distance and proper motion will affect different dSphs.

Overall, our analysis shows that while proper motions are currently one of the dominant sources of orbital uncertainty, once we have *Gaia* DR5 data, the main uncertainties will come from the distance and Milky Way potential. This motivates the need of improving our measurement of the Milky Way potential so that we can make optimal use of the upcoming data sets, especially in the outskirts since it makes a significant contribution to the uncertainty in apocenters.

6. CONCLUSION

We have presented a method to measure the systemic proper motion of MW satellites and applied it to 54 MW dSphs. Our methodology builds on previous work utilizing mixture models to cleanly separate the MW foreground from the dSph stars and uses *Gaia* astrometry combined with either DECam, *Gaia*, or Pan-Starrs photometry (Pace & Li 2019; McConnachie & Venn 2020a). Our primary results are:

- We have measured the systemic proper motion of 52 dSphs with two different background models

and have identified likely members. We publicly release our membership catalogs to enable spectroscopic follow-up analysis (see Appendix A).

- Our systemic proper motion measurements are in excellent agreement with other EDR3 analysis (e.g., McConnachie & Venn 2020b; Li et al. 2021; Battaglia et al. 2022). We have compared our candidate dSph members to spectroscopic catalogs and found that high probable proper motion members are confirmed with velocity measurements. In addition, future spectroscopic measurements in the following dSphs can significantly expand spectroscopic samples by factors of 2-3: Aqu II, Boo II, Boo III, Car II, Dra II, Hyd II, Hyi I, Ret II, Tuc II, and UMa II. Larger spectroscopic samples can improve our knowledge of the dynamical properties of the ultra-faint dwarfs (Table 4).
- For the 46 dSphs with literature line-of-sight velocities, we have simulated their orbits in the Milky Way and Milky Way+LMC system. For 16 of the dSphs, we found that including the LMC changes the pericenter or apocenter by $> 25\%$, showing that the LMC must be included for precise orbits (Figure 4).
- We have compared the orbital information here to some previously used diagnostics for searching for tidal influences on dSphs. Most directly we have compared the average dSph density to the average MW density at the dSph’s pericenter (Figure 5). dSphs that are clearly undergoing tidal disruption (Ant II, Sgr, and Tuc III) fall below the average MW density at their pericenter whereas other dSphs near the average MW density (Boo I, Boo III, Cra II, Gru II, Seg 2, and Tuc IV) are potentially tidally disrupting although future work is

required to confirm this. We do not observe any trends between ellipticity, pericenter, and susceptibility to tidal disruption suggesting that not all large elongation is due to tidal disruption (Figure 6). At a fixed pericenter, the dSphs with the smallest values of the ratio between the average dSph density and the average MW density at the dSph’s pericenter have larger half-light radii than the general dSph population.

- We have explored alignments between the spatial orientation of a dSph and its orbital direction (via it reflex corrected proper motion) and there is an excess of dSphs aligned with their orbital motion (Figure 7). Moreover, the most elliptical dSphs ($\epsilon > 0.4$) are preferentially aligned with their orbital direction. This may be evidence of large scale tidal torques on the dSph population from the MW.
- We have identified six dSphs that were likely associated with the LMC: Car II, Car III, Hor I, Hyi I, Phx II, and Ret II (Figure 8). Our association results agree with previous orbital analysis with *Gaia* DR2 and updated EDR3 results (Kallivayalil et al. 2018; Erkal & Belokurov 2020; Patel et al. 2020; Battaglia et al. 2022; Correa Magnus & Vasiliev 2022).
- Our analysis does not suggest there is an excess of satellites near their orbital pericenter in contrast to some previous *Gaia* DR2 results (Figure 9). We have examined the ratio f_{peri} and we have found pileups near $f_{\text{peri}} \sim 0, 1$ (i.e., pericenter and apocenter), similar to previous analyses. We have applied the same analysis to subhalos of MW-like halos in N -body simulations and find that the subhalo f_{peri} distribution agrees with the observed dSph distribution. This agrees with other analyses directly examining the orbital phase (e.g., Correa Magnus & Vasiliev 2022)
- We have examined how the orbital uncertainties of these dwarfs are affected by the observational uncertainties for each dwarf as well as the uncertainties in the MW and LMC potentials. This allows us to determine which of these sources currently dominates the dSph population and what the largest source of error will be at the end of the *Gaia* mission (Figures 11-13). In general, the current orbital pericenters are dominated by either distance and/or systemic proper motion errors whereas the current orbital apocenters are

dominated by the distance and/or potential uncertainty. In the future, both the orbital pericenters and apocenters will be dominated by distance and/or potential uncertainties except for dSphs with very small *Gaia* sample sizes.

The *Gaia* astrometric data sets (DR2, EDR3) have transformed our understanding of the orbital motion of the MW dSph population and enabled new analyses. The study of proper motions and internal tangential kinematics of MW dSphs and more distant dSphs is promising with the future *Gaia* data releases and future space based astrometry (e.g., Nancy Grace Roman Space Telescope).

ACKNOWLEDGMENTS

We thank Matt Walker and Sergey Kosopov for helpful discussions. We thank the referee for their constructive report. We thank Josh Simon and Dmitry Makarov for their helpful comments. ABP is supported by NSF grant AST-1813881. TSL acknowledges financial support from Natural Sciences and Engineering Research Council of Canada (NSERC) through grant RGPIN-2022-04794.

For the purpose of open access, the author has applied a Creative Commons Attribution (CC BY) licence to any Author Accepted Manuscript version arising from this submission.

This research has made use of the SIMBAD database, operated at CDS, Strasbourg, France (Wenger et al. 2000). This research has made use of NASA’s Astrophysics Data System Bibliographic Services.

This paper made use of the Whole Sky Database (wsdb) created by Sergey Koposov and maintained at the Institute of Astronomy, Cambridge by Sergey Koposov, Vasily Belokurov and Wyn Evans with financial support from the Science & Technology Facilities Council (STFC) and the European Research Council (ERC).

This work has made use of data from the European Space Agency (ESA) mission *Gaia* (<https://www.cosmos.esa.int/gaia>), processed by the *Gaia* Data Processing and Analysis Consortium (DPAC, <https://www.cosmos.esa.int/web/gaia/dpac/consortium>). Funding for the DPAC has been provided by national institutions, in particular the institutions participating in the *Gaia* Multilateral Agreement.

This project used public archival data from the Dark Energy Survey (DES). Funding for the DES Projects has been provided by the U.S. Department of Energy, the U.S. National Science Foundation, the Ministry of Science and Education of Spain, the Science and Technology Facilities Council of the United Kingdom, the

Higher Education Funding Council for England, the National Center for Supercomputing Applications at the University of Illinois at Urbana-Champaign, the Kavli Institute of Cosmological Physics at the University of Chicago, the Center for Cosmology and Astro-Particle Physics at the Ohio State University, the Mitchell Institute for Fundamental Physics and Astronomy at Texas A&M University, Financiadora de Estudos e Projetos, Fundação Carlos Chagas Filho de Amparo à Pesquisa do Estado do Rio de Janeiro, Conselho Nacional de Desenvolvimento Científico e Tecnológico and the Ministério da Ciência, Tecnologia e Inovação, the Deutsche Forschungsgemeinschaft, and the Collaborating Institutions in the Dark Energy Survey. The Collaborating Institutions are Argonne National Laboratory, the University of California at Santa Cruz, the University of Cambridge, Centro de Investigaciones Energéticas, Medioambientales y Tecnológicas-Madrid, the University of Chicago, University College London, the DES-Brazil Consortium, the University of Edinburgh, the Eidgenössische Technische Hochschule (ETH) Zürich, Fermi National Accelerator Laboratory, the University of Illinois at Urbana-Champaign, the Institut de Ciències de l'Espai (IEEC/CSIC), the Institut de Física d'Altes Energies, Lawrence Berkeley National Laboratory, the Ludwig-Maximilians Universität München and the associated Excellence Cluster Universe, the University of Michigan, the National Optical Astronomy Observatory, the University of Nottingham, The Ohio State University, the OzDES Membership Consortium, the University of Pennsylvania, the University of Portsmouth, SLAC National Accelerator Laboratory, Stanford University, the University of Sussex, and Texas A&M University. Based in part on observations at Cerro Tololo Inter-American Observatory, National Optical Astronomy Observatory, which is operated by the Association of Universities for Research in Astronomy (AURA) under a cooperative agreement with the National Science Foundation.

The Pan-STARRS1 Surveys (PS1) and the PS1 public science archive have been made possible through contributions by the Institute for Astronomy, the University of Hawaii, the Pan-STARRS Project Office, the Max-Planck Society and its participating institutes, the Max Planck Institute for Astronomy, Heidelberg and the Max Planck Institute for Extraterrestrial Physics, Garching, The Johns Hopkins University, Durham University, the University of Edinburgh, the Queen's University Belfast, the Harvard-Smithsonian Center for Astrophysics, the Las Cumbres Observatory Global Telescope Network Incorporated, the National Central University of Taiwan, the Space Telescope Science Institute, the National

Aeronautics and Space Administration under Grant No. NNX08AR22G issued through the Planetary Science Division of the NASA Science Mission Directorate, the National Science Foundation Grant No. AST-1238877, the University of Maryland, Eotvos Lorand University (ELTE), the Los Alamos National Laboratory, and the Gordon and Betty Moore Foundation.

The Legacy Surveys consist of three individual and complementary projects: the Dark Energy Camera Legacy Survey (DECaLS; Proposal ID #2014B-0404; PIs: David Schlegel and Arjun Dey), the Beijing-Arizona Sky Survey (BASS; NOAO Prop. ID #2015A-0801; PIs: Zhou Xu and Xiaohui Fan), and the Mayall z-band Legacy Survey (MzLS; Prop. ID #2016A-0453; PI: Arjun Dey). DECaLS, BASS and MzLS together include data obtained, respectively, at the Blanco telescope, Cerro Tololo Inter-American Observatory, NSF's NOIRLab; the Bok telescope, Steward Observatory, University of Arizona; and the Mayall telescope, Kitt Peak National Observatory, NOIRLab. The Legacy Surveys project is honored to be permitted to conduct astronomical research on Iolkam Du'ag (Kitt Peak), a mountain with particular significance to the Tohono O'odham Nation.

NOIRLab is operated by the Association of Universities for Research in Astronomy (AURA) under a cooperative agreement with the National Science Foundation.

This project used data obtained with the Dark Energy Camera (DECam), which was constructed by the Dark Energy Survey (DES) collaboration. Funding for the DES Projects has been provided by the U.S. Department of Energy, the U.S. National Science Foundation, the Ministry of Science and Education of Spain, the Science and Technology Facilities Council of the United Kingdom, the Higher Education Funding Council for England, the National Center for Supercomputing Applications at the University of Illinois at Urbana-Champaign, the Kavli Institute of Cosmological Physics at the University of Chicago, Center for Cosmology and Astro-Particle Physics at the Ohio State University, the Mitchell Institute for Fundamental Physics and Astronomy at Texas A&M University, Financiadora de Estudos e Projetos, Fundacao Carlos Chagas Filho de Amparo, Financiadora de Estudos e Projetos, Fundacao Carlos Chagas Filho de Amparo a Pesquisa do Estado do Rio de Janeiro, Conselho Nacional de Desenvolvimento Cientifico e Tecnologico and the Ministerio da Ciencia, Tecnologia e Inovacao, the Deutsche Forschungsgemeinschaft and the Collaborating Institutions in the Dark Energy Survey. The Collaborating Institutions are Argonne National Laboratory, the University of California at Santa Cruz, the University

of Cambridge, Centro de Investigaciones Energeticas, Medioambientales y Tecnologicas-Madrid, the University of Chicago, University College London, the DES-Brazil Consortium, the University of Edinburgh, the Eidgenossische Technische Hochschule (ETH) Zurich, Fermi National Accelerator Laboratory, the University of Illinois at Urbana-Champaign, the Institut de Ciencies de l'Espai (IEEC/CSIC), the Institut de Fisica d'Altes Energies, Lawrence Berkeley National Laboratory, the Ludwig Maximilians Universitat Munchen and the associated Excellence Cluster Universe, the University of Michigan, NSF's NOIRLab, the University of Nottingham, the Ohio State University, the University of Pennsylvania, the University of Portsmouth, SLAC National Accelerator Laboratory, Stanford University, the University of Sussex, and Texas A&M University.

The Legacy Surveys imaging of the DESI footprint is supported by the Director, Office of Science, Office

of High Energy Physics of the U.S. Department of Energy under Contract No. DE-AC02-05CH1123, by the National Energy Research Scientific Computing Center, a DOE Office of Science User Facility under the same contract; and by the U.S. National Science Foundation, Division of Astronomical Sciences under Contract No. AST-0950945 to NOAO.

Facilities: Gaia

Software: `astropy` (Astropy Collaboration et al. 2013, 2018), `matplotlib` (Hunter 2007), `NumPy` (Walt et al. 2011), `iPython` (Pérez & Granger 2007), `SciPy` (Virtanen et al. 2020) `corner.py` (Foreman-Mackey 2016), `emcee` (Foreman-Mackey et al. 2013), `Q3C` (Koposov & Bartunov 2006)

REFERENCES

- Abbott, T. M. C., Adamów, M., Agüena, M., et al. 2021, *ApJS*, 255, 20, doi: [10.3847/1538-4365/ac00b3](https://doi.org/10.3847/1538-4365/ac00b3)
- Astropy Collaboration, Robitaille, T. P., Tollerud, E. J., et al. 2013, *A&A*, 558, A33, doi: [10.1051/0004-6361/201322068](https://doi.org/10.1051/0004-6361/201322068)
- Astropy Collaboration, Price-Whelan, A. M., Sipőcz, B. M., et al. 2018, *AJ*, 156, 123, doi: [10.3847/1538-3881/aabc4f](https://doi.org/10.3847/1538-3881/aabc4f)
- Battaglia, G., Taibi, S., Thomas, G. F., & Fritz, T. K. 2022, *A&A*, 657, A54, doi: [10.1051/0004-6361/202141528](https://doi.org/10.1051/0004-6361/202141528)
- Baumgardt, H., Faller, J., Meinhold, N., McGovern-Greco, C., & Hilker, M. 2022, *MNRAS*, 510, 3531, doi: [10.1093/mnras/stab3629](https://doi.org/10.1093/mnras/stab3629)
- Bechtol, K., Drlica-Wagner, A., Balbinot, E., et al. 2015, *ApJ*, 807, 50, doi: [10.1088/0004-637X/807/1/50](https://doi.org/10.1088/0004-637X/807/1/50)
- Behroozi, P. S., Wechsler, R. H., & Wu, H.-Y. 2013a, *ApJ*, 762, 109, doi: [10.1088/0004-637X/762/2/109](https://doi.org/10.1088/0004-637X/762/2/109)
- Behroozi, P. S., Wechsler, R. H., Wu, H.-Y., et al. 2013b, *ApJ*, 763, 18, doi: [10.1088/0004-637X/763/1/18](https://doi.org/10.1088/0004-637X/763/1/18)
- Bellazzini, M., Ferraro, F. R., Origlia, L., et al. 2002, *AJ*, 124, 3222, doi: [10.1086/344794](https://doi.org/10.1086/344794)
- Bellazzini, M., Gennari, N., & Ferraro, F. R. 2005, *MNRAS*, 360, 185, doi: [10.1111/j.1365-2966.2005.09027.x](https://doi.org/10.1111/j.1365-2966.2005.09027.x)
- Belokurov, V., Zucker, D. B., Evans, N. W., et al. 2007, *ApJ*, 654, 897, doi: [10.1086/509718](https://doi.org/10.1086/509718)
- Belokurov, V., Walker, M. G., Evans, N. W., et al. 2009, *MNRAS*, 397, 1748, doi: [10.1111/j.1365-2966.2009.15106.x](https://doi.org/10.1111/j.1365-2966.2009.15106.x)
- Boettcher, E., Willman, B., Fadel, R., et al. 2013, *AJ*, 146, 94, doi: [10.1088/0004-6256/146/4/94](https://doi.org/10.1088/0004-6256/146/4/94)
- Bonanos, A. Z., Stanek, K. Z., Szentgyorgyi, A. H., Sasselov, D. D., & Bakos, G. Á. 2004, *AJ*, 127, 861, doi: [10.1086/381073](https://doi.org/10.1086/381073)
- Borukhovetskaya, A., Errani, R., Navarro, J. F., Fattahi, A., & Santos-Santos, I. 2022a, *MNRAS*, 509, 5330, doi: [10.1093/mnras/stab2912](https://doi.org/10.1093/mnras/stab2912)
- Borukhovetskaya, A., Navarro, J. F., Errani, R., & Fattahi, A. 2022b, *MNRAS*, 512, 5247, doi: [10.1093/mnras/stac653](https://doi.org/10.1093/mnras/stac653)
- Bovy, J. 2015, *ApJS*, 216, 29, doi: [10.1088/0067-0049/216/2/29](https://doi.org/10.1088/0067-0049/216/2/29)
- Bressan, A., Marigo, P., Girardi, L., et al. 2012, *MNRAS*, 427, 127, doi: [10.1111/j.1365-2966.2012.21948.x](https://doi.org/10.1111/j.1365-2966.2012.21948.x)
- Caldwell, N., Walker, M. G., Mateo, M., et al. 2017, *ApJ*, 839, 20, doi: [10.3847/1538-4357/aa688e](https://doi.org/10.3847/1538-4357/aa688e)
- Callingham, T. M., Cautun, M., Deason, A. J., et al. 2019, *MNRAS*, 484, 5453, doi: [10.1093/mnras/stz365](https://doi.org/10.1093/mnras/stz365)
- Cantu, S. A., Pace, A. B., Marshall, J., et al. 2021, *ApJ*, 916, 81, doi: [10.3847/1538-4357/ac0443](https://doi.org/10.3847/1538-4357/ac0443)
- Carlin, J. L., Grillmair, C. J., Muñoz, R. R., Nidever, D. L., & Majewski, S. R. 2009, *ApJ*, 702, L9, doi: [10.1088/0004-637X/702/1/L9](https://doi.org/10.1088/0004-637X/702/1/L9)
- Carlin, J. L., & Sand, D. J. 2018, *ApJ*, 865, 7, doi: [10.3847/1538-4357/aad8c1](https://doi.org/10.3847/1538-4357/aad8c1)
- Carlin, J. L., Sand, D. J., Muñoz, R. R., et al. 2017, *AJ*, 154, 267, doi: [10.3847/1538-3881/aa94d0](https://doi.org/10.3847/1538-3881/aa94d0)
- Casetti-Dinescu, D. I., & Girard, T. M. 2016, *MNRAS*, 461, 271, doi: [10.1093/mnras/stw1337](https://doi.org/10.1093/mnras/stw1337)
- Casetti-Dinescu, D. I., Girard, T. M., & Schrieffer, M. 2018, *MNRAS*, 473, 4064, doi: [10.1093/mnras/stx2645](https://doi.org/10.1093/mnras/stx2645)

Table 5. Dominant Error Source

Dwarf	$\sigma_{r_{\text{peri}}, \mu}$	$\sigma_{r_{\text{peri}}, d}$	$\sigma_{r_{\text{peri}}, \Phi}$	$\sigma_{r_{\text{apo}}, \mu}$	$\sigma_{r_{\text{apo}}, d}$	$\sigma_{r_{\text{apo}}, \Phi}$
Ant II	0.96	0.89	0.93	1.00	0.55	0.90
Aqu II	0.28	0.99	0.99	0.33	0.95	0.98
Boo I	0.98	0.52	0.94	1.00	0.52	0.85
Boo II	1.01	0.39	1.04	0.94	0.76	0.81
Boo III	0.98	0.37	0.97	1.00	0.81	0.62
CVn I	0.65	1.00	0.97	0.64	0.96	0.99
CVn II	0.30	0.97	1.01	0.30	0.89	0.88
Car	1.01	0.71	0.92	0.98	0.02	0.79
Car II	0.95	0.64	0.92	1.00	1.00	0.27
Car III	0.99	0.12	0.99	1.03	1.00	0.39
Col I	0.25	0.92	0.98	1.01	1.06	1.06
CB	0.99	0.11	0.99	0.94	0.75	0.71
Cra II	0.74	1.04	0.98	0.94	0.96	0.45
Dra	1.00	0.71	0.90	0.99	0.73	0.72
Dra II	0.91	0.83	0.79	0.92	0.94	0.39
Eri II	0.76	1.01	0.96	1.02	1.01	0.98
For	0.95	0.62	0.91	0.99	0.08	0.98
Gru I	0.41	1.00	0.99	0.57	0.92	0.74
Gru II	0.96	0.56	0.94	0.99	0.50	0.88
Her	0.62	0.93	0.99	0.82	0.98	0.88
Hor I	0.94	0.58	0.96	0.96	0.12	0.97
Hyd II	0.43	0.98	1.02	0.58	1.00	1.01
Hyi I	0.94	0.85	0.43	1.01	1.01	0.44
Leo I	0.89	1.01	0.96	0.96	0.98	0.64
Leo II	0.60	0.95	0.95	0.96	0.20	1.00
Leo IV	0.24	0.99	0.98	0.11	0.95	1.02
Leo V	0.18	1.06	1.08	1.05	0.99	1.02
Peg III	0.00	1.05	0.97	0.00	1.00	0.95
Phx II	0.98	1.10	0.78	1.01	0.82	0.78
Psc II	0.00	0.97	0.94	0.00	0.94	1.02
Ret II	0.98	0.36	0.91	1.01	0.59	0.73
Ret III	0.60	0.89	1.01	0.65	0.91	0.93
Sgr II	0.98	0.94	0.83	0.93	0.54	0.77
Scl	1.02	1.03	0.83	1.00	0.99	0.40
Seg 1	1.00	0.14	0.98	0.99	0.29	0.89
Seg 2	0.82	0.63	0.94	0.97	0.26	0.94
Sxt	0.98	0.66	0.87	0.98	0.95	0.53
Tri II	0.60	0.90	0.96	0.98	0.93	0.48
Tuc II	0.99	0.43	1.00	1.00	0.60	0.82
Tuc III	0.91	0.82	0.93	1.00	0.74	0.69
Tuc IV	0.98	0.43	0.97	0.98	0.25	0.96
Tuc V	0.75	0.68	0.99	0.83	0.47	0.99
UMa I	0.53	0.46	0.61	0.95	0.21	0.95
UMa II	0.98	0.32	0.96	1.03	0.52	0.83
UMi	1.02	0.89	0.84	1.01	0.82	0.66
Wil 1	0.64	0.75	0.96	1.00	0.03	0.98

- Cerny, W., Pace, A. B., Drlica-Wagner, A., et al. 2021, *ApJ*, 920, L44, doi: [10.3847/2041-8213/ac2d9a](https://doi.org/10.3847/2041-8213/ac2d9a)
- Cerny, W., Simon, J. D., Li, T. S., et al. 2022, arXiv e-prints, arXiv:2203.11788. <https://arxiv.org/abs/2203.11788>
- Chakrabarti, S., Chang, P., Price-Whelan, A. M., et al. 2019, *ApJ*, 886, 67, doi: [10.3847/1538-4357/ab4659](https://doi.org/10.3847/1538-4357/ab4659)
- Chambers, K. C., Magnier, E. A., Metcalfe, N., et al. 2016, ArXiv e-prints. <https://arxiv.org/abs/1612.05560>
- Chiti, A., Frebel, A., Jerjen, H., Kim, D., & Norris, J. E. 2020, *ApJ*, 891, 8, doi: [10.3847/1538-4357/ab6d72](https://doi.org/10.3847/1538-4357/ab6d72)
- Chiti, A., Frebel, A., Ji, A. P., et al. 2018, *ApJ*, 857, 74, doi: [10.3847/1538-4357/aab4fc](https://doi.org/10.3847/1538-4357/aab4fc)
- Chiti, A., Frebel, A., Simon, J. D., et al. 2021, *Nature Astronomy*, 5, 392, doi: [10.1038/s41550-020-01285-w](https://doi.org/10.1038/s41550-020-01285-w)
- Collins, M. L. M., Tollerud, E. J., Sand, D. J., et al. 2017, *MNRAS*, 467, 573, doi: [10.1093/mnras/stx067](https://doi.org/10.1093/mnras/stx067)
- Correa Magnus, L., & Vasiliev, E. 2022, *MNRAS*, 511, 2610, doi: [10.1093/mnras/stab3726](https://doi.org/10.1093/mnras/stab3726)
- Crnojević, D., Sand, D. J., Zaritsky, D., et al. 2016, *ApJ*, 824, L14, doi: [10.3847/2041-8205/824/1/L14](https://doi.org/10.3847/2041-8205/824/1/L14)
- Dall’Ora, M., Clementini, G., Kinemuchi, K., et al. 2006, *ApJ*, 653, L109, doi: [10.1086/510665](https://doi.org/10.1086/510665)
- Dall’Ora, M., Kinemuchi, K., Ripepi, V., et al. 2012, *ApJ*, 752, 42, doi: [10.1088/0004-637X/752/1/42](https://doi.org/10.1088/0004-637X/752/1/42)
- Deason, A. J., Wetzell, A. R., Garrison-Kimmel, S., & Belokurov, V. 2015, *MNRAS*, 453, 3568, doi: [10.1093/mnras/stv1939](https://doi.org/10.1093/mnras/stv1939)
- Deason, A. J., Erkal, D., Belokurov, V., et al. 2021, *MNRAS*, 501, 5964, doi: [10.1093/mnras/staa3984](https://doi.org/10.1093/mnras/staa3984)
- del Pino, A., Fardal, M. A., van der Marel, R. P., et al. 2021, *ApJ*, 908, 244, doi: [10.3847/1538-4357/abd5bf](https://doi.org/10.3847/1538-4357/abd5bf)
- DES Collaboration, Abbott, T. M. C., Abdalla, F. B., Allam, S., et al. 2018, *ApJS*, 239, 18, doi: [10.3847/1538-4365/aae9f0](https://doi.org/10.3847/1538-4365/aae9f0)
- Dey, A., Schlegel, D. J., Lang, D., et al. 2019, *AJ*, 157, 168, doi: [10.3847/1538-3881/ab089d](https://doi.org/10.3847/1538-3881/ab089d)
- Dinescu, D. I., Keeney, B. A., Majewski, S. R., & Girard, T. M. 2004, *AJ*, 128, 687, doi: [10.1086/422491](https://doi.org/10.1086/422491)
- Dotter, A., Chaboyer, B., Jevremović, D., et al. 2008, *ApJS*, 178, 89, doi: [10.1086/589654](https://doi.org/10.1086/589654)
- Drlica-Wagner, A., Bechtol, K., Rykoff, E. S., et al. 2015, *ApJ*, 813, 109, doi: [10.1088/0004-637X/813/2/109](https://doi.org/10.1088/0004-637X/813/2/109)
- Drlica-Wagner, A., Bechtol, K., Allam, S., et al. 2016, *ApJ*, 833, L5, doi: [10.3847/2041-8205/833/1/L5](https://doi.org/10.3847/2041-8205/833/1/L5)
- Drlica-Wagner, A., Bechtol, K., Mau, S., et al. 2020, *ApJ*, 893, 47, doi: [10.3847/1538-4357/ab7eb9](https://doi.org/10.3847/1538-4357/ab7eb9)
- Drlica-Wagner, A., Carlin, J. L., Nidever, D. L., et al. 2021, *ApJS*, 256, 2, doi: [10.3847/1538-4365/ac079d](https://doi.org/10.3847/1538-4365/ac079d)
- D’Souza, R., & Bell, E. F. 2022, *MNRAS*, 512, 739, doi: [10.1093/mnras/stac404](https://doi.org/10.1093/mnras/stac404)
- Erkal, D., & Belokurov, V. A. 2020, *MNRAS*, 495, 2554, doi: [10.1093/mnras/staa1238](https://doi.org/10.1093/mnras/staa1238)
- Erkal, D., Belokurov, V. A., & Parkin, D. L. 2020, *MNRAS*, 498, 5574, doi: [10.1093/mnras/staa2840](https://doi.org/10.1093/mnras/staa2840)
- Erkal, D., Belokurov, V., Laporte, C. F. P., et al. 2019, *MNRAS*, 487, 2685, doi: [10.1093/mnras/stz1371](https://doi.org/10.1093/mnras/stz1371)
- Erkal, D., Deason, A. J., Belokurov, V., et al. 2021, *MNRAS*, 506, 2677, doi: [10.1093/mnras/stab1828](https://doi.org/10.1093/mnras/stab1828)
- Filion, C., & Wyse, R. F. G. 2021, *ApJ*, 923, 218, doi: [10.3847/1538-4357/ac2df1](https://doi.org/10.3847/1538-4357/ac2df1)
- Fillingham, S. P., Cooper, M. C., Kelley, T., et al. 2019, arXiv e-prints, arXiv:1906.04180. <https://arxiv.org/abs/1906.04180>
- Flaugher, B., Diehl, H. T., Honscheid, K., et al. 2015, *AJ*, 150, 150, doi: [10.1088/0004-6256/150/5/150](https://doi.org/10.1088/0004-6256/150/5/150)
- Foreman-Mackey, D. 2016, *The Journal of Open Source Software*, 1, 24, doi: [10.21105/joss.00024](https://doi.org/10.21105/joss.00024)
- Foreman-Mackey, D., Hogg, D. W., Lang, D., & Goodman, J. 2013, *PASP*, 125, 306, doi: [10.1086/670067](https://doi.org/10.1086/670067)
- Fritz, T. K., Battaglia, G., Pawlowski, M. S., et al. 2018a, *A&A*, 619, A103, doi: [10.1051/0004-6361/201833343](https://doi.org/10.1051/0004-6361/201833343)
- Fritz, T. K., Carrera, R., Battaglia, G., & Taibi, S. 2019, *A&A*, 623, A129, doi: [10.1051/0004-6361/201833458](https://doi.org/10.1051/0004-6361/201833458)
- Fritz, T. K., Di Cintio, A., Battaglia, G., Brook, C., & Taibi, S. 2020, *MNRAS*, 494, 5178, doi: [10.1093/mnras/staa1040](https://doi.org/10.1093/mnras/staa1040)
- Fritz, T. K., Lokken, M., Kallivayalil, N., et al. 2018b, *ApJ*, 860, 164, doi: [10.3847/1538-4357/aac516](https://doi.org/10.3847/1538-4357/aac516)
- Fu, S. W., Simon, J. D., & Alarcón Jara, A. G. 2019, *ApJ*, 883, 11, doi: [10.3847/1538-4357/ab3658](https://doi.org/10.3847/1538-4357/ab3658)
- Gaia Collaboration, Helmi, A., van Leeuwen, F., et al. 2018, *A&A*, 616, A12, doi: [10.1051/0004-6361/201832698](https://doi.org/10.1051/0004-6361/201832698)
- Gaia Collaboration, Brown, A. G. A., Vallenari, A., et al. 2021a, *A&A*, 649, A1, doi: [10.1051/0004-6361/202039657](https://doi.org/10.1051/0004-6361/202039657)
- Gaia Collaboration, Luri, X., Chemin, L., et al. 2021b, *A&A*, 649, A7, doi: [10.1051/0004-6361/202039588](https://doi.org/10.1051/0004-6361/202039588)
- Garavito-Camargo, N., Patel, E., Besla, G., et al. 2021, arXiv e-prints, arXiv:2108.07321. <https://arxiv.org/abs/2108.07321>
- Garofalo, A., Delgado, H. E., Sarro, L. M., et al. 2022, arXiv e-prints, arXiv:2203.07435. <https://arxiv.org/abs/2203.07435>
- Garofalo, A., Cusano, F., Clementini, G., et al. 2013, *ApJ*, 767, 62, doi: [10.1088/0004-637X/767/1/62](https://doi.org/10.1088/0004-637X/767/1/62)
- Garrison-Kimmel, S., Wetzell, A., Bullock, J. S., et al. 2017, *MNRAS*, 471, 1709, doi: [10.1093/mnras/stx1710](https://doi.org/10.1093/mnras/stx1710)
- Gómez, F. A., Besla, G., Carpinero, D. D., et al. 2015, *ApJ*, 802, 128, doi: [10.1088/0004-637X/802/2/128](https://doi.org/10.1088/0004-637X/802/2/128)

- Greco, C., Dall’Ora, M., Clementini, G., et al. 2008, *ApJ*, 675, L73, doi: [10.1086/533585](https://doi.org/10.1086/533585)
- Gregory, A. L., Collins, M. L. M., Erkal, D., et al. 2020, *MNRAS*, 496, 1092, doi: [10.1093/mnras/staa1553](https://doi.org/10.1093/mnras/staa1553)
- Hansen, T. T., Simon, J. D., Marshall, J. L., et al. 2017, *ApJ*, 838, 44, doi: [10.3847/1538-4357/aa634a](https://doi.org/10.3847/1538-4357/aa634a)
- Homma, D., Chiba, M., Okamoto, S., et al. 2018, *PASJ*, 70, S18, doi: [10.1093/pasj/psx050](https://doi.org/10.1093/pasj/psx050)
- Homma, D., Chiba, M., Komiyama, Y., et al. 2019, *PASJ*, 71, 94, doi: [10.1093/pasj/psz076](https://doi.org/10.1093/pasj/psz076)
- Hunter, J. D. 2007, *Computing In Science & Engineering*, 9, 90
- Jenkins, S. A., Li, T. S., Pace, A. B., et al. 2021, *ApJ*, 920, 92, doi: [10.3847/1538-4357/ac1353](https://doi.org/10.3847/1538-4357/ac1353)
- Jethwa, P., Erkal, D., & Belokurov, V. 2016, *MNRAS*, 461, 2212, doi: [10.1093/mnras/stw1343](https://doi.org/10.1093/mnras/stw1343)
- . 2018, *MNRAS*, 473, 2060, doi: [10.1093/mnras/stx2330](https://doi.org/10.1093/mnras/stx2330)
- Ji, A. P., Frebel, A., Simon, J. D., & Geha, M. 2016, *ApJ*, 817, 41, doi: [10.3847/0004-637X/817/1/41](https://doi.org/10.3847/0004-637X/817/1/41)
- Ji, A. P., Li, T. S., Simon, J. D., et al. 2020, *ApJ*, 889, 27, doi: [10.3847/1538-4357/ab6213](https://doi.org/10.3847/1538-4357/ab6213)
- Ji, A. P., Koposov, S. E., Li, T. S., et al. 2021, *ApJ*, 921, 32, doi: [10.3847/1538-4357/ac1869](https://doi.org/10.3847/1538-4357/ac1869)
- Jiang, F., Kaplinghat, M., Lisanti, M., & Slone, O. 2021, *arXiv e-prints*, arXiv:2108.03243. <https://arxiv.org/abs/2108.03243>
- Kallivayalil, N., van der Marel, R. P., Besla, G., Anderson, J., & Alcock, C. 2013, *ApJ*, 764, 161, doi: [10.1088/0004-637X/764/2/161](https://doi.org/10.1088/0004-637X/764/2/161)
- Kallivayalil, N., Sales, L. V., Zivick, P., et al. 2018, *ApJ*, 867, 19, doi: [10.3847/1538-4357/aadfee](https://doi.org/10.3847/1538-4357/aadfee)
- Kaplinghat, M., Valli, M., & Yu, H.-B. 2019, *MNRAS*, 490, 231, doi: [10.1093/mnras/stz2511](https://doi.org/10.1093/mnras/stz2511)
- Karczarek, P., Pietrzyński, G., Gieren, W., et al. 2015, *AJ*, 150, 90, doi: [10.1088/0004-6256/150/3/90](https://doi.org/10.1088/0004-6256/150/3/90)
- Kim, D., & Jerjen, H. 2015, *ApJ*, 808, L39, doi: [10.1088/2041-8205/808/2/L39](https://doi.org/10.1088/2041-8205/808/2/L39)
- Kim, D., Jerjen, H., Geha, M., et al. 2016, *ApJ*, 833, 16, doi: [10.3847/0004-637X/833/1/16](https://doi.org/10.3847/0004-637X/833/1/16)
- King, I. 1962, *AJ*, 67, 471, doi: [10.1086/108756](https://doi.org/10.1086/108756)
- Kirby, E. N., Boylan-Kolchin, M., Cohen, J. G., et al. 2013, *ApJ*, 770, 16, doi: [10.1088/0004-637X/770/1/16](https://doi.org/10.1088/0004-637X/770/1/16)
- Kirby, E. N., Cohen, J. G., Simon, J. D., et al. 2017, *ApJ*, 838, 83, doi: [10.3847/1538-4357/aa6570](https://doi.org/10.3847/1538-4357/aa6570)
- Kirby, E. N., Simon, J. D., & Cohen, J. G. 2015, *ApJ*, 810, 56, doi: [10.1088/0004-637X/810/1/56](https://doi.org/10.1088/0004-637X/810/1/56)
- Kleyna, J. T., Wilkinson, M. I., Evans, N. W., & Gilmore, G. 2005, *ApJ*, 630, L141, doi: [10.1086/491654](https://doi.org/10.1086/491654)
- Koch, A., Wilkinson, M. I., Kleyna, J. T., et al. 2009, *ApJ*, 690, 453, doi: [10.1088/0004-637X/690/1/453](https://doi.org/10.1088/0004-637X/690/1/453)
- Koposov, S., & Bartunov, O. 2006, in *Astronomical Society of the Pacific Conference Series*, Vol. 351, *Astronomical Data Analysis Software and Systems XV*, ed. C. Gabriel, C. Arviset, D. Ponz, & S. Enrique, 735
- Koposov, S., Belokurov, V., Evans, N. W., et al. 2008, *ApJ*, 686, 279, doi: [10.1086/589911](https://doi.org/10.1086/589911)
- Koposov, S. E., Belokurov, V., Torrealba, G., & Evans, N. W. 2015a, *ApJ*, 805, 130, doi: [10.1088/0004-637X/805/2/130](https://doi.org/10.1088/0004-637X/805/2/130)
- Koposov, S. E., Gilmore, G., Walker, M. G., et al. 2011, *ApJ*, 736, 146, doi: [10.1088/0004-637X/736/2/146](https://doi.org/10.1088/0004-637X/736/2/146)
- Koposov, S. E., Casey, A. R., Belokurov, V., et al. 2015b, *ApJ*, 811, 62, doi: [10.1088/0004-637X/811/1/62](https://doi.org/10.1088/0004-637X/811/1/62)
- Koposov, S. E., Walker, M. G., Belokurov, V., et al. 2018, *MNRAS*, 479, 5343, doi: [10.1093/mnras/sty1772](https://doi.org/10.1093/mnras/sty1772)
- Koposov, S. E., Belokurov, V., Li, T. S., et al. 2019, *MNRAS*, 485, 4726, doi: [10.1093/mnras/stz457](https://doi.org/10.1093/mnras/stz457)
- Kuehn, C., Kinemuchi, K., Ripepi, V., et al. 2008, *ApJ*, 674, L81, doi: [10.1086/529137](https://doi.org/10.1086/529137)
- Küpper, A. H. W., Balbinot, E., Bonaca, A., et al. 2015, *ApJ*, 803, 80, doi: [10.1088/0004-637X/803/2/80](https://doi.org/10.1088/0004-637X/803/2/80)
- Küpper, A. H. W., Johnston, K. V., Mieske, S., Collins, M. L. M., & Tollerud, E. J. 2017, *ApJ*, 834, 112, doi: [10.3847/1538-4357/834/2/112](https://doi.org/10.3847/1538-4357/834/2/112)
- Lépine, S., Koch, A., Rich, R. M., & Kuijken, K. 2011, *ApJ*, 741, 100, doi: [10.1088/0004-637X/741/2/100](https://doi.org/10.1088/0004-637X/741/2/100)
- Li, H., Hammer, F., Babusiaux, C., et al. 2021, *ApJ*, 916, 8, doi: [10.3847/1538-4357/ac0436](https://doi.org/10.3847/1538-4357/ac0436)
- Li, T. S., Simon, J. D., Drlica-Wagner, A., et al. 2017, *ApJ*, 838, 8, doi: [10.3847/1538-4357/aa6113](https://doi.org/10.3847/1538-4357/aa6113)
- Li, T. S., Simon, J. D., Pace, A. B., et al. 2018a, *ApJ*, 857, 145, doi: [10.3847/1538-4357/aab666](https://doi.org/10.3847/1538-4357/aab666)
- Li, T. S., Simon, J. D., Kuehn, K., et al. 2018b, *ApJ*, 866, 22, doi: [10.3847/1538-4357/aadf91](https://doi.org/10.3847/1538-4357/aadf91)
- Li, T. S., Ji, A. P., Pace, A. B., et al. 2022, *ApJ*, 928, 30, doi: [10.3847/1538-4357/ac46d3](https://doi.org/10.3847/1538-4357/ac46d3)
- Li, Z.-Z., Qian, Y.-Z., Han, J., et al. 2020, *ApJ*, 894, 10, doi: [10.3847/1538-4357/ab84f0](https://doi.org/10.3847/1538-4357/ab84f0)
- Lindgren, L., Klioner, S. A., Hernández, J., et al. 2021, *A&A*, 649, A2, doi: [10.1051/0004-6361/202039709](https://doi.org/10.1051/0004-6361/202039709)
- Longeard, N., Martin, N., Starkenburg, E., et al. 2018, *MNRAS*, 480, 2609, doi: [10.1093/mnras/sty1986](https://doi.org/10.1093/mnras/sty1986)
- . 2020, *MNRAS*, 491, 356, doi: [10.1093/mnras/stz2854](https://doi.org/10.1093/mnras/stz2854)
- Longeard, N., Martin, N., Ibata, R. A., et al. 2021a, *MNRAS*, 503, 2754, doi: [10.1093/mnras/stab604](https://doi.org/10.1093/mnras/stab604)
- Longeard, N., Jablonka, P., Arentsen, A., et al. 2021b, *arXiv e-prints*, arXiv:2107.10849. <https://arxiv.org/abs/2107.10849>

- Martin, N. F., Ibata, R. A., Chapman, S. C., Irwin, M., & Lewis, G. F. 2007, *MNRAS*, 380, 281, doi: [10.1111/j.1365-2966.2007.12055.x](https://doi.org/10.1111/j.1365-2966.2007.12055.x)
- Martin, N. F., & Jin, S. 2010, *ApJ*, 721, 1333, doi: [10.1088/0004-637X/721/2/1333](https://doi.org/10.1088/0004-637X/721/2/1333)
- Martin, N. F., Nidever, D. L., Besla, G., et al. 2015, *ApJ*, 804, L5, doi: [10.1088/2041-8205/804/1/L5](https://doi.org/10.1088/2041-8205/804/1/L5)
- Martin, N. F., Geha, M., Ibata, R. A., et al. 2016a, *MNRAS*, 458, L59, doi: [10.1093/mnras/52w013](https://doi.org/10.1093/mnras/52w013)
- Martin, N. F., Ibata, R. A., Collins, M. L. M., et al. 2016b, *ApJ*, 818, 40, doi: [10.3847/0004-637X/818/1/40](https://doi.org/10.3847/0004-637X/818/1/40)
- Martínez, G. D., Minor, Q. E., Bullock, J., et al. 2011, *ApJ*, 738, 55, doi: [10.1088/0004-637X/738/1/55](https://doi.org/10.1088/0004-637X/738/1/55)
- Martínez-García, A. M., del Pino, A., Aparicio, A., van der Marel, R. P., & Watkins, L. L. 2021, *MNRAS*, 505, 5884, doi: [10.1093/mnras/stab1568](https://doi.org/10.1093/mnras/stab1568)
- Martínez-Vázquez, C. E., Monelli, M., Bono, G., et al. 2015, *MNRAS*, 454, 1509, doi: [10.1093/mnras/stv2014](https://doi.org/10.1093/mnras/stv2014)
- Martínez-Vázquez, C. E., Vivas, A. K., Gurevich, M., et al. 2019, *MNRAS*, 490, 2183, doi: [10.1093/mnras/stz2609](https://doi.org/10.1093/mnras/stz2609)
- Massari, D., Breddels, M. A., Helmi, A., et al. 2018, *Nature Astronomy*, 2, 156, doi: [10.1038/s41550-017-0322-y](https://doi.org/10.1038/s41550-017-0322-y)
- Massari, D., & Helmi, A. 2018, *A&A*, 620, A155, doi: [10.1051/0004-6361/201833367](https://doi.org/10.1051/0004-6361/201833367)
- Mateo, M., Olszewski, E. W., & Walker, M. G. 2008, *ApJ*, 675, 201, doi: [10.1086/522326](https://doi.org/10.1086/522326)
- Mau, S., Cerny, W., Pace, A. B., et al. 2020, *ApJ*, 890, 136, doi: [10.3847/1538-4357/ab6c67](https://doi.org/10.3847/1538-4357/ab6c67)
- McConnachie, A. W. 2012, *AJ*, 144, 4, doi: [10.1088/0004-6256/144/1/4](https://doi.org/10.1088/0004-6256/144/1/4)
- McConnachie, A. W., & Venn, K. A. 2020a, *AJ*, 160, 124, doi: [10.3847/1538-3881/aba4ab](https://doi.org/10.3847/1538-3881/aba4ab)
- . 2020b, *Research Notes of the American Astronomical Society*, 4, 229, doi: [10.3847/2515-5172/abd18b](https://doi.org/10.3847/2515-5172/abd18b)
- McMillan, P. J. 2017, *MNRAS*, 465, 76, doi: [10.1093/mnras/stw2759](https://doi.org/10.1093/mnras/stw2759)
- Medina, G. E., Muñoz, R. R., Vivas, A. K., et al. 2018, *ApJ*, 855, 43, doi: [10.3847/1538-4357/aaad02](https://doi.org/10.3847/1538-4357/aaad02)
- Méndez, R. A., Costa, E., Gallart, C., et al. 2011, *AJ*, 142, 93, doi: [10.1088/0004-6256/142/3/93](https://doi.org/10.1088/0004-6256/142/3/93)
- Minor, Q. E., Pace, A. B., Marshall, J. L., & Strigari, L. E. 2019, *MNRAS*, 487, 2961, doi: [10.1093/mnras/stz1468](https://doi.org/10.1093/mnras/stz1468)
- Moliné, Á., Sánchez-Conde, M. A., Aguirre-Santaella, A., et al. 2021, arXiv e-prints, arXiv:2110.02097, <https://arxiv.org/abs/2110.02097>
- Moskowitz, A. G., & Walker, M. G. 2020, *ApJ*, 892, 27, doi: [10.3847/1538-4357/ab7459](https://doi.org/10.3847/1538-4357/ab7459)
- Muñoz, R. R., Carlin, J. L., Frinchaboy, P. M., et al. 2006, *ApJ*, 650, L51, doi: [10.1086/508685](https://doi.org/10.1086/508685)
- Muñoz, R. R., Côté, P., Santana, F. A., et al. 2018, *ApJ*, 860, 66, doi: [10.3847/1538-4357/aac16b](https://doi.org/10.3847/1538-4357/aac16b)
- Muñoz, R. R., Geha, M., & Willman, B. 2010, *AJ*, 140, 138, doi: [10.1088/0004-6256/140/1/138](https://doi.org/10.1088/0004-6256/140/1/138)
- Muñoz, R. R., Majewski, S. R., & Johnston, K. V. 2008, *ApJ*, 679, 346, doi: [10.1086/587125](https://doi.org/10.1086/587125)
- Musella, I., Ripepi, V., Clementini, G., et al. 2009, *ApJ*, 695, L83, doi: [10.1088/0004-637X/695/1/L83](https://doi.org/10.1088/0004-637X/695/1/L83)
- Mutlu-Pakdil, B., Sand, D. J., Carlin, J. L., et al. 2018, *ApJ*, 863, 25, doi: [10.3847/1538-4357/aacd0e](https://doi.org/10.3847/1538-4357/aacd0e)
- Mutlu-Pakdil, B., Sand, D. J., Walker, M. G., et al. 2019, *ApJ*, 885, 53, doi: [10.3847/1538-4357/ab45ec](https://doi.org/10.3847/1538-4357/ab45ec)
- Mutlu-Pakdil, B., Sand, D. J., Crnojević, D., et al. 2020, *ApJ*, 902, 106, doi: [10.3847/1538-4357/abb40b](https://doi.org/10.3847/1538-4357/abb40b)
- Nagarajan, P., Weisz, D. R., & El-Badry, K. 2021, arXiv e-prints, arXiv:2111.06899, <https://arxiv.org/abs/2111.06899>
- Nagasawa, D. Q., Marshall, J. L., Li, T. S., et al. 2018, *ApJ*, 852, 99, doi: [10.3847/1538-4357/aaa01d](https://doi.org/10.3847/1538-4357/aaa01d)
- Navarro, J. F., Frenk, C. S., & White, S. D. M. 1996, *ApJ*, 462, 563, doi: [10.1086/177173](https://doi.org/10.1086/177173)
- Nidever, D. L., Olsen, K., Choi, Y., et al. 2021a, *AJ*, 161, 74, doi: [10.3847/1538-3881/abceb7](https://doi.org/10.3847/1538-3881/abceb7)
- Nidever, D. L., Dey, A., Fasbender, K., et al. 2021b, *AJ*, 161, 192, doi: [10.3847/1538-3881/abd6e1](https://doi.org/10.3847/1538-3881/abd6e1)
- Norris, J. E., Wyse, R. F. G., Gilmore, G., et al. 2010, *ApJ*, 723, 1632, doi: [10.1088/0004-637X/723/2/1632](https://doi.org/10.1088/0004-637X/723/2/1632)
- Okamoto, S., Arimoto, N., Tolstoy, E., et al. 2017, *MNRAS*, 467, 208, doi: [10.1093/mnras/stx086](https://doi.org/10.1093/mnras/stx086)
- Pace, A. B., & Li, T. S. 2019, *ApJ*, 875, 77, doi: [10.3847/1538-4357/ab0aee](https://doi.org/10.3847/1538-4357/ab0aee)
- Pace, A. B., & Strigari, L. E. 2019, *MNRAS*, 482, 3480, doi: [10.1093/mnras/sty2839](https://doi.org/10.1093/mnras/sty2839)
- Pace, A. B., Kaplinghat, M., Kirby, E., et al. 2020, *MNRAS*, 495, 3022, doi: [10.1093/mnras/staa1419](https://doi.org/10.1093/mnras/staa1419)
- Pardy, S. A., D’Onghia, E., Navarro, J. F., et al. 2020, *MNRAS*, 492, 1543, doi: [10.1093/mnras/stz3192](https://doi.org/10.1093/mnras/stz3192)
- Patel, E., Kallivayalil, N., Garavito-Camargo, N., et al. 2020, *ApJ*, 893, 121, doi: [10.3847/1538-4357/ab7b75](https://doi.org/10.3847/1538-4357/ab7b75)
- Pawlowski, M. S., Oria, P.-A., Taibi, S., Famaey, B., & Ibata, R. 2021, arXiv e-prints, arXiv:2111.05358, <https://arxiv.org/abs/2111.05358>
- Pereira, M. J., Bryan, G. L., & Gill, S. P. D. 2008, *ApJ*, 672, 825, doi: [10.1086/523830](https://doi.org/10.1086/523830)
- Pérez, F., & Granger, B. E. 2007, *Computing in Science and Engineering*, 9, 21, doi: [10.1109/MCSE.2007.53](https://doi.org/10.1109/MCSE.2007.53)
- Petersen, M. S., & Peñarrubia, J. 2021, *Nature Astronomy*, 5, 251, doi: [10.1038/s41550-020-01254-3](https://doi.org/10.1038/s41550-020-01254-3)
- Piatek, S., Pryor, C., Bristow, P., et al. 2005, *AJ*, 130, 95, doi: [10.1086/430532](https://doi.org/10.1086/430532)

- . 2006, *AJ*, 131, 1445, doi: [10.1086/499526](https://doi.org/10.1086/499526)
- . 2007, *AJ*, 133, 818, doi: [10.1086/510456](https://doi.org/10.1086/510456)
- Piatek, S., Pryor, C., & Olszewski, E. W. 2016, *AJ*, 152, 166, doi: [10.3847/0004-6256/152/6/166](https://doi.org/10.3847/0004-6256/152/6/166)
- Piatek, S., Pryor, C., Olszewski, E. W., et al. 2003, *AJ*, 126, 2346, doi: [10.1086/378713](https://doi.org/10.1086/378713)
- . 2002, *AJ*, 124, 3198, doi: [10.1086/344767](https://doi.org/10.1086/344767)
- Pietrzyński, G., Górski, M., Gieren, W., et al. 2009, *AJ*, 138, 459, doi: [10.1088/0004-6256/138/2/459](https://doi.org/10.1088/0004-6256/138/2/459)
- Pietrzyński, G., Graczyk, D., Gallenne, A., et al. 2019, *Nature*, 567, 200, doi: [10.1038/s41586-019-0999-4](https://doi.org/10.1038/s41586-019-0999-4)
- Plummer, H. C. 1911, *MNRAS*, 71, 460
- Pryor, C., Piatek, S., & Olszewski, E. W. 2015, *AJ*, 149, 42, doi: [10.1088/0004-6256/149/2/42](https://doi.org/10.1088/0004-6256/149/2/42)
- Qi, Y., Zivick, P., Pace, A. B., Riley, A. H., & Strigari, L. E. 2022, *MNRAS*, 512, 5601, doi: [10.1093/mnras/stac805](https://doi.org/10.1093/mnras/stac805)
- Richstein, H., Patel, E., Kallivayalil, N., et al. 2022, arXiv e-prints, arXiv:2204.01917, <https://arxiv.org/abs/2204.01917>
- Riello, M., De Angeli, F., Evans, D. W., et al. 2021, *A&A*, 649, A3, doi: [10.1051/0004-6361/202039587](https://doi.org/10.1051/0004-6361/202039587)
- Riley, A. H., Fattahi, A., Pace, A. B., et al. 2019, *MNRAS*, 486, 2679, doi: [10.1093/mnras/stz973](https://doi.org/10.1093/mnras/stz973)
- Robles, V. H., & Bullock, J. S. 2021, *MNRAS*, 503, 5232, doi: [10.1093/mnras/stab829](https://doi.org/10.1093/mnras/stab829)
- Roderick, T. A., Jerjen, H., Mackey, A. D., & Da Costa, G. S. 2015, *ApJ*, 804, 134, doi: [10.1088/0004-637X/804/2/134](https://doi.org/10.1088/0004-637X/804/2/134)
- Sales, L. V., Navarro, J. F., Kallivayalil, N., & Frenk, C. S. 2017, *MNRAS*, 465, 1879, doi: [10.1093/mnras/stw2816](https://doi.org/10.1093/mnras/stw2816)
- Sand, D. J., Olszewski, E. W., Willman, B., et al. 2009, *ApJ*, 704, 898, doi: [10.1088/0004-637X/704/2/898](https://doi.org/10.1088/0004-637X/704/2/898)
- Sand, D. J., Strader, J., Willman, B., et al. 2012, *ApJ*, 756, 79, doi: [10.1088/0004-637X/756/1/79](https://doi.org/10.1088/0004-637X/756/1/79)
- Sanders, J. L., & Evans, N. W. 2017, *MNRAS*, 472, 2670, doi: [10.1093/mnras/stx2116](https://doi.org/10.1093/mnras/stx2116)
- Sanders, J. L., Evans, N. W., & Dehnen, W. 2018, *MNRAS*, 478, 3879, doi: [10.1093/mnras/sty1278](https://doi.org/10.1093/mnras/sty1278)
- Santos-Santos, I. M. E., Fattahi, A., Sales, L. V., & Navarro, J. F. 2021, *MNRAS*, 504, 4551, doi: [10.1093/mnras/stab1020](https://doi.org/10.1093/mnras/stab1020)
- Schönrich, R., Binney, J., & Dehnen, W. 2010, *MNRAS*, 403, 1829, doi: [10.1111/j.1365-2966.2010.16253.x](https://doi.org/10.1111/j.1365-2966.2010.16253.x)
- Shipp, N., Drlica-Wagner, A., Balbinot, E., et al. 2018, *ApJ*, 862, 114, doi: [10.3847/1538-4357/aacdab](https://doi.org/10.3847/1538-4357/aacdab)
- Shipp, N., Li, T. S., Pace, A. B., et al. 2019, *ApJ*, 885, 3, doi: [10.3847/1538-4357/ab44bf](https://doi.org/10.3847/1538-4357/ab44bf)
- Simon, J. D. 2018, *ApJ*, 863, 89, doi: [10.3847/1538-4357/aacdfb](https://doi.org/10.3847/1538-4357/aacdfb)
- . 2019, *ARA&A*, 57, 375, doi: [10.1146/annurev-astro-091918-104453](https://doi.org/10.1146/annurev-astro-091918-104453)
- Simon, J. D., & Geha, M. 2007, *ApJ*, 670, 313, doi: [10.1086/521816](https://doi.org/10.1086/521816)
- Simon, J. D., Geha, M., Minor, Q. E., et al. 2011, *ApJ*, 733, 46, doi: [10.1088/0004-637X/733/1/46](https://doi.org/10.1088/0004-637X/733/1/46)
- Simon, J. D., Drlica-Wagner, A., Li, T. S., et al. 2015, *ApJ*, 808, 95, doi: [10.1088/0004-637X/808/1/95](https://doi.org/10.1088/0004-637X/808/1/95)
- Simon, J. D., Li, T. S., Drlica-Wagner, A., et al. 2017, *ApJ*, 838, 11, doi: [10.3847/1538-4357/aa5be7](https://doi.org/10.3847/1538-4357/aa5be7)
- Simon, J. D., Li, T. S., Erkal, D., et al. 2020, *ApJ*, 892, 137, doi: [10.3847/1538-4357/ab7ccb](https://doi.org/10.3847/1538-4357/ab7ccb)
- Simon, J. D., Brown, T. M., Drlica-Wagner, A., et al. 2021, *ApJ*, 908, 18, doi: [10.3847/1538-4357/abd31b](https://doi.org/10.3847/1538-4357/abd31b)
- Sohn, S. T., Besla, G., van der Marel, R. P., et al. 2013, *ApJ*, 768, 139, doi: [10.1088/0004-637X/768/2/139](https://doi.org/10.1088/0004-637X/768/2/139)
- Sohn, S. T., Patel, E., Besla, G., et al. 2017, *ApJ*, 849, 93, doi: [10.3847/1538-4357/aa917b](https://doi.org/10.3847/1538-4357/aa917b)
- Spencer, M. E., Mateo, M., Olszewski, E. W., et al. 2018, *AJ*, 156, 257, doi: [10.3847/1538-3881/aae3e4](https://doi.org/10.3847/1538-3881/aae3e4)
- Spencer, M. E., Mateo, M., Walker, M. G., & Olszewski, E. W. 2017, *ApJ*, 836, 202, doi: [10.3847/1538-4357/836/2/202](https://doi.org/10.3847/1538-4357/836/2/202)
- Springel, V. 2005, *MNRAS*, 364, 1105, doi: [10.1111/j.1365-2966.2005.09655.x](https://doi.org/10.1111/j.1365-2966.2005.09655.x)
- Stetson, P. B., Fiorentino, G., Bono, G., et al. 2014, *PASP*, 126, 616, doi: [10.1086/677352](https://doi.org/10.1086/677352)
- Torrealba, G., Koposov, S. E., Belokurov, V., & Irwin, M. 2016a, *MNRAS*, 459, 2370, doi: [10.1093/mnras/stw733](https://doi.org/10.1093/mnras/stw733)
- Torrealba, G., Koposov, S. E., Belokurov, V., et al. 2016b, *MNRAS*, 463, 712, doi: [10.1093/mnras/stw2051](https://doi.org/10.1093/mnras/stw2051)
- Torrealba, G., Belokurov, V., Koposov, S. E., et al. 2018, *MNRAS*, 475, 5085, doi: [10.1093/mnras/sty170](https://doi.org/10.1093/mnras/sty170)
- . 2019, *MNRAS*, 488, 2743, doi: [10.1093/mnras/stz1624](https://doi.org/10.1093/mnras/stz1624)
- van der Marel, R. P., Alves, D. R., Hardy, E., & Suntzeff, N. B. 2002, *AJ*, 124, 2639, doi: [10.1086/343775](https://doi.org/10.1086/343775)
- van der Marel, R. P., & Kallivayalil, N. 2014, *ApJ*, 781, 121, doi: [10.1088/0004-637X/781/2/121](https://doi.org/10.1088/0004-637X/781/2/121)
- Vasiliev, E., & Baumgardt, H. 2021, *MNRAS*, 505, 5978, doi: [10.1093/mnras/stab1475](https://doi.org/10.1093/mnras/stab1475)
- Vasiliev, E., & Belokurov, V. 2020, *MNRAS*, 497, 4162, doi: [10.1093/mnras/staa2114](https://doi.org/10.1093/mnras/staa2114)
- Vasiliev, E., Belokurov, V., & Erkal, D. 2021, *MNRAS*, 501, 2279, doi: [10.1093/mnras/staa3673](https://doi.org/10.1093/mnras/staa3673)
- Virtanen, P., Gommers, R., Oliphant, T. E., et al. 2020, *Nature Methods*, 17, 261, doi: [10.1038/s41592-019-0686-2](https://doi.org/10.1038/s41592-019-0686-2)
- Vitral, E. 2021, *MNRAS*, 504, 1355, doi: [10.1093/mnras/stab947](https://doi.org/10.1093/mnras/stab947)
- Vivas, A. K., Martínez-Vázquez, C. E., Walker, A. R., et al. 2022, *ApJ*, 926, 78, doi: [10.3847/1538-4357/ac43bd](https://doi.org/10.3847/1538-4357/ac43bd)

- Vivas, A. K., Olsen, K., Blum, R., et al. 2016, *AJ*, 151, 118, doi: [10.3847/0004-6256/151/5/118](https://doi.org/10.3847/0004-6256/151/5/118)
- Walker, A. R., Martínez-Vázquez, C. E., Monelli, M., et al. 2019, *MNRAS*, 490, 4121, doi: [10.1093/mnras/stz2826](https://doi.org/10.1093/mnras/stz2826)
- Walker, M. G., Mateo, M., & Olszewski, E. W. 2008, *ApJ*, 688, L75, doi: [10.1086/595586](https://doi.org/10.1086/595586)
- . 2009, *AJ*, 137, 3100, doi: [10.1088/0004-6256/137/2/3100](https://doi.org/10.1088/0004-6256/137/2/3100)
- Walker, M. G., Mateo, M., Olszewski, E. W., et al. 2015a, *ApJ*, 808, 108, doi: [10.1088/0004-637X/808/2/108](https://doi.org/10.1088/0004-637X/808/2/108)
- Walker, M. G., Olszewski, E. W., & Mateo, M. 2015b, *MNRAS*, 448, 2717, doi: [10.1093/mnras/stv099](https://doi.org/10.1093/mnras/stv099)
- Walker, M. G., Mateo, M., Olszewski, E. W., et al. 2016, *ApJ*, 819, 53, doi: [10.3847/0004-637X/819/1/53](https://doi.org/10.3847/0004-637X/819/1/53)
- Walsh, S. M., Willman, B., Sand, D., et al. 2008, *ApJ*, 688, 245, doi: [10.1086/592076](https://doi.org/10.1086/592076)
- Walt, S. v. d., Colbert, S. C., & Varoquaux, G. 2011, *Computing in Science & Engineering*, 13, 22, doi: <http://dx.doi.org/10.1109/MCSE.2011.37>
- Wang, M. Y., de Boer, T., Pieres, A., et al. 2019, *ApJ*, 881, 118, doi: [10.3847/1538-4357/ab31a9](https://doi.org/10.3847/1538-4357/ab31a9)
- Wang, W., Han, J., Cautun, M., Li, Z., & Ishigaki, M. N. 2020, *Science China Physics, Mechanics, and Astronomy*, 63, 109801, doi: [10.1007/s11433-019-1541-6](https://doi.org/10.1007/s11433-019-1541-6)
- Wenger, M., Ochsenbein, F., Egret, D., et al. 2000, *A&AS*, 143, 9, doi: [10.1051/aas:2000332](https://doi.org/10.1051/aas:2000332)
- Willman, B., Geha, M., Strader, J., et al. 2011, *AJ*, 142, 128, doi: [10.1088/0004-6256/142/4/128](https://doi.org/10.1088/0004-6256/142/4/128)
- Willman, B., Masjedi, M., Hogg, D. W., et al. 2006, arXiv e-prints, astro. <https://arxiv.org/abs/astro-ph/0603486>
- Wolf, J., Martinez, G. D., Bullock, J. S., et al. 2010, *MNRAS*, 406, 1220, doi: [10.1111/j.1365-2966.2010.16753.x](https://doi.org/10.1111/j.1365-2966.2010.16753.x)
- Zoutendijk, S. L., Brinchmann, J., Bouché, N. F., et al. 2021, *A&A*, 651, A80, doi: [10.1051/0004-6361/202040239](https://doi.org/10.1051/0004-6361/202040239)
- Zucker, D. B., Belokurov, V., Evans, N. W., et al. 2006, *ApJ*, 643, L103, doi: [10.1086/505216](https://doi.org/10.1086/505216)

APPENDIX

A. MEMBERSHIP CATALOGS

We provide catalogs of our membership along with select *Gaia* EDR3 columns on Zenodo under a Creative Commons Attribution license: [10.5281/zenodo.6533295](https://zenodo.org/record/6533295). We further include a diagnostic plot (similar to Figure 2) and a plot comparing our systemic proper motion measurement to literature values for each dSph and a machine readable compilation of Tables 1-5.

B. COMMENTS ON INDIVIDUAL DWARF SPHEROIDAL GALAXIES AND SPECIAL CASES

Ant II—Due to the low surface density of Ant II and the higher MW foreground due to the lower galactic latitude we only analyze the “clean” sample and use a magnitude limit, $G_{\max} = 20$, that is much higher than suggested from the depth of astrometric solutions in the Ant II region ($G_{\max} = 20.85$). Accurate photometry will assist with improving foreground separation in future measurements. Regardless our EDR3 measurement is consistent with other measurements (McConnachie & Venn 2020b; Battaglia et al. 2022) and spectroscopic based measurements (Ji et al. 2021). This dSph is included in our clear tidally disrupting sample based on the small pericenter and velocity gradient (Torrealba et al. 2019; Ji et al. 2021). While this analysis was in preparation a new analysis measuring the distance to Ant II with RRL stars which slightly improved and updated the distance measurement (Vivas et al. 2022).

Boo I—This dSph is included in our potentially tidally disrupting sample due to literature analysis (Longeard et al. 2021b; Filion & Wyse 2021) and a low value of $\rho_{1/2}/\rho_{MW}(r = r_{\text{peri}}) \sim 25$. We exclude the region around Boo II ($R_{\text{Boo II}} = 5 \times r_h$, $B_{\text{Boo II}} \sim 15'$) when constructing the fixed background model.

Boo II—We exclude a region around Boo I ($R_{\text{Boo I}} = 60' \sim 6 \times r_h$, $B_{\text{Boo I}}$) when constructing the fixed background model.

Boo III—This dSph is included in our potentially tidally disrupting based on its small pericenter and low average density (Carlin & Sand 2018). We do not include it in our clear tidally disrupting sample because of the lack of detailed tidal stripping models or clear observational evidence (e.g., deep photometry or kinematic evidence). There are a large number of candidate targets ($N_{\text{expected}} \sim 130$) that will significantly increase the spectroscopic sample size and can be used to further assess dynamical equilibrium. However, the large angular size and low luminosity makes follow-up difficult. We exclude the region around the globular clusters, NGC 5466 ($R_{\text{NGC 5466}} = 7 \times r_h$, $NGC 5466 = 16.1'$) and NGC 5272 ($R_{\text{NGC 5272}} = 30' \sim 13 \times r_h$, $NGC 5272$), when constructing the fixed background model.

Boo IV—A systemic proper motion measurement of this recently discovered dwarf has only been possible with EDR3. Our measurement disagrees with McConnachie & Venn (2020b) due to their choice of prior on the tangential velocity.

Car—While other works have considered Car as a potential LMC satellite (Pardy et al. 2020), we do not favor this scenario as it was closer to the MW at its most recent LMC pericenter. There is larger background contamination around Car than other bright satellites, due to its low relative Galactic latitude and the LMC foreground stars.

Car II and Car III—Because of the small angular separation between Car II and Car III we model these two dwarfs simultaneously. In particular, the angular separation, $\sim 18'$, is roughly $2 \times r_h$, $Car II$ and spatial overlap of members of the two dSphs is possible. There is DECam g, r coverage in the NSC catalog, however, we find there is a large color difference ($(g - r)_0 \sim 0.075$) between spectroscopic members (Li et al. 2018a) and a old-metal-poor isochrone. In addition, a direct comparison to the reported magnitudes in the Li et al. (2018a) catalog to the NSC catalog finds a similar offset. This suggests that there are potential calibration issues in this region. When we apply our standard g, r isochrone filter and include a color offset, we find that some Car II and Car III spectroscopic members are not included. Due to this issue, we opt to use *Gaia* photometry in this region.

We include a second dSph term in the likelihood to represent the Car III population and we modify the prior volume on $\mu_{\alpha\star}$ and μ_{δ} due to the large MW and LMC background. With the addition of the Car III component we are able to determine the systemic proper motion of both UFDs simultaneously for the fixed MW proper motion model. When we model the MW proper motion with a Gaussian model, the Car III component also models the MW foreground. In particular, the number of Car III ‘members’ is much larger than expected, the proper motion completely disagrees with known spectroscopic members, and the r_h spatial parameter takes on the largest possible value in the prior distribution to mimic a flat spatial distribution. This attests to the complexity of the MW and LMC background model in this region. Due to this issue, we only include the fixed background model results. Both Car II and Car III are highly likely

to associated with the LMC in our analysis and agrees with previous work (e.g., Erkal & Belokurov 2020; Battaglia et al. 2022).

Cet II—There was not a signal observed in *Gaia* DR2 (Pace & Li 2019; McConnachie & Venn 2020a) but there is a clear signal observed in *Gaia* EDR3.

Cet III—We exclude a region around the globular cluster Whiting 1 ($R_{\text{Whi 1}} = 5 \times r_h$, $Whi 1 = 1.1'$) when constructing the fixed background model.

Cra II—While there is not clear photometric (tidal tails) or kinematic evidence (e.g., gradients) (Ji et al. 2021) the small pericenter, large size, and small velocity dispersion suggests that Cra II is undergoing tidal disruption (Sanders et al. 2018; Borukhovetskaya et al. 2022b) and we classify it as potentially tidally disrupting.

Dra II—One of the few objects in the sample that may be faint star cluster and not a dwarf galaxy. Baumgardt et al. (2022) concluded that Dra II is a star cluster based on evidence of mass segregation. There is not a resolved velocity dispersion or metallicity dispersion that would indicate there is a dark matter halo (Longeard et al. 2018). There are potential of tidal features in smoothed stellar density distribution (Longeard et al. 2018). Due to the unresolved velocity dispersion and small size the density upper limit is quite large. Dra II has a relatively small pericenter and if the velocity dispersion was low ($\sim 1 \text{ km s}^{-1}$) the satellite would likely be undergoing tidal disruption.

Eri II—The photometric selection window was increased for Eri II due to its larger stellar mass relative to the other UFDs. Without this increase some spectroscopic members would be excluded. In addition, there is one spectroscopic member that is missing DECam photometry due to a nearby bright star that is manually included in the model. Only $\sim 15\%$ of the orbital samples are bound which have $r_{\text{peri}} \sim 100 \text{ kpc}$ ($r_{\text{peri, nL}} \sim 200 \text{ kpc}$) while the reminder of the chain is unbound.

For—The proper motion is anti-parallel to the solar motion and the orbit is more sensitive to the distance uncertainty than other dwarfs (Borukhovetskaya et al. 2022a). The orbital pole aligns with the LMC and this has been used as an argument for For to be associated with the LMC (Pardy et al. 2020). We do not find a potential association with the LMC and note that For was outside the LMC escape velocity at its most recent closest approach.

Gru II—There is a bright star ($G \sim 1.7$) near Gru II. In DES DR2, a large portion of the region around this star is masked. We opted to instead use DES DR1 (DES Collaboration et al. 2018) as the mask is smaller. It is possible that sources near the bright star have biased photometry/colors due to presence of the bright star.

Gru II spatially overlaps with the Chenab/Orphan stream and it has been suggested to be connected to the stream (Koposov et al. 2019). Gru II and the Chenab/Orphan stream are found to have the same proper motion (Shipp et al. 2019) but the radial velocities of Gru II is $\sim 90 \text{ km s}^{-1}$ offset from the Chenab/Orphan stream predictions (Simon et al. 2020) and Gru II is $\sim 10 \text{ kpc}$ more distant than the stream (Martínez-Vázquez et al. 2019). There will be overlap between the two structures in the color-magnitude diagram and both the signal and background region of Gru II will be contaminated with the Chenab/Orphan stream members that have similar a proper motion to the Gru II proper motion. Regardless we are able to successfully identify all known spectroscopic members. The candidate members from our mixture model likely include some Chenab/Orphan stream members and the spectroscopic success rate might be lower than expected.

This is one of the six dSphs that we have classified as likely tidally disrupted based on its low average density relative to the MW at pericenter ($\rho_{1/2}/\rho_{\text{MW}}(r = r_{\text{peri}}) \lesssim 10$). This agrees with Simon et al. (2020), which found that the tidal radius was just larger than the Gru II's physical size. As there is overlap in spatial and proper motion position but not radial velocity, searching for potential tidal tails and other signs of tidal disruption will be challenging.

We do not find an association with the LMC but note that it is one of the closest MW satellites in phase space. Other studies have considered Gru II recently captured by the LMC (e.g., Battaglia et al. 2022). We consider Gru II as potentially tidally disrupting based on its low value of $\rho_{1/2}/\rho_{\text{MW}}(r = r_{\text{peri}})$.

Her—The large elongation of Her has long been used as evidence for tidal disruption in her (e.g., Martin & Jin 2010; Küpper et al. 2017; Fu et al. 2019). Extra-tidal photometric overdensities have been identified (Sand et al. 2009; Roderick et al. 2015), however, follow-up efforts have been unsuccessful (Fu et al. 2019; Mutlu-Pakdil et al. 2020). The large pericenter, $r_{\text{peri}} \sim 60 \text{ kpc}$ we find with the LMC+MW orbit modeling suggests that the tidal shocking at pericenter is small however, we note that the orbital motion (via the reflex corrected proper motion) is aligned with the Her major axis ($|\theta_{\mu} - \theta_{\text{xy}}| \sim 5^\circ$)

Hor I—Likely LMC satellite. We exclude the region around the globular cluster NGC 1261 ($R_{\text{NGC 1261}} = 5 \times r_h$, $\text{NGC 1261} \sim 3.4'$) when constructing the fixed background model.

Hor II—Due to the low number of members and the lack of *Gaia* matches more observations are needed. Of the 3 spectroscopic members (Fritz et al. 2019) with astrometric solutions in DR2 only 2 have astrometric solutions in EDR3. We note that the same four member stars were identified in Pace & Li (2019) and in EDR3 the strength of the signal has increased.

Hyd II—The orbital pole of Hyd II aligns with the LMC (Kallivayalil et al. 2018) but we do not find a large probability ($p_{\text{LMC}} \sim 6\%$) for them to be associated. At the most recent minimum LMC distance ($r_{\text{LMC, min}} \sim 125$ kpc) Hyd II has a large relative velocity and is outside the LMC escape velocity ($(v_{\text{LMC, min}} \sim 250 \text{ km s}^{-1})$) and unlikely to be associated.

Hyi I—For the photometry of Hyi I we use the NSC catalog. Similar to Car II and Car III we find that there is a color offset between spectroscopic members and stellar isochrones. The offset is smaller than in Car II, $(g - r)_0 \sim 0.05$, and we find that after applying this offset to the photometry our standard isochrone selection is able to select all known spectroscopic members. Hyi I is a likely LMC satellite.

Leo V—In the clean sample, our selection remove all MW foreground members and only known Leo V spectroscopic members are left. This is not the case for the complete sample. This is the only dSph for which we do not find new candidate members in.

Peg III—All known spectroscopic members (Kim et al. 2016) are below the *Gaia* magnitude limit. While this analysis was in the later stages of preparation, there was a new analysis of the structural parameters and stellar distribution of Peg III with deep *HST* photometry (Richstein et al. 2022). In particular, they found the center of Peg II shifted by $\sim 0.5'$ and the half-light radius roughly doubled. With these updated structural parameters we are able to make a detection of the systemic proper motion of Peg III. In our previous analysis with the Kim et al. (2016) structural parameters, there were 4 candidate members with $p > 0.1$ but all had large errors such that $\sum p = 3.0^{+0.9}_{-3.0}$. With the updated parameters the same stars are identified as members with $\sum p = 3.9^{+0.3}_{-0.4}$. The candidate members are located $R \sim 1 - 2 r_h$ whereas with the previous literature values they were $R \sim 2 - 4 r_h$. There is no detection of Peg III in Battaglia et al. (2022) and the small errors in McConnachie & Venn (2020b) are likely due to their prior that the satellite be bound to the MW. Our measurement is just past the threshold for detection based on the small number of members. This highlights the next for accurate structural parameters to identify candidates dSph members without spectroscopic information.

Phx II—Likely LMC satellite.

Pic II—Similar to the other two NSC dSphs, we find a color offset for Pic II. This has the largest offset of the three NSC dSphs, $(g - r)_0 \sim 0.1$. We have modeled this object with both *Gaia* and NSC photometry and found that there is little difference between them. We opt to use the NSC photometry as we are able to exclude more background stars. When the structural parameters are varied, the half-light radius and ellipticity are found to be larger and more elongated than the literature values and the overall signal is weak at best. The overall UFD membership from the our standard analysis is $\sum p \sim 8 \pm 8$ and all identified stars contain large errors. To determine a more confident Pic II signal, we fixed the spatial parameters to the best fit literature values. When the structural parameters are fixed we find $\sum p \sim 6.1^{+3.5}_{-1.5}$ and the systemic proper motion has asymmetric error bars. We suspect this issues are caused by the large LMC+MW background and the overlap between the Pic II and LMC proper motion. Other EDR3 work have not had this issue (McConnachie & Venn 2020b; Battaglia et al. 2022) and a color-magnitude term in the likelihood may address this issue. Future spectroscopic observations and membership will assist in measuring the systemic proper motion.

Psc II—Our mixture models did not return a confident signal in Psc II, however, there are known spectroscopic members identified in the *Gaia* catalog (Fritz et al. 2018a). Two of the known spectroscopic stars were identified as members but they were assigned enormous errors ($\sim 0.99, 0.5$). With *Gaia* EDR3, there is one more spectroscopic member that has an astrometric solution compared to two in the *Gaia* DR2 catalog from the Kirby et al. (2015) spectroscopic sample.

As an alternative model, we rerun the mixture model but fix the three spectroscopic members in the dSph component. With this change, a proper motion signal is measured but no new members are identified. As the mixture model does not increase the number of members, we opt to calculate the systemic proper motion from the three known spectra members. Our result disagrees with McConnachie & Venn (2020b) likely due to their prior on tangential velocity that assumes the satellite is bound.

Ret II—This is one of the only objects with a well measured proper motions where our results differ from a result in the literature (Martínez-García et al. 2021). Ret II is a likely LMC satellite.

Sxt—We exclude the region around the globular cluster Palomar 3 ($R_{\text{Pal } 3} = 5 \times r_h$, $Pal \ 3 = 3.25'$) and the local field galaxy Sextans A ($R_{\text{Sxt A}} = 3 \times r_h$, $Sxt \ A \sim 7.4'$), when constructing the fixed background model.

Sgr—Sgr is clearly tidally disrupting and has a prominent stellar stream (Vasiliev et al. 2021). Sgr was not included in our primary sample due to its large angular size. We include the parameters we use for this analysis for reference: $r_{\text{peri}} = 16$ kpc (Vasiliev et al. 2021), $r_{1/2} = 2500$ pc, $\epsilon = 0.64$, and $d = 26.5$ kpc (McConnachie 2012).

Sgr II—The second system in our sample that is likely to be a globular cluster (Longeard et al. 2021a; Baumgardt et al. 2022).

Tuc III—We consider this dSph to be clearly tidally disrupting based on its tidal tails (Drlica-Wagner et al. 2015) and a velocity gradient (Li et al. 2018b).

Tuc IV—Tuc IV is above the LMC escape velocity at its closest approach to LMC and is unlikely to be LMC satellite. It is currently within the LMC escape velocity and may have been recently captured by the LMC. It had a close encounter with the LMC (see also Simon et al. 2020).

Tuc V—There was not a signal observed in similar *Gaia* DR2 (Pace & Li 2019) but a clear signal observed in *Gaia* EDR3. We are able to identify a signal without using of spectroscopic membership as prior information but note that the systemic proper motion can be measured more precisely including this information (e.g., Battaglia et al. 2022).

Wil 1—Roughly half of the stars (9/16) identified as candidate members in Table 2 of Willman et al. (2011) with matches to the *Gaia* EDR3 catalog are clearly MW foreground stars based on their parallax and/or proper motions. It is clear that any future kinematic analysis should include *Gaia* astrometry to improve the remove of foreground contamination.

C. EXTRA FIGURES

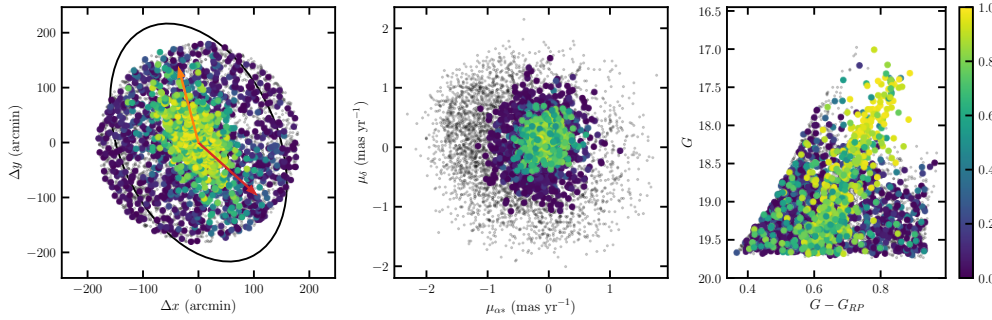


Figure 14. Diagnostic plot for Antlia II similar to Figure 2. The three rows are the spatial distribution (tangent plane), the proper motion (vector point diagram), and a *Gaia* color-magnitude diagram. Points with membership probability $p > 0.01$ are colored according to their probability; the rest are considered as MW stars and are shown as grey points. The red arrow points toward the Galactic center and the orange arrow is the direction of the reflex-corrected proper motion which is approximately equal to the orbital motion.

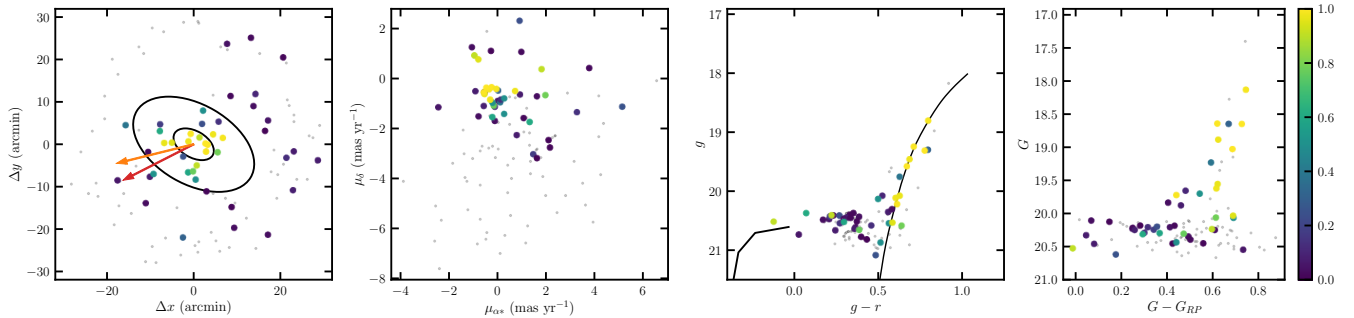


Figure 15. Similar to Figure 14 but for Aquarius II. The center-right panel is a DECam color-magnitude diagram.

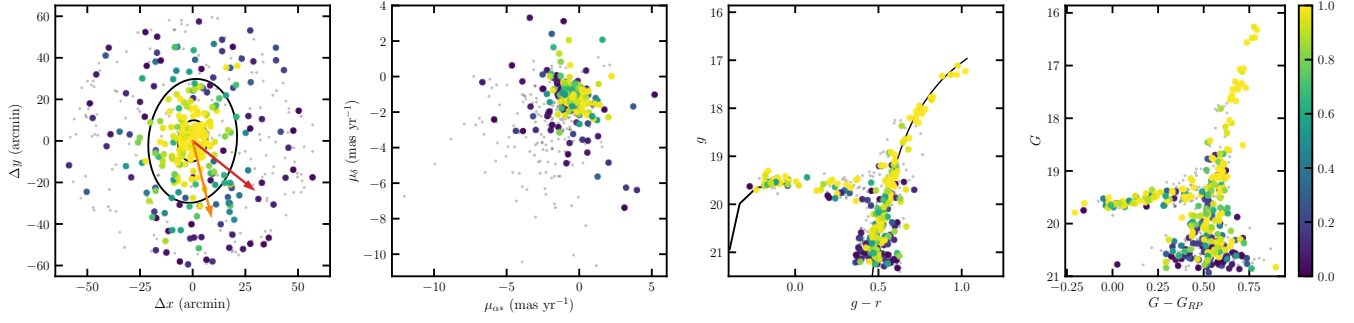


Figure 16. Same as Figure 15 but for Boötes I.

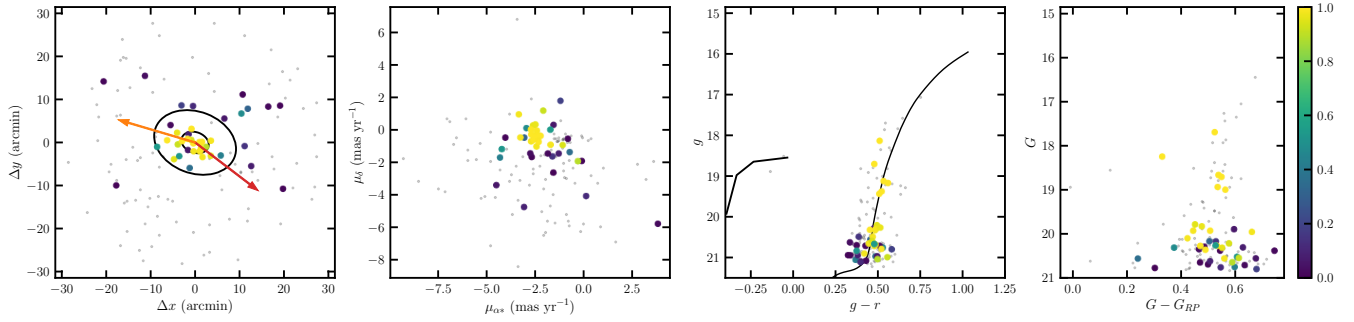


Figure 17. Same as Figure 15 but for Boötes II.

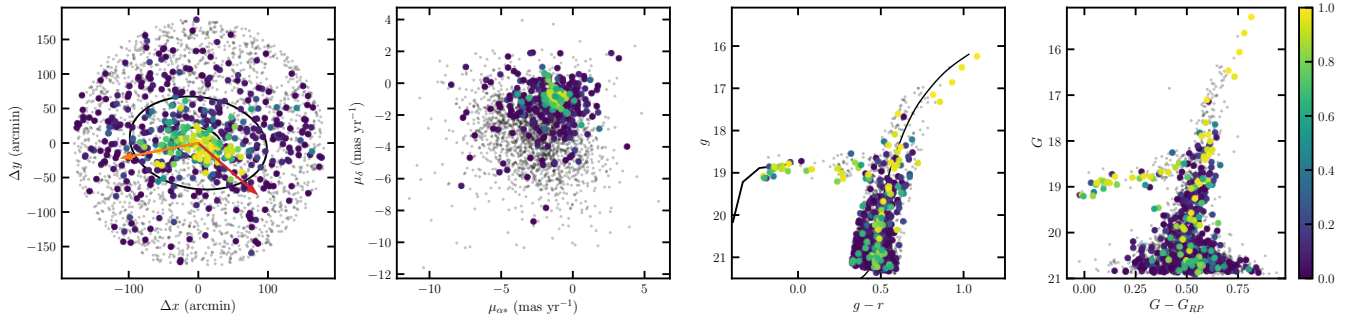


Figure 18. Same as Figure 15 but for Boötes III.

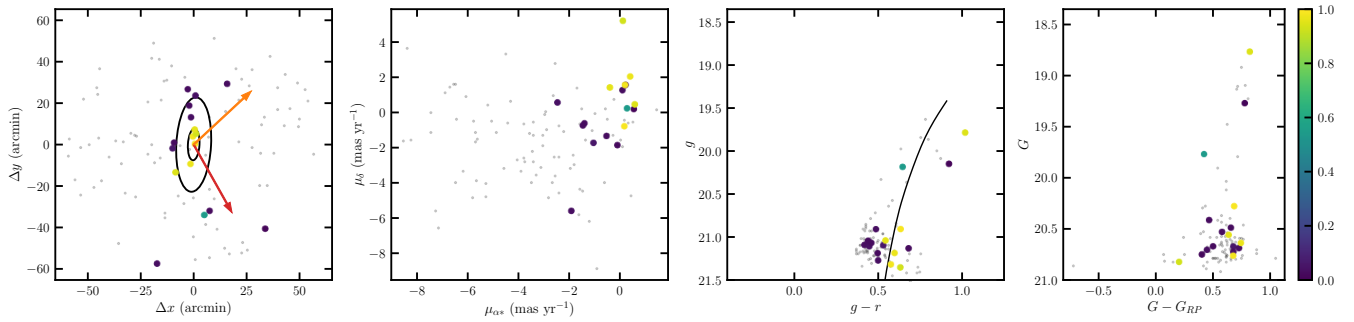


Figure 19. Same as Figure 15 but for Boötes IV. Includes PS1 photometry instead of DECam.

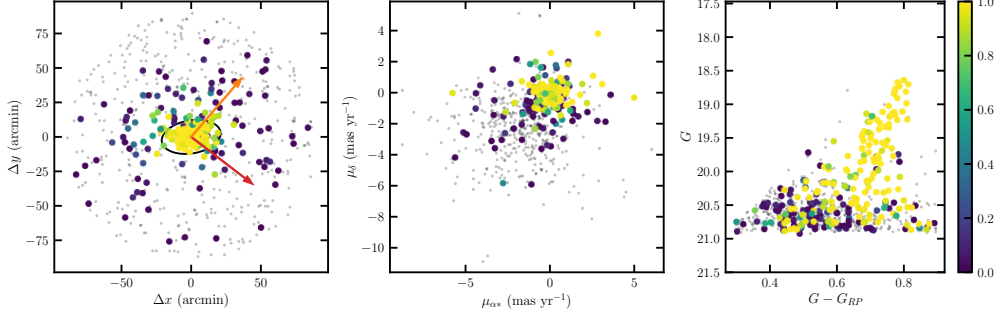


Figure 20. Same as Figure 14 but for Canes Venatici I.

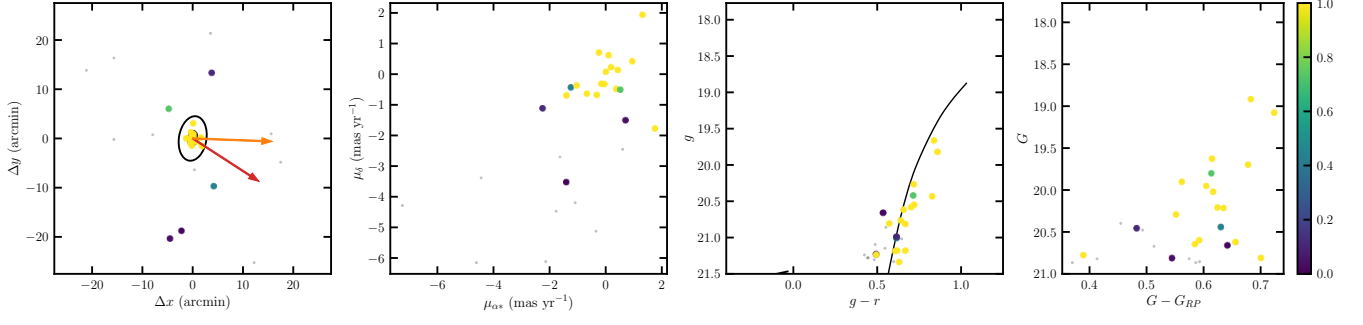


Figure 21. Same as Figure 15 but for Canes Venatici II.

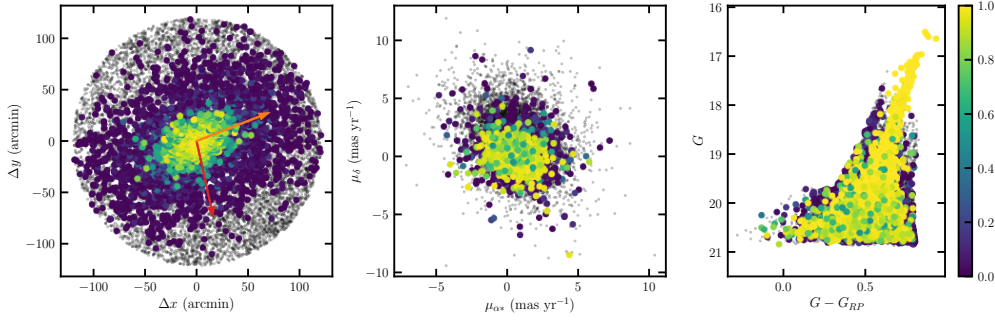


Figure 22. Same as Figure 14 but for Carina.

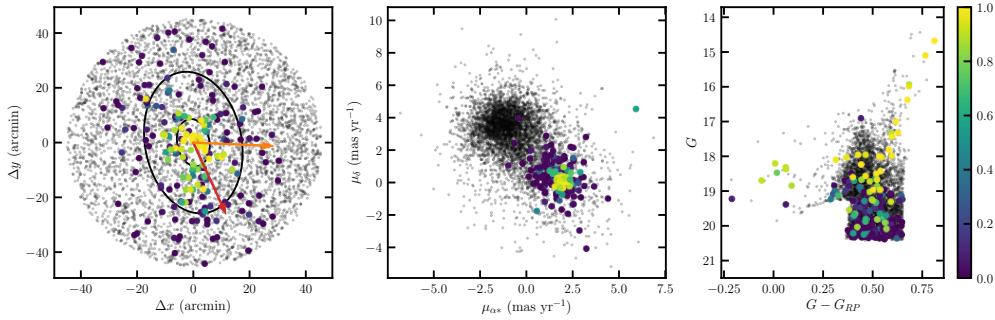


Figure 23. Same as Figure 14 but for Carina II. The region overlaps with Carina III.

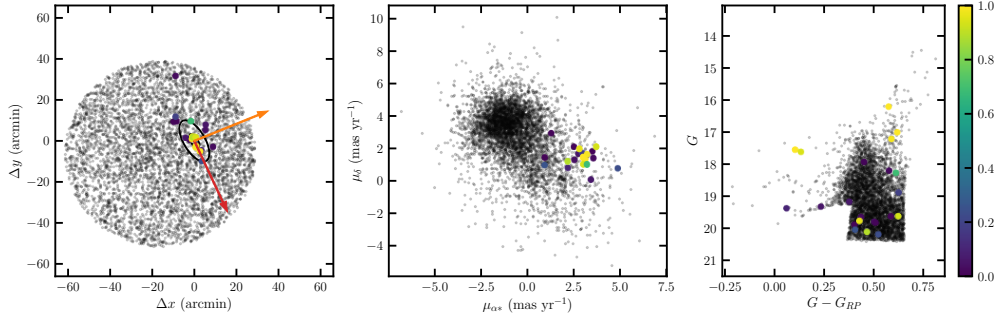


Figure 24. Same as Figure 14 but for Carina III. The area is center on Carina II.

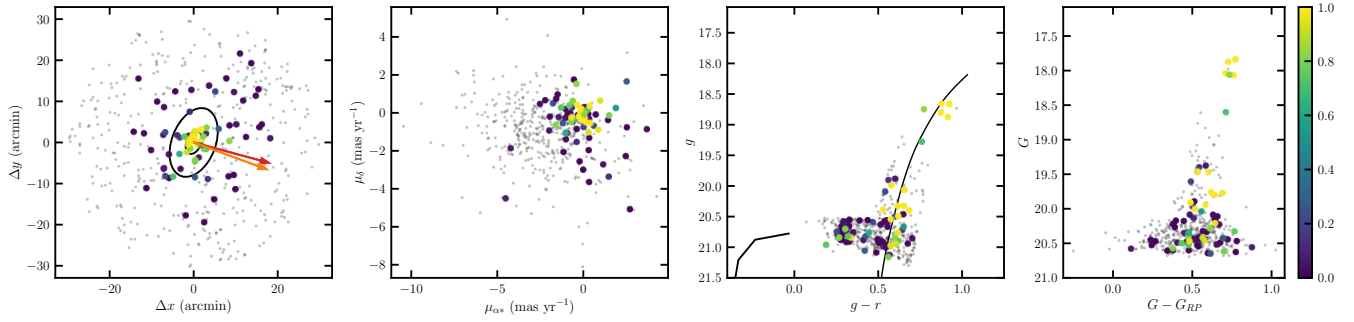


Figure 25. Same as Figure 15 but for Centaurus I.

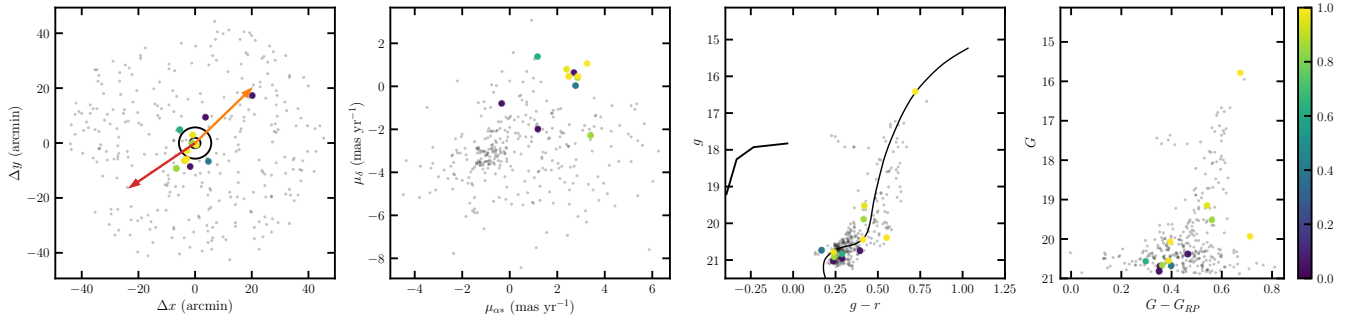


Figure 26. Same as Figure 15 but for Cetus II.

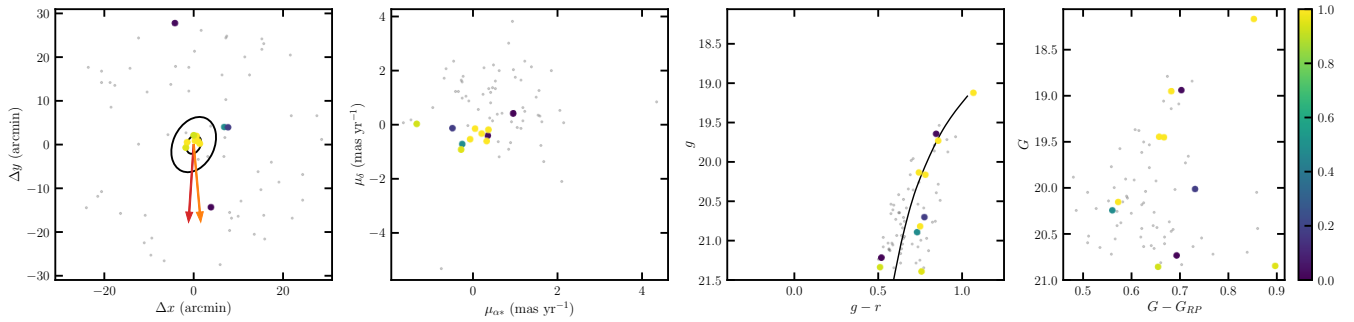


Figure 27. Same as Figure 15 but for Columba I.

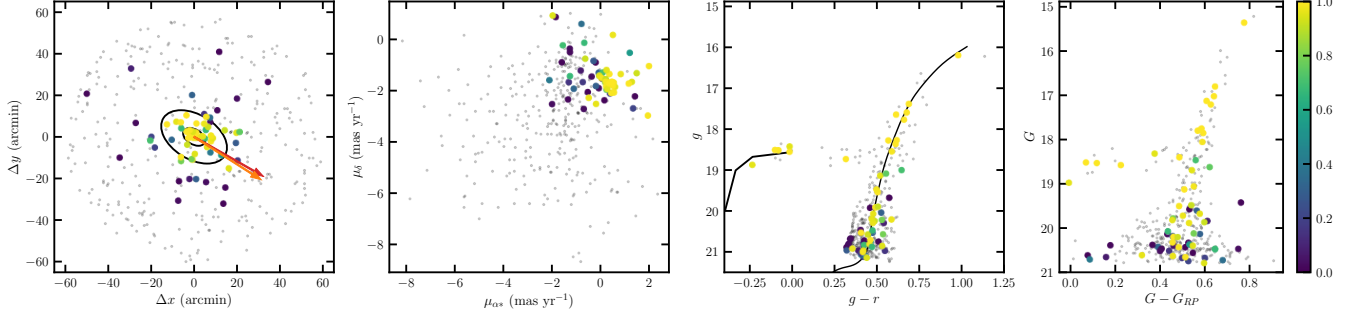


Figure 28. Same as Figure 15 but for Coma Berenices.

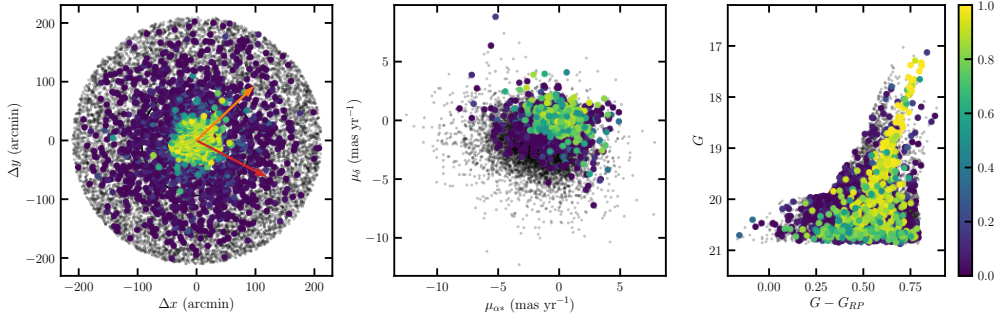


Figure 29. Same as Figure 14 but for Crater II.

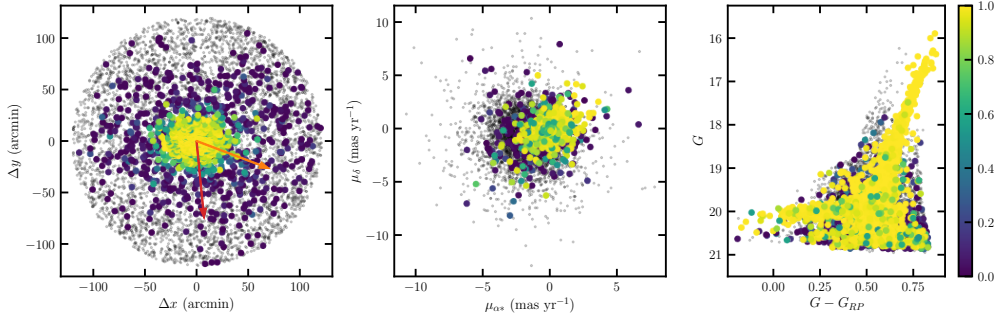


Figure 30. Same as Figure 14 but for Draco.

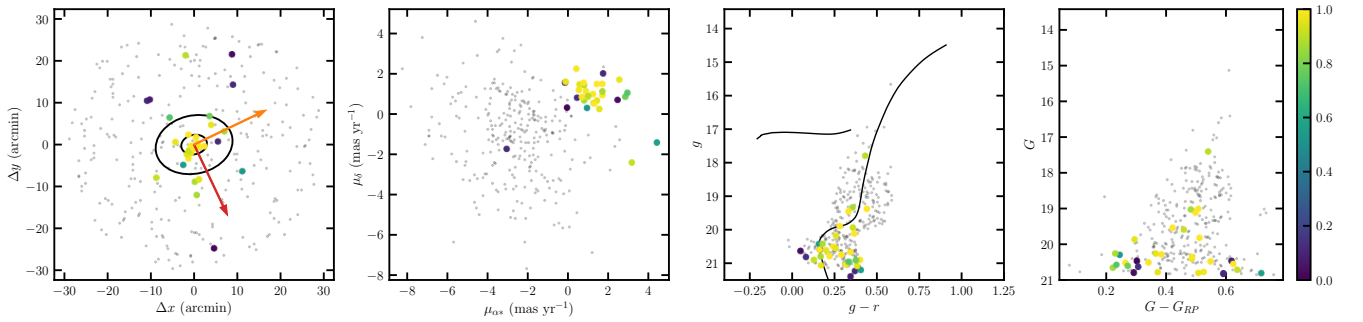


Figure 31. Same as Figure 15 but for Draco II.

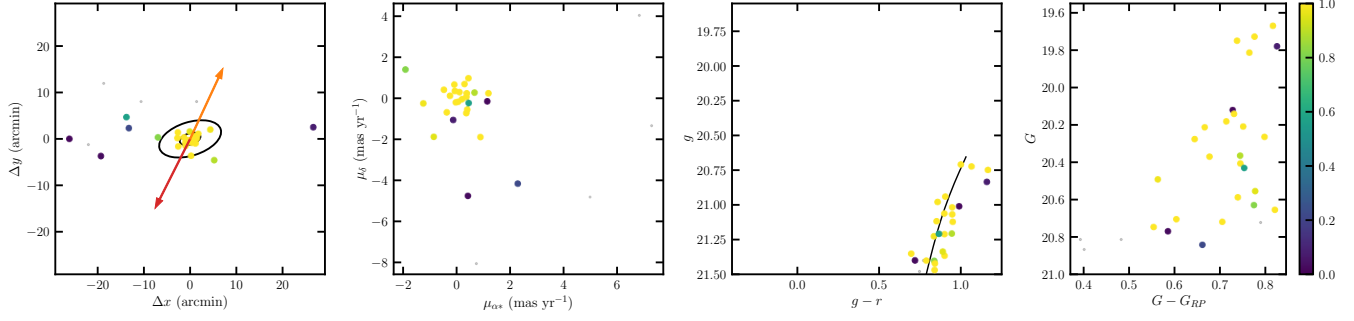


Figure 32. Same as Figure 15 but for Eridanus II.

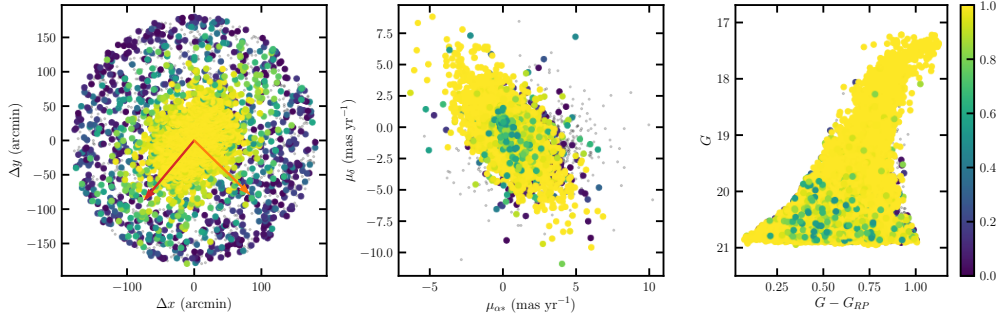


Figure 33. Same as Figure 14 but for Fornax.

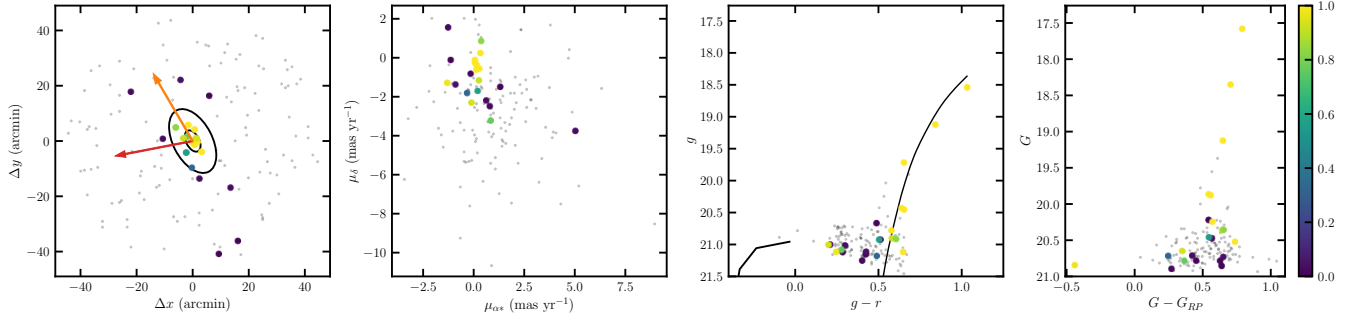


Figure 34. Same as Figure 15 but for Grus I.

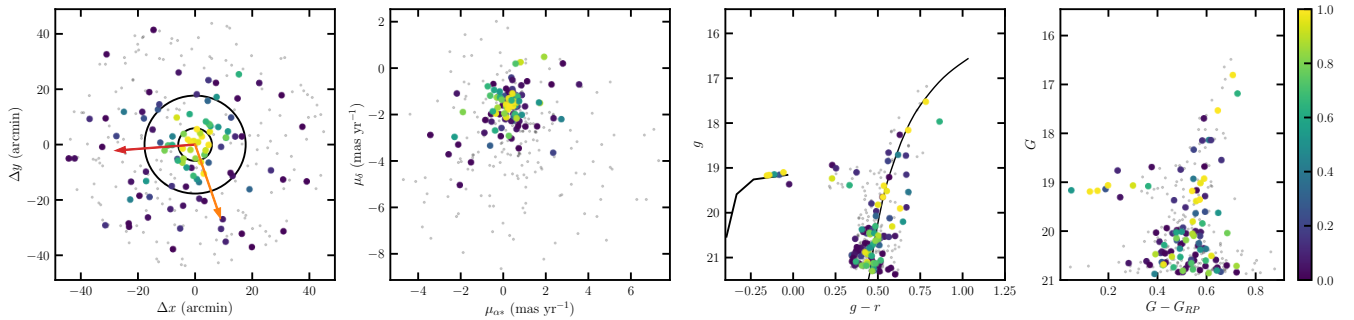


Figure 35. Same as Figure 15 but for Grus II.

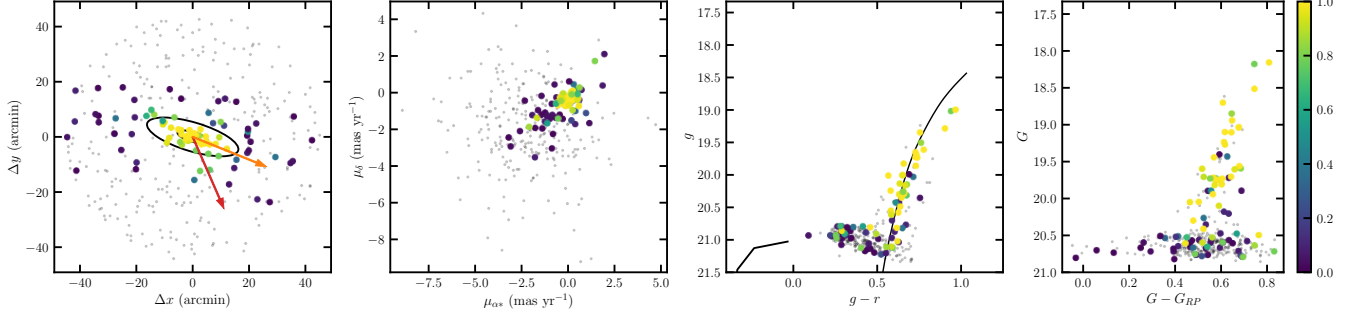


Figure 36. Same as Figure 15 but for Hercules.

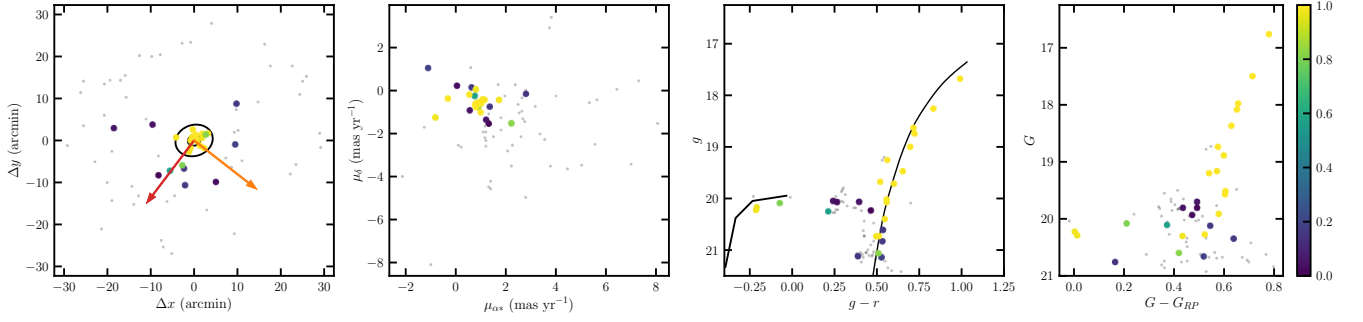


Figure 37. Same as Figure 15 but for Horologium I.

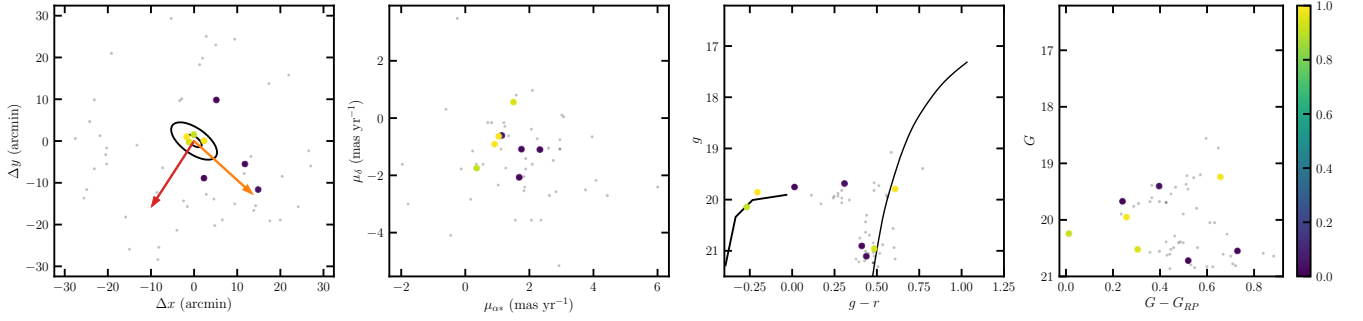


Figure 38. Same as Figure 15 but for Horologium II.

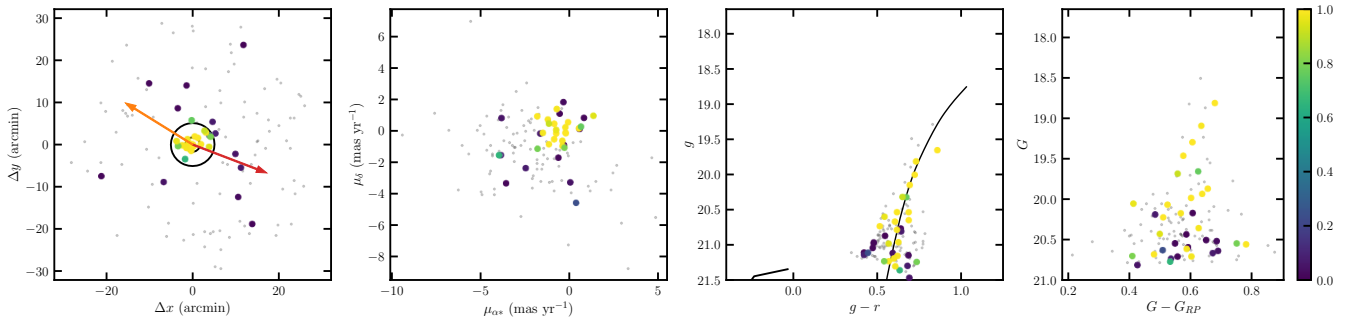


Figure 39. Same as Figure 15 but for Hydra II.

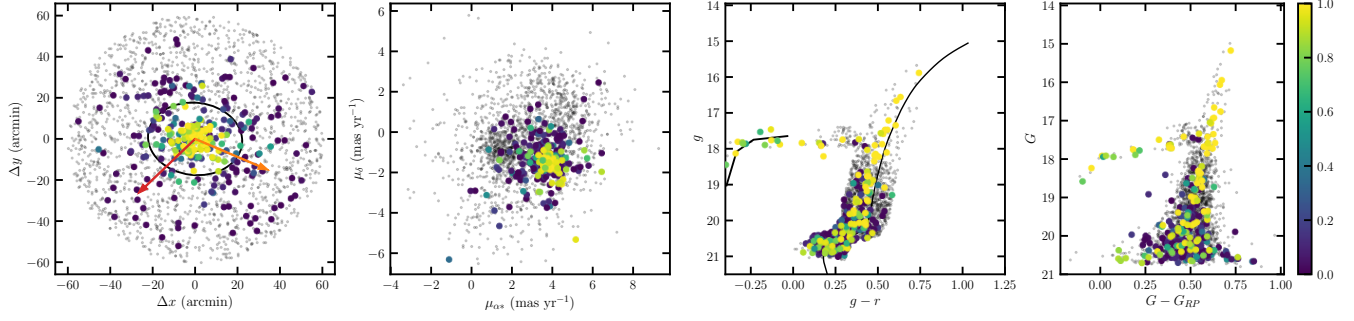


Figure 40. Same as Figure 15 but for Hydrus I.

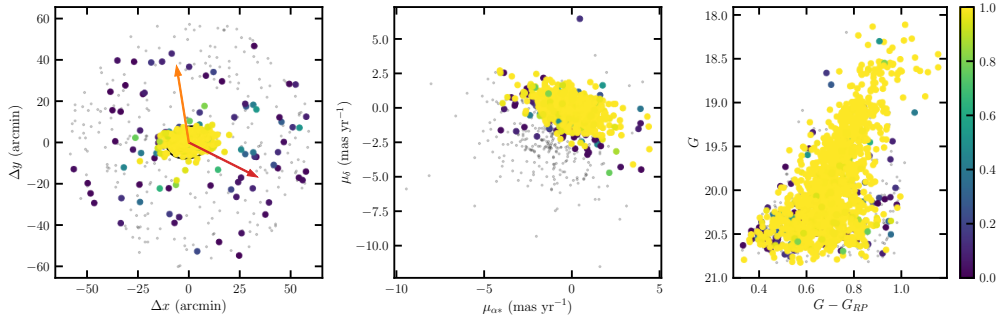


Figure 41. Same as Figure 14 but for Leo I.

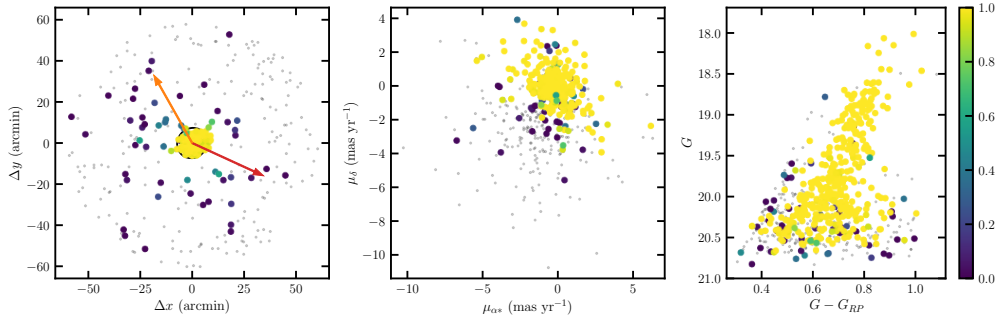


Figure 42. Same as Figure 14 but for Leo II.

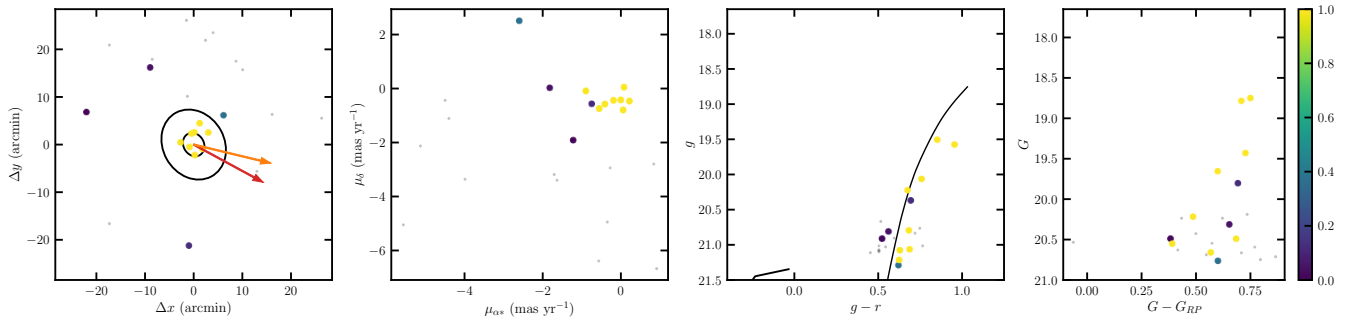


Figure 43. Same as Figure 15 but for Leo IV.

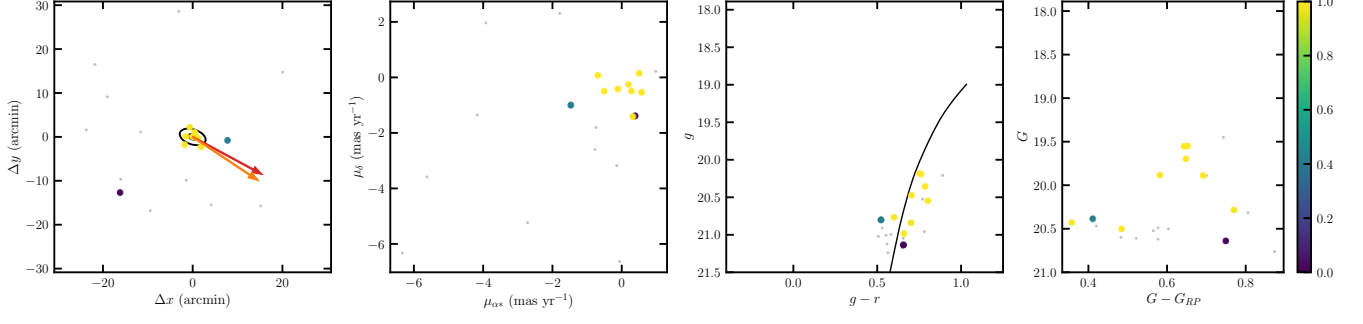


Figure 44. Same as Figure 15 but for Leo V.

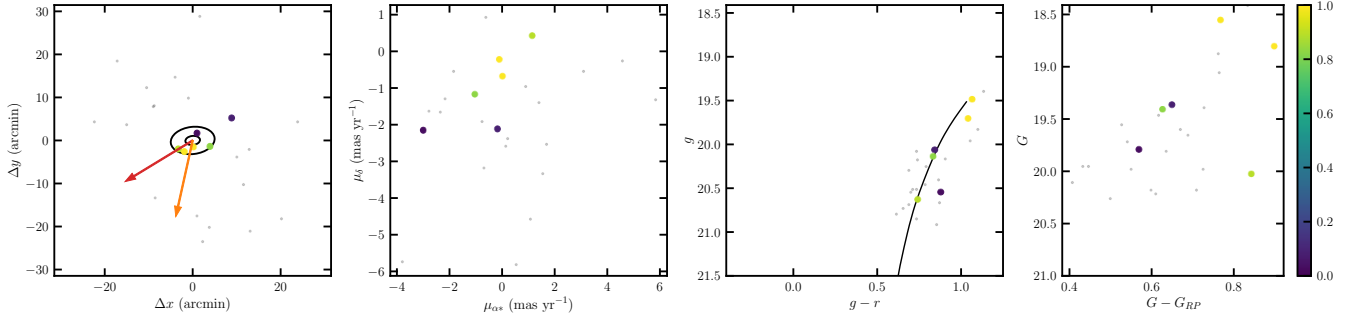


Figure 45. Same as Figure 15 but for Pegasus III.

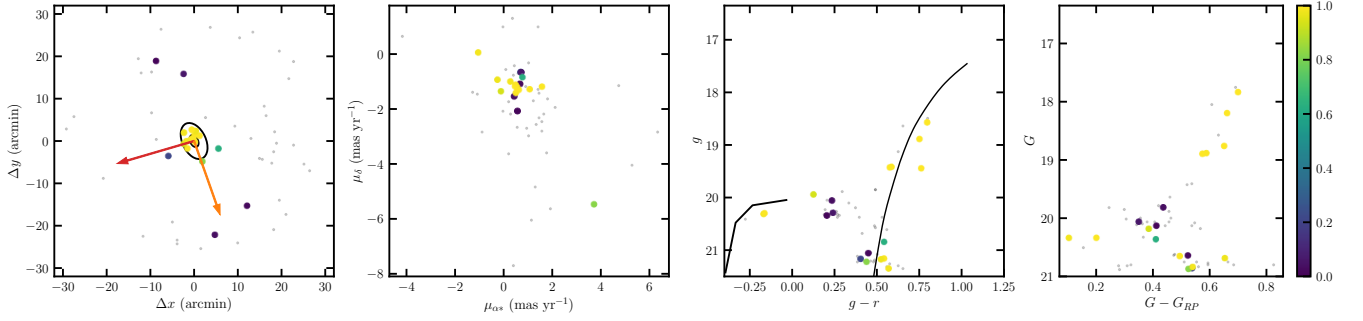


Figure 46. Same as Figure 15 but for Phoenix II.

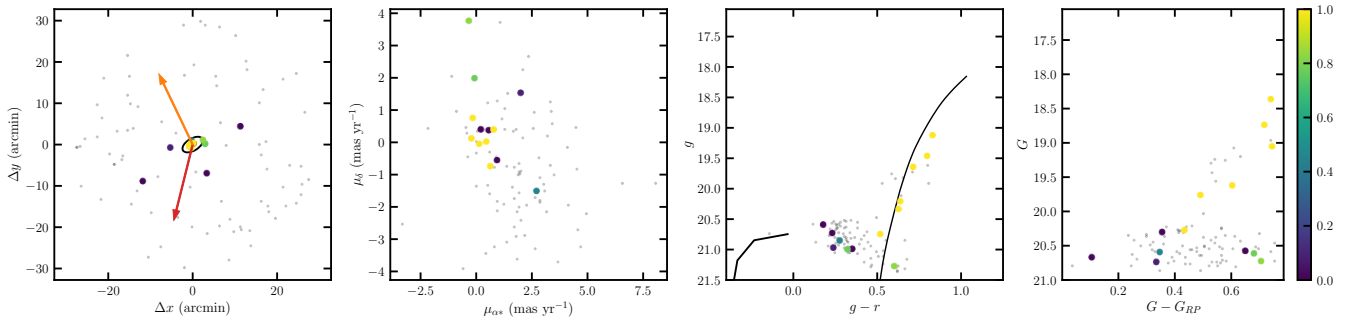


Figure 47. Same as Figure 15 but for Pictor I.

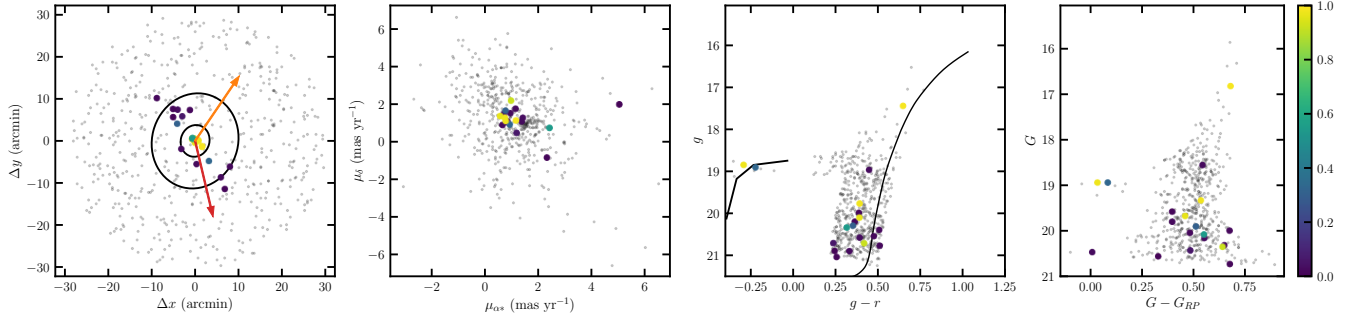


Figure 48. Same as Figure 15 but for Pictor II. There is color offset in the NSC data that is unaccounted for in the isochrone.

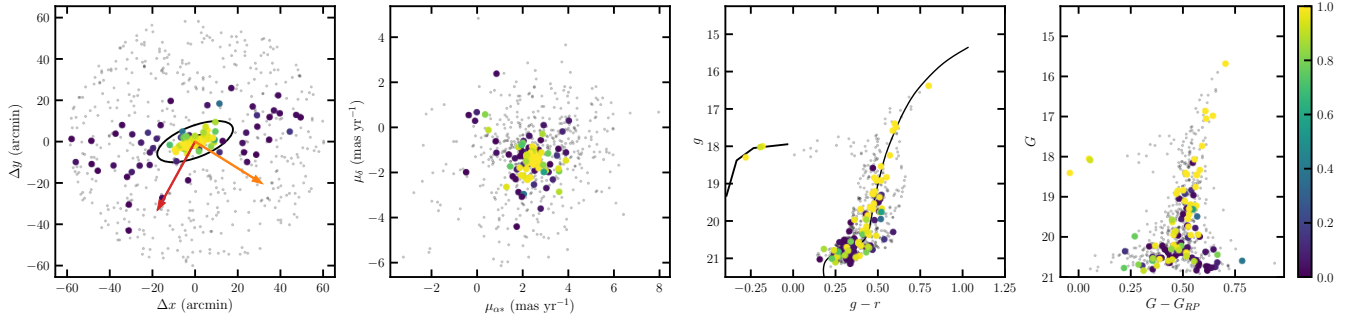


Figure 49. Same as Figure 15 but for Reticulum II.

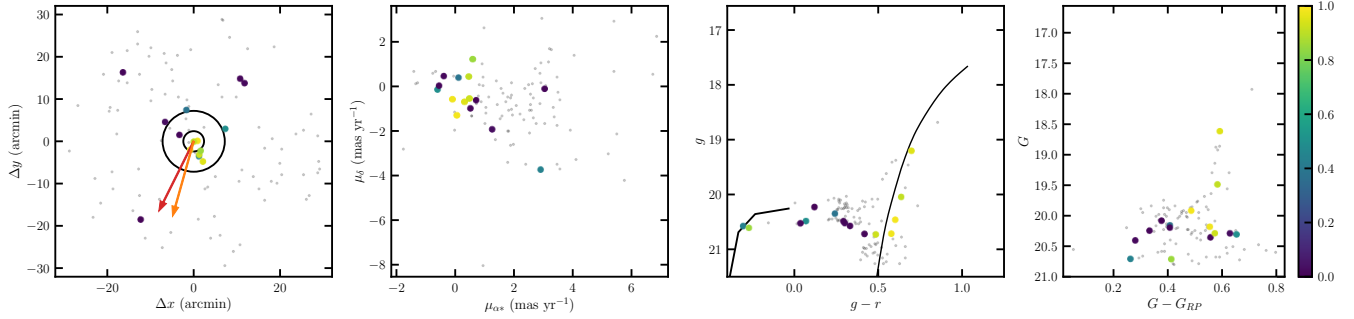


Figure 50. Same as Figure 15 but for Reticulum III.

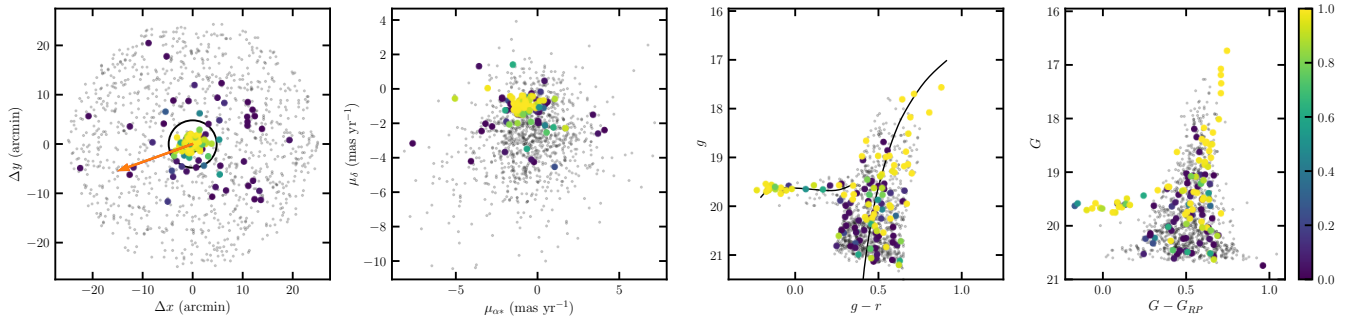


Figure 51. Same as Figure 15 but for Sagittarius II.

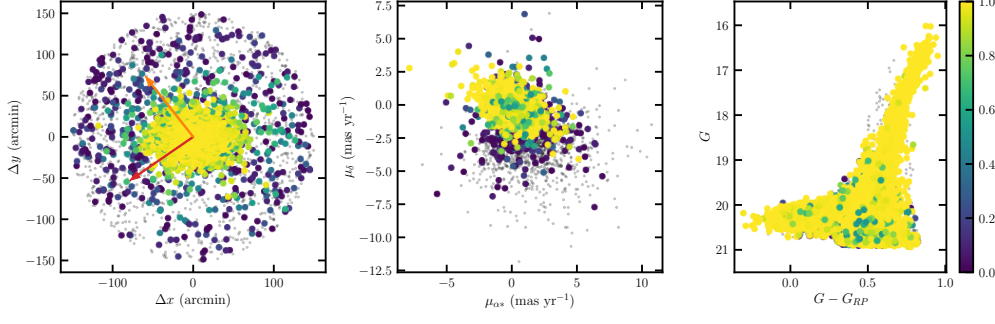


Figure 52. Same as Figure 14 but for Sculptor.

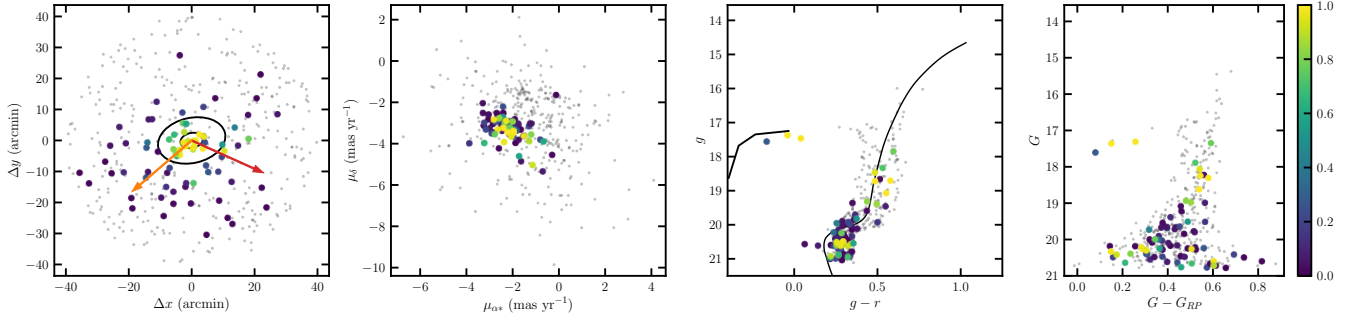


Figure 53. Same as Figure 15 but for Segue 1.

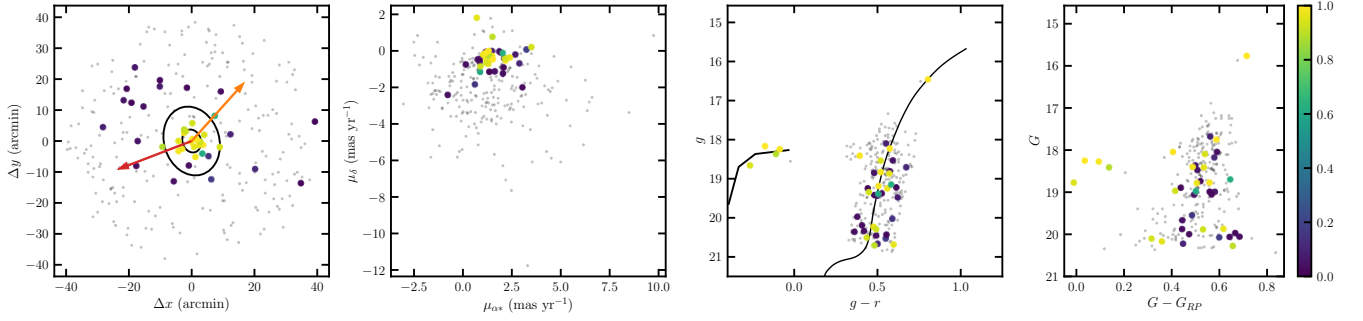


Figure 54. Same as Figure 15 but for Segue 2.

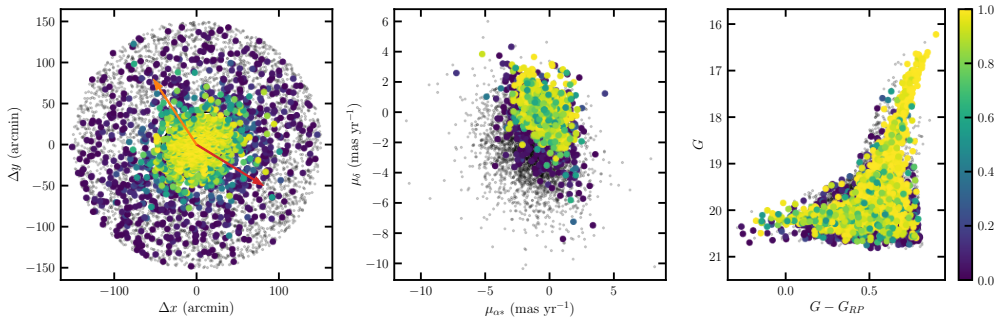


Figure 55. Same as Figure 14 but for Sextans.

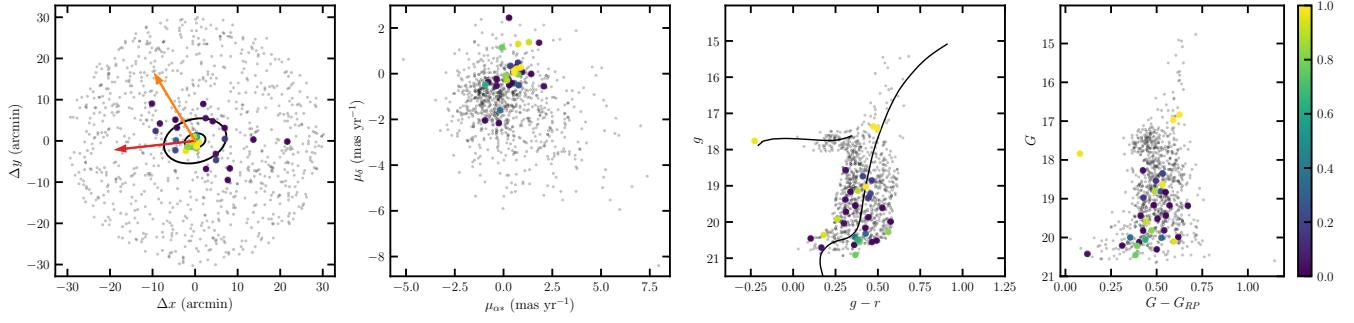


Figure 56. Same as Figure 15 but for Triangulum II.

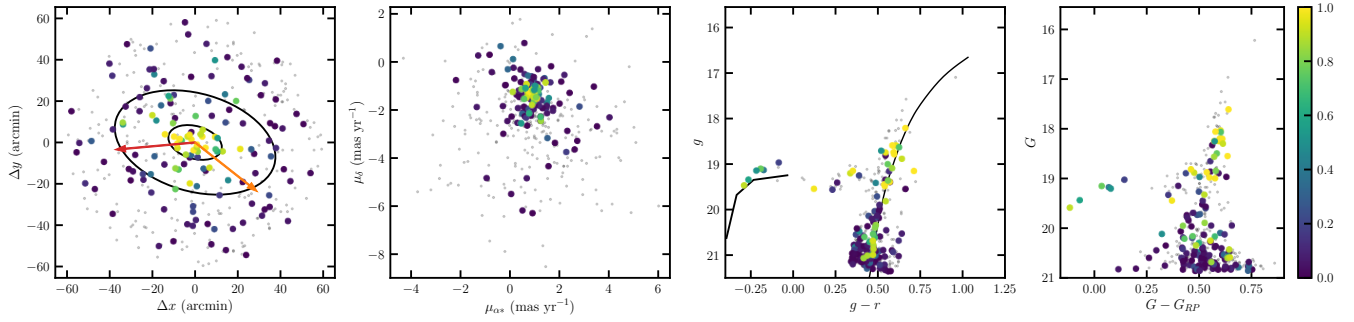


Figure 57. Same as Figure 15 but for Tucana II.

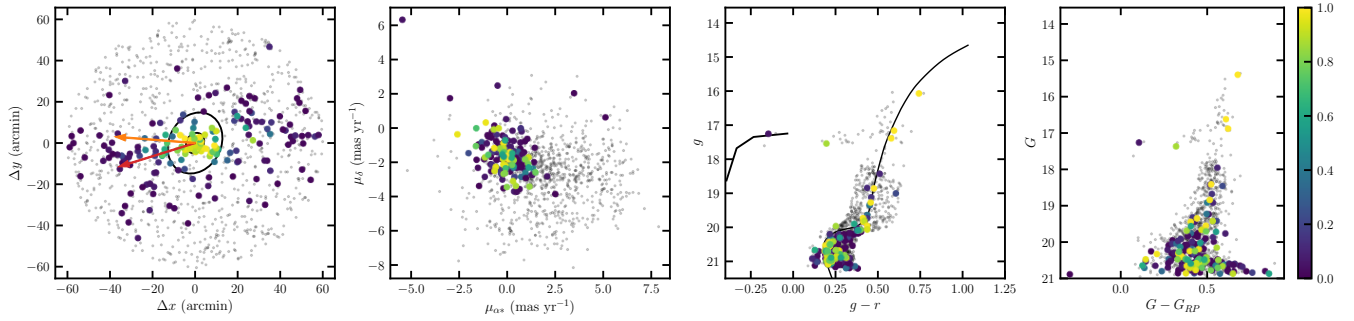


Figure 58. Same as Figure 15 but for Tucana III.

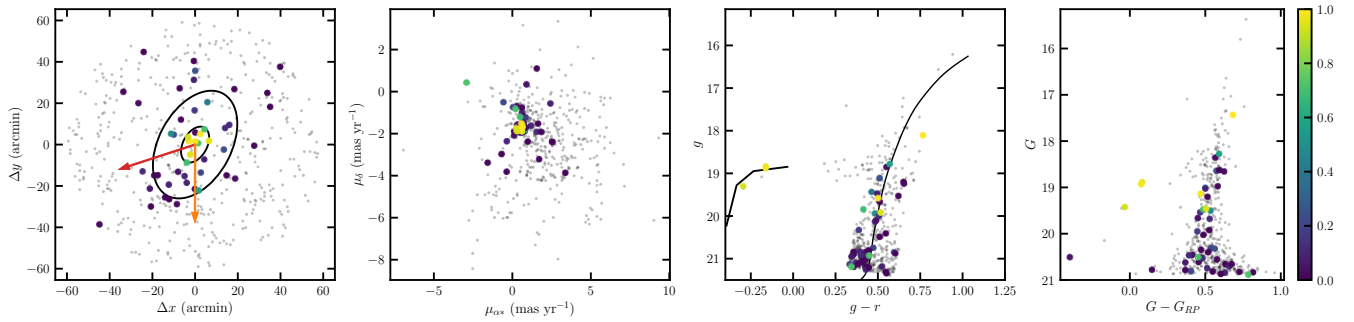


Figure 59. Same as Figure 15 but for Tucana IV.

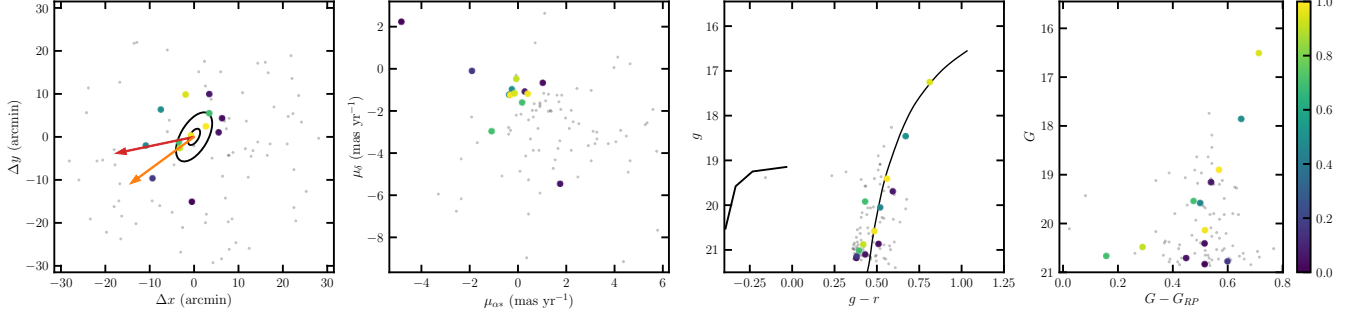


Figure 60. Same as Figure 15 but for Tucana V.

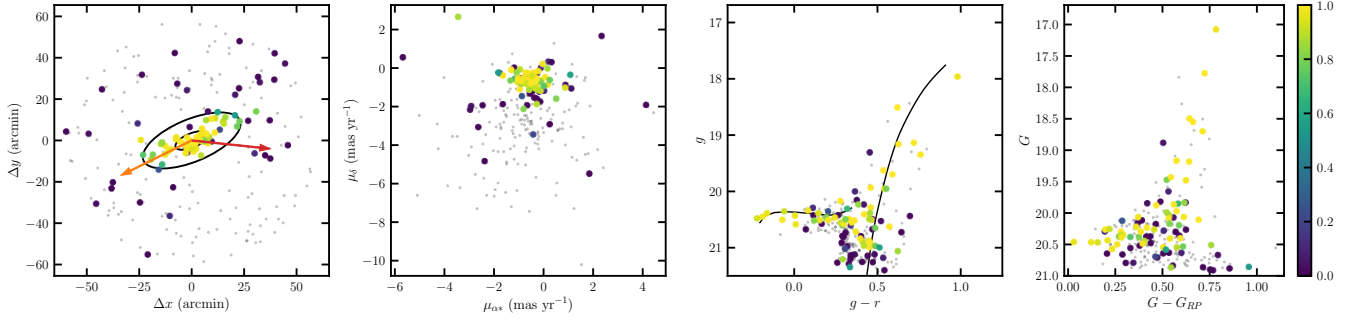


Figure 61. Same as Figure 15 but for Ursa Major I.

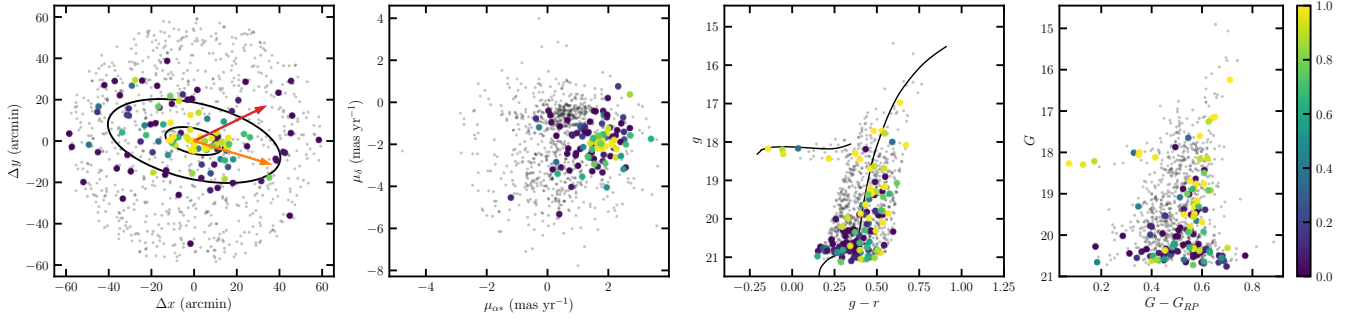


Figure 62. Same as Figure 15 but for Ursa Major II.

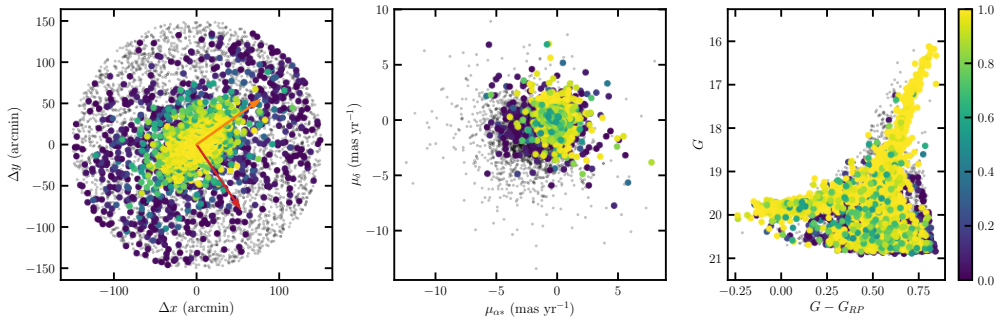


Figure 63. Same as Figure 14 but for Ursa Minor.

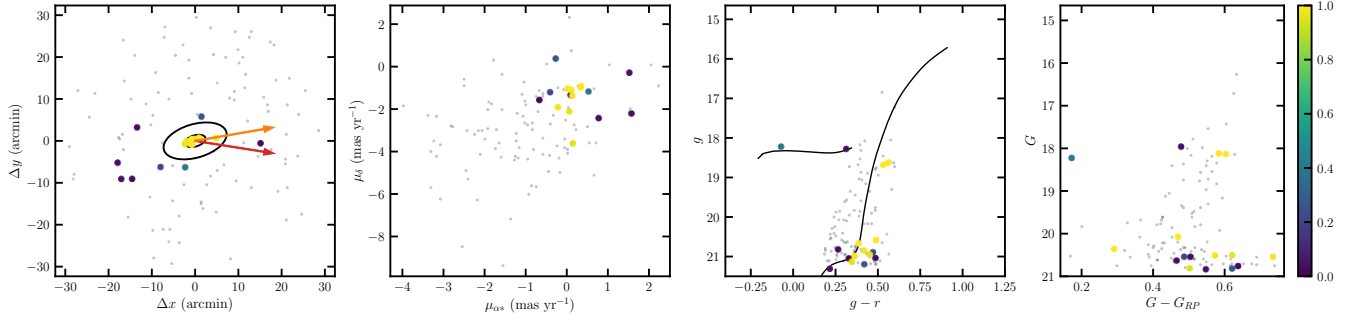


Figure 64. Same as Figure 15 but for Willman 1.

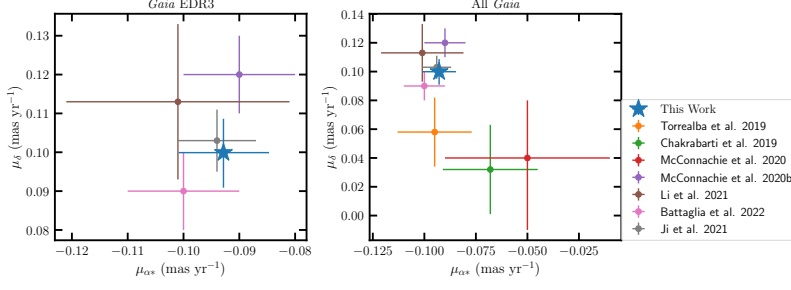


Figure 65. Comparison between our systemic proper motion measurement and literature measurements for Antlia II.

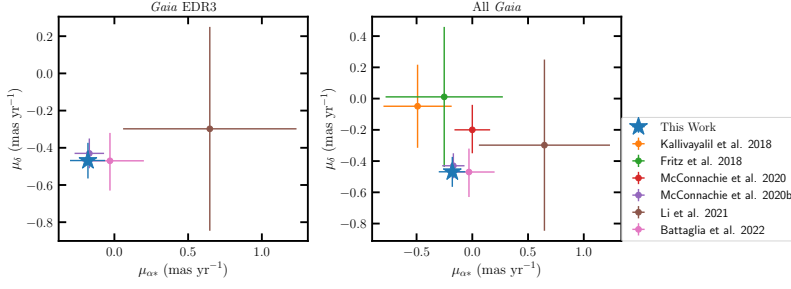


Figure 66. Same as Figure 65 but for Aquarius II.

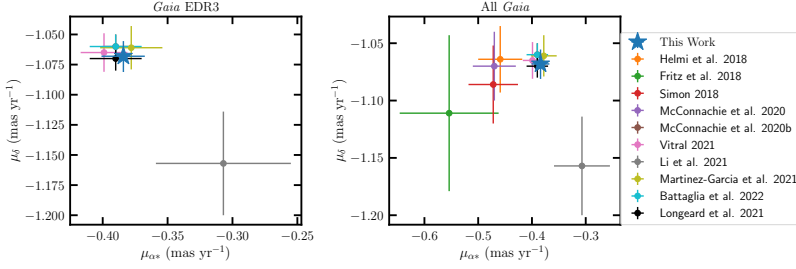


Figure 67. Same as Figure 65 but for Boötes I.

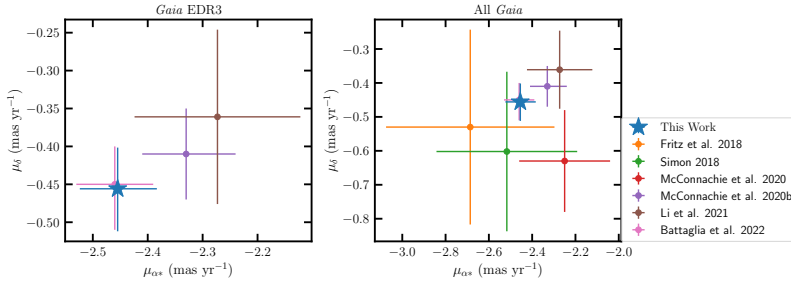


Figure 68. Same as Figure 65 but for Boötes II.

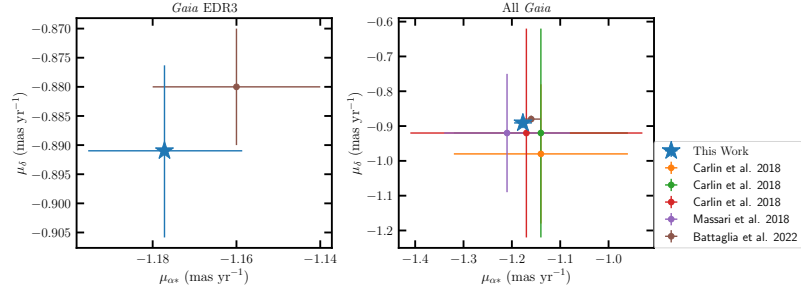


Figure 69. Same as Figure 65 but for Boötes III.

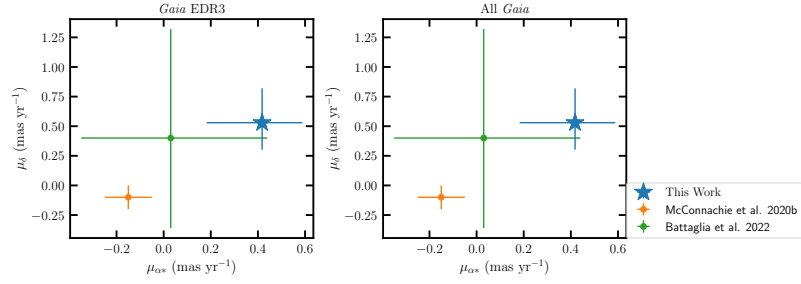


Figure 70. Same as Figure 65 but for Boötes IV.

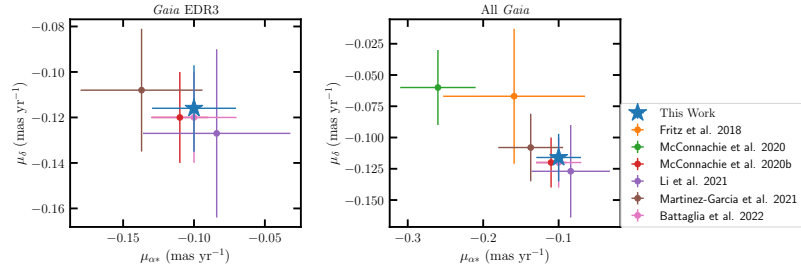


Figure 71. Same as Figure 65 but for Canes Venatici I.

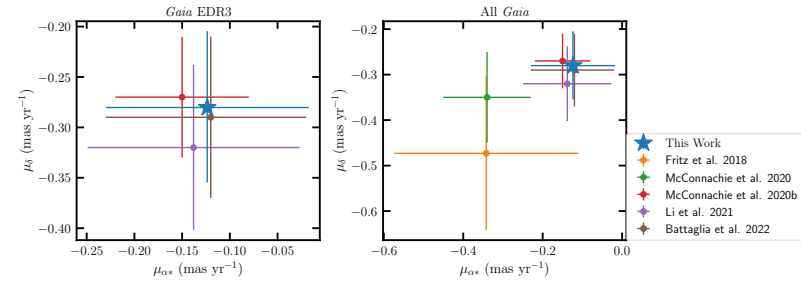


Figure 72. Same as Figure 65 but for Canes Venatici II.

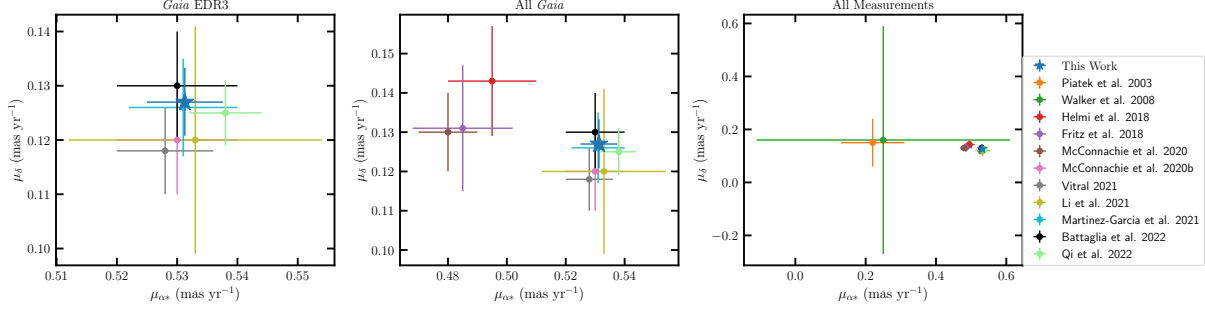


Figure 73. Same as Figure 65 but for Carina.

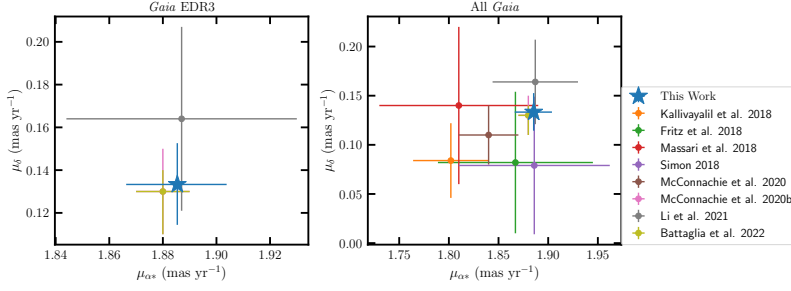


Figure 74. Same as Figure 65 but for Carina II.

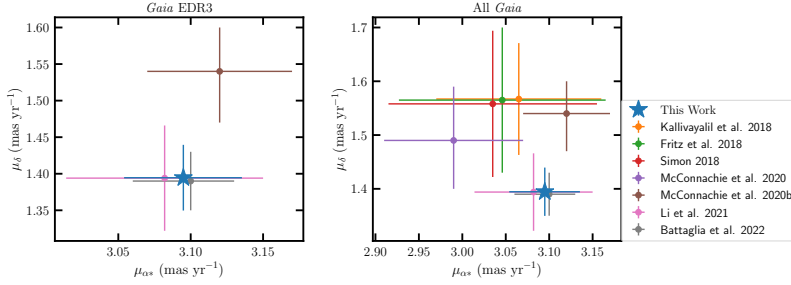


Figure 75. Same as Figure 65 but for Carina III.

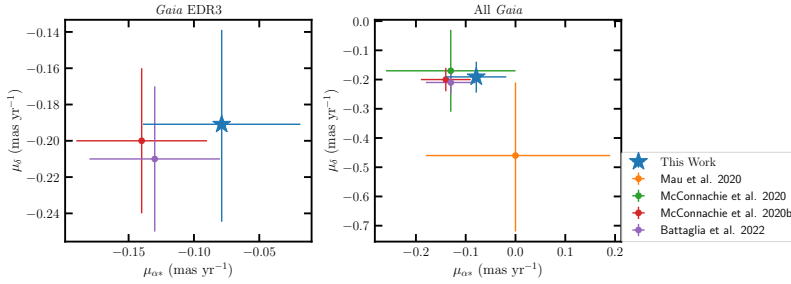


Figure 76. Same as Figure 65 but for Centaurus I.

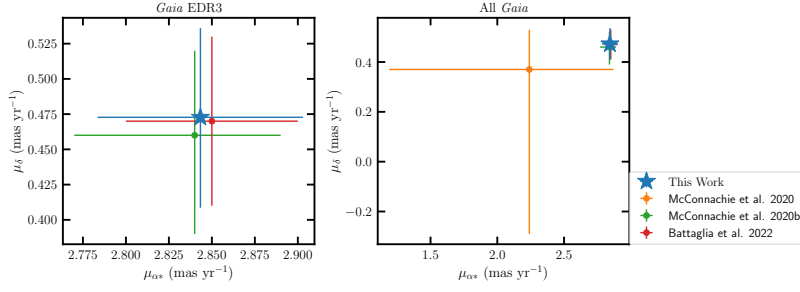


Figure 77. Same as Figure 65 but for Cetus II.

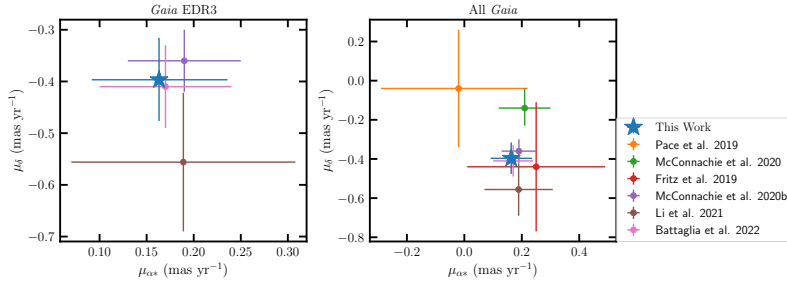


Figure 78. Same as Figure 65 but for Columba I.

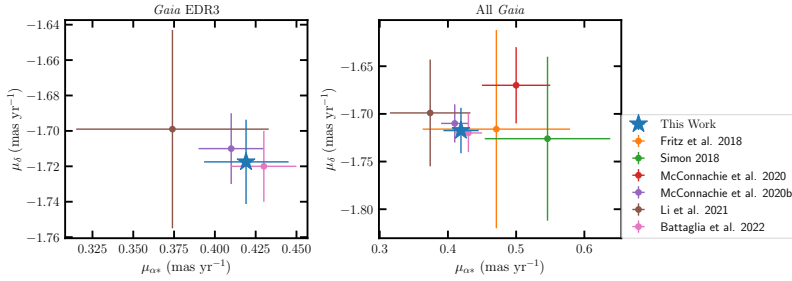


Figure 79. Same as Figure 65 but for Coma Berenices.

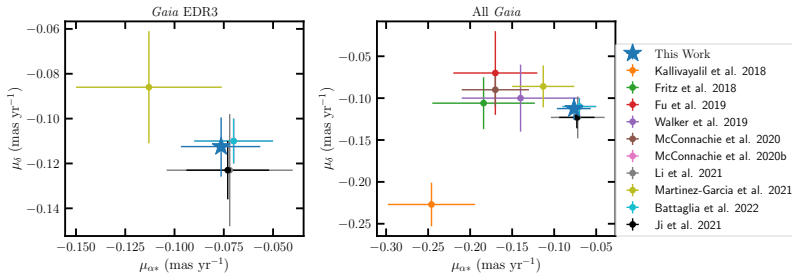


Figure 80. Same as Figure 65 but for Crater II.

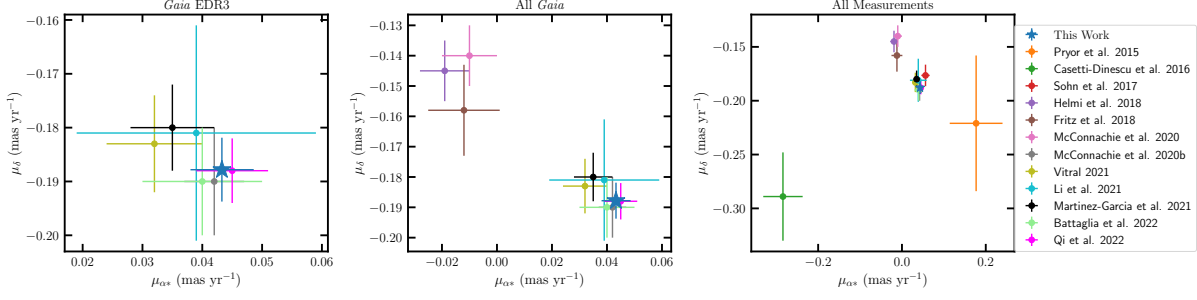


Figure 81. Same as Figure 65 but for Draco.

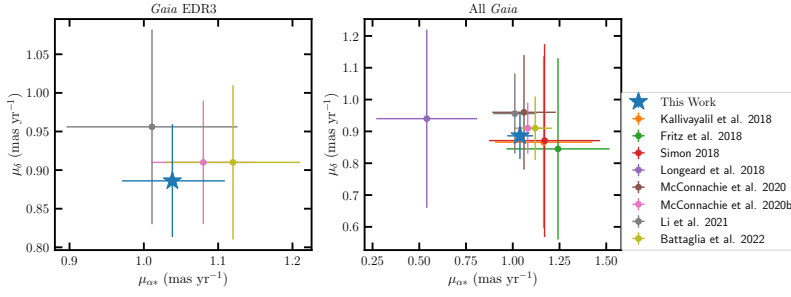


Figure 82. Same as Figure 65 but for Draco II.

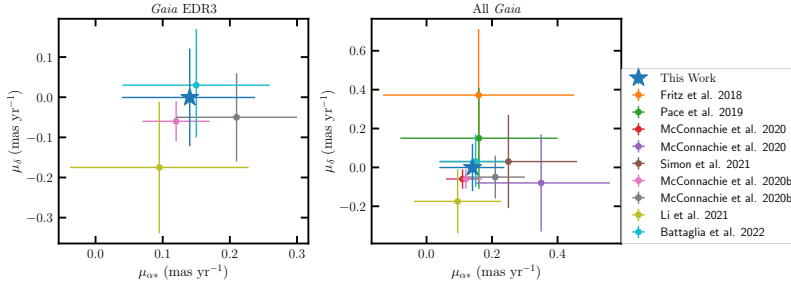


Figure 83. Same as Figure 65 but for Eridanus II.

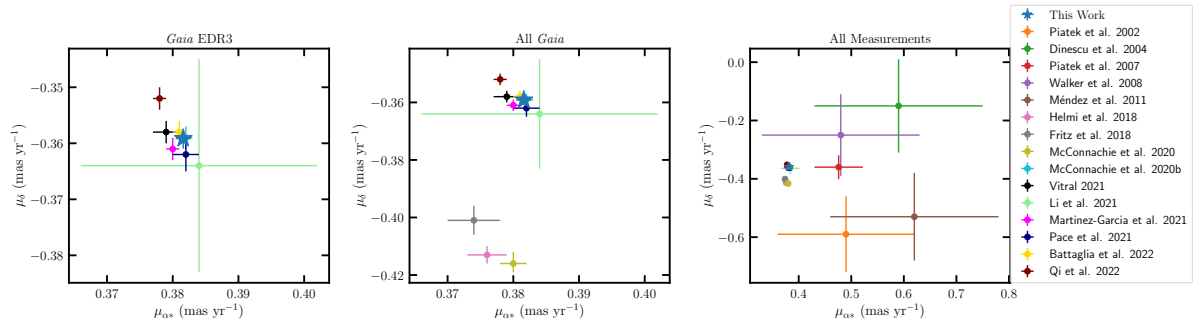


Figure 84. Same as Figure 65 but for Fornax.

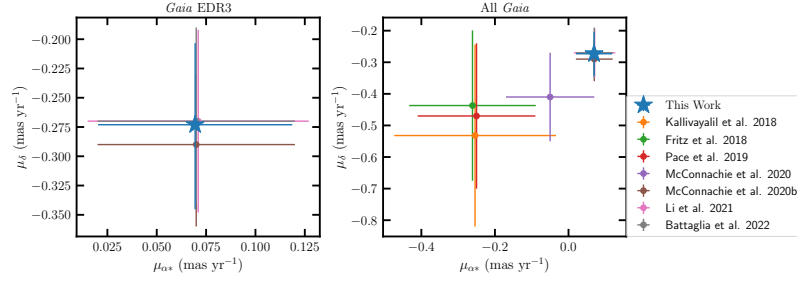


Figure 85. Same as Figure 65 but for Grus I.

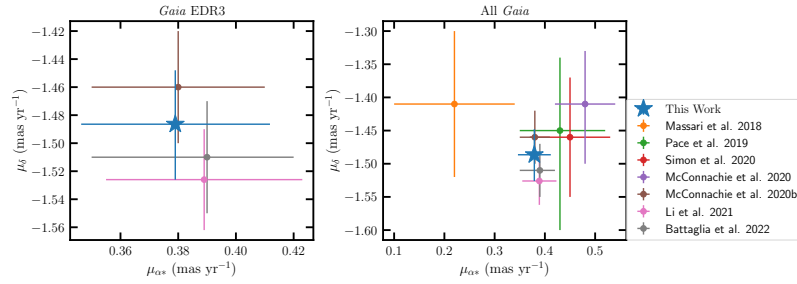


Figure 86. Same as Figure 65 but for Grus II.

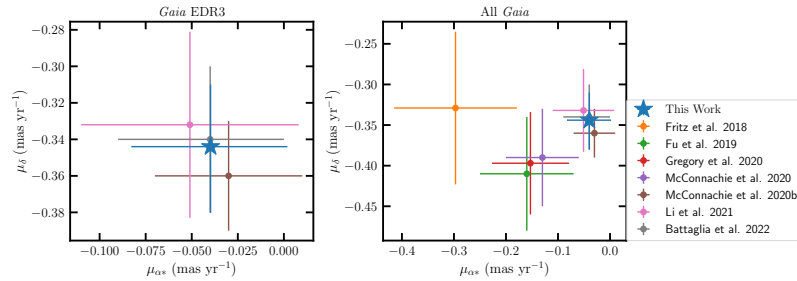


Figure 87. Same as Figure 65 but for Hercules.

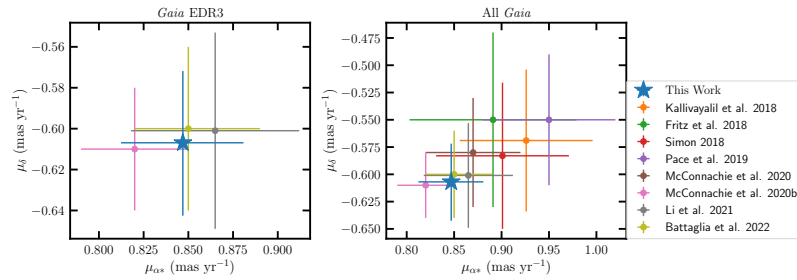


Figure 88. Same as Figure 65 but for Horologium I.

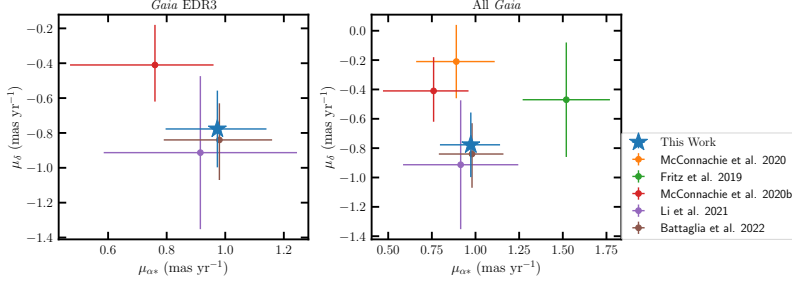


Figure 89. Same as Figure 65 but for Horologium II.

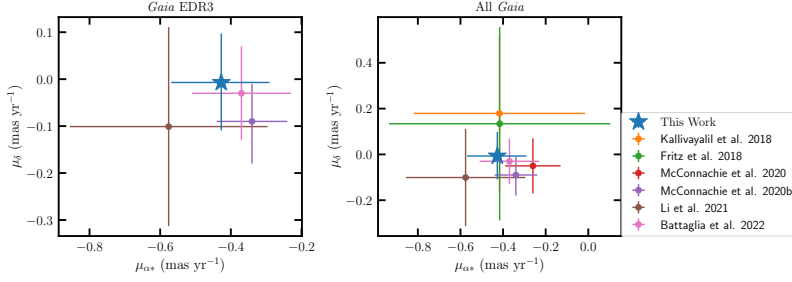


Figure 90. Same as Figure 65 but for Hydra II.

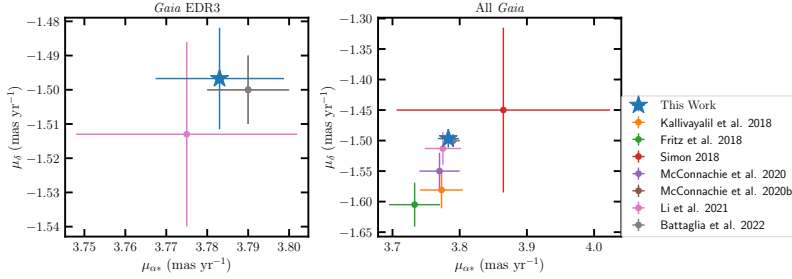


Figure 91. Same as Figure 65 but for Hydrus I.

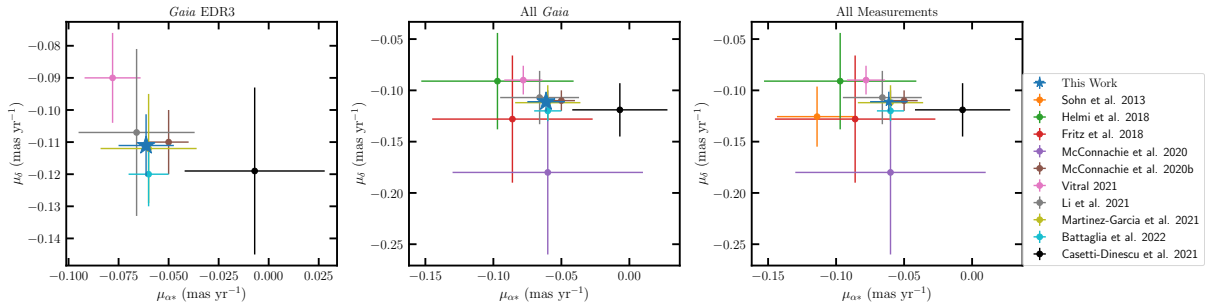


Figure 92. Same as Figure 65 but for Leo I.

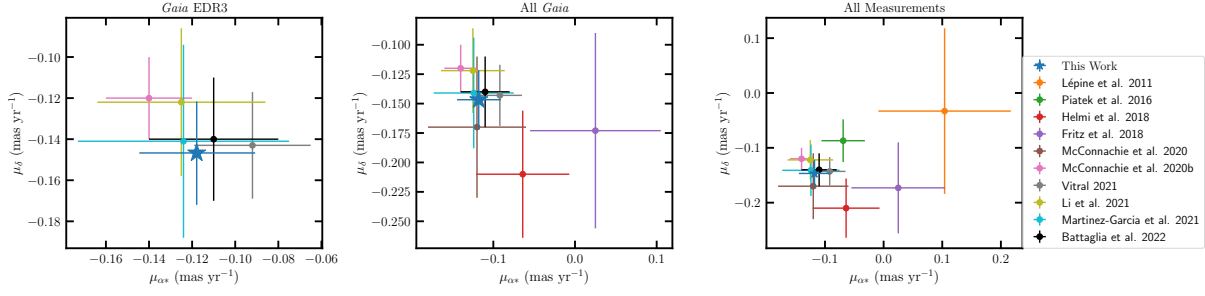


Figure 93. Same as Figure 65 but for Leo II.

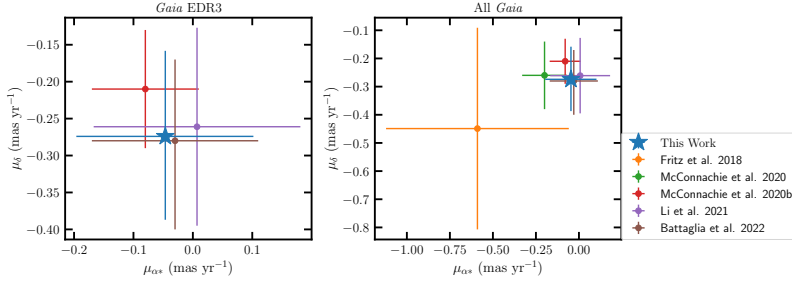


Figure 94. Same as Figure 65 but for Leo IV.

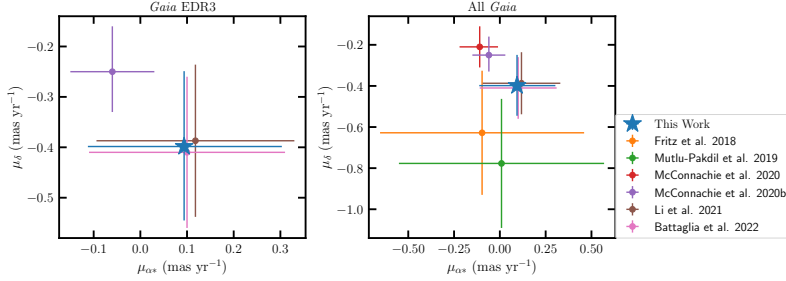


Figure 95. Same as Figure 65 but for Leo V.

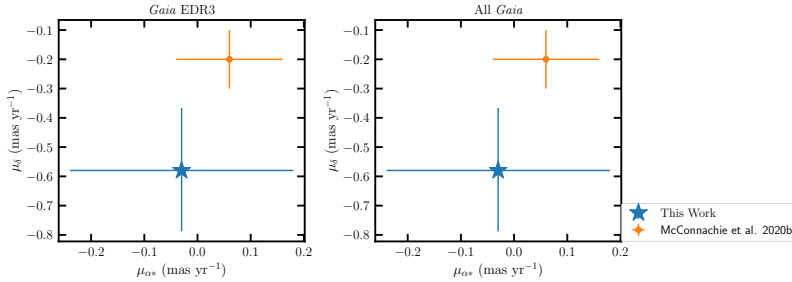


Figure 96. Same as Figure 65 but for Pegasus III.

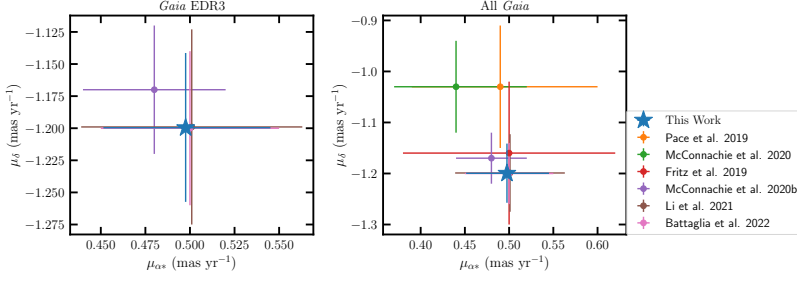


Figure 97. Same as Figure 65 but for Phoenix II.

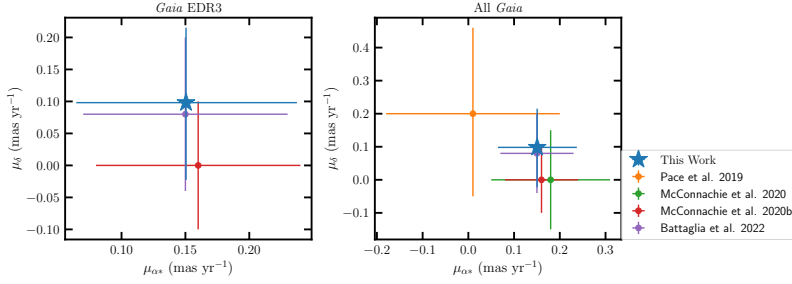


Figure 98. Same as Figure 65 but for Pictor I.

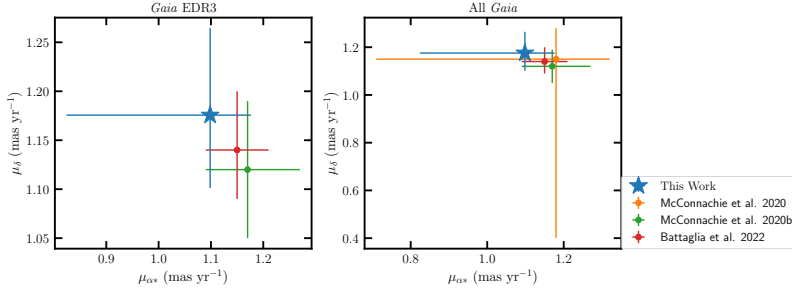


Figure 99. Same as Figure 65 but for Pictor II.

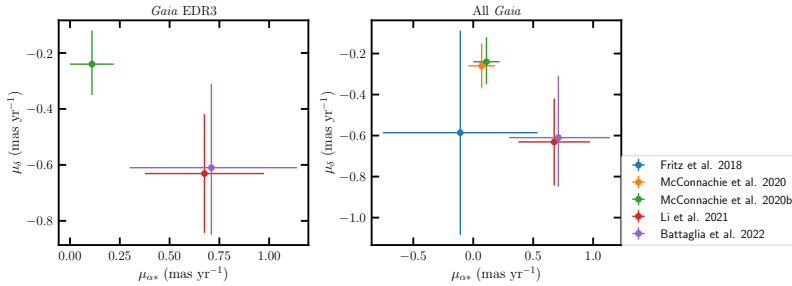


Figure 100. Same as Figure 65 but for Pisces II.

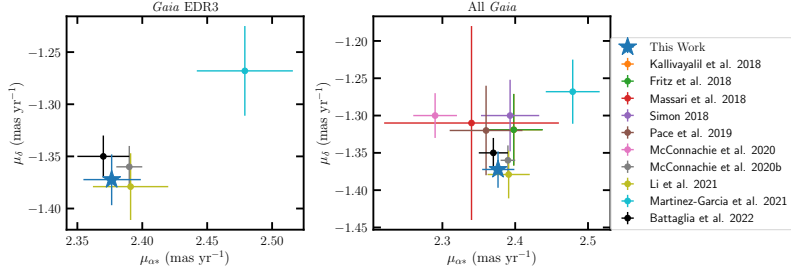


Figure 101. Same as Figure 65 but for Reticulum II.

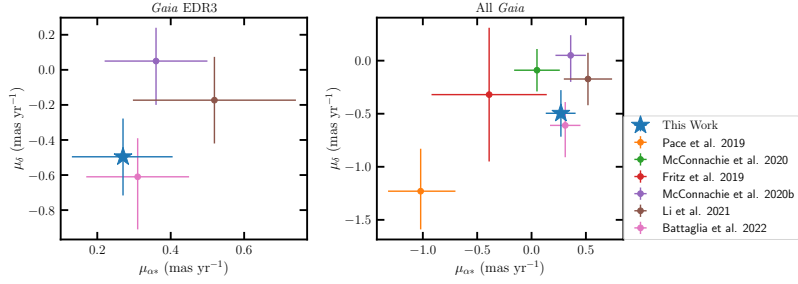


Figure 102. Same as Figure 65 but for Reticulum III.

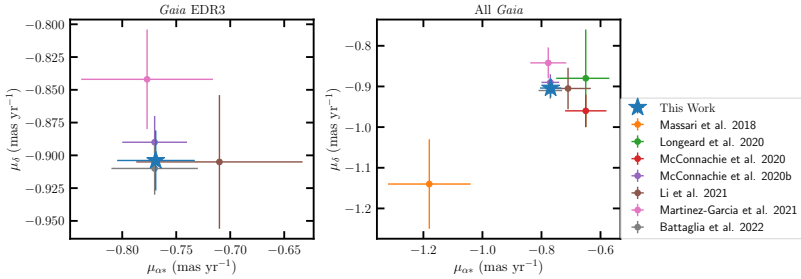


Figure 103. Same as Figure 65 but for Sagittarius II.

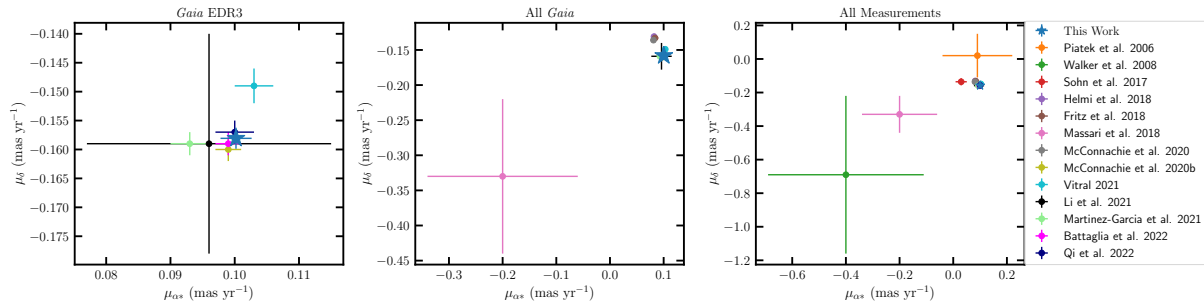


Figure 104. Same as Figure 65 but for Sculptor.

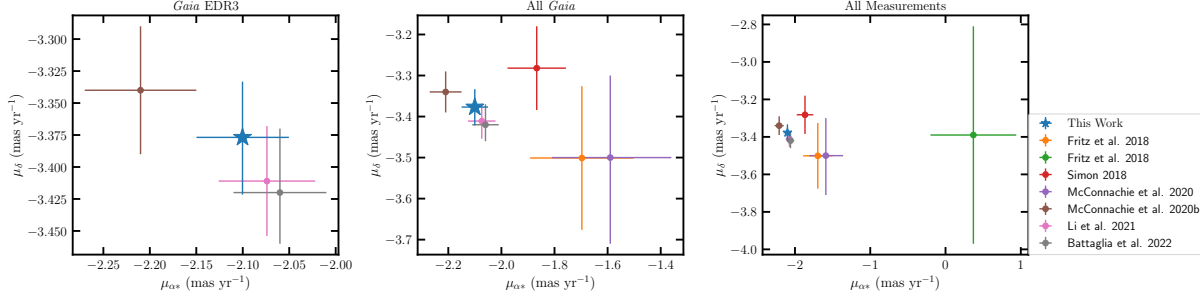


Figure 105. Same as Figure 65 but for Segue 1.

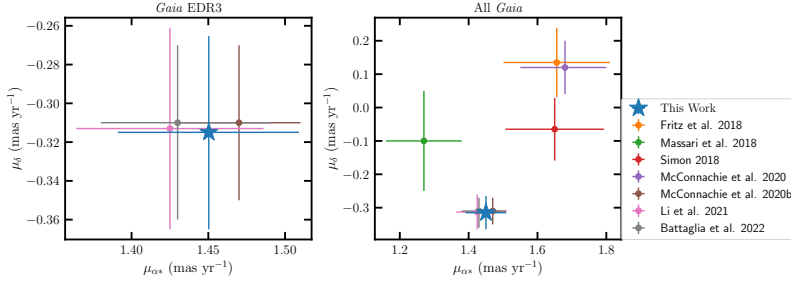


Figure 106. Same as Figure 65 but for Segue 2.

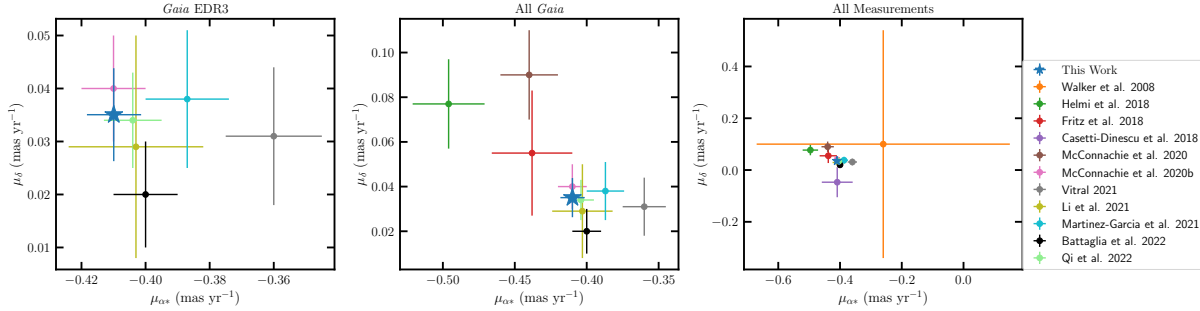


Figure 107. Same as Figure 65 but for Sextans.

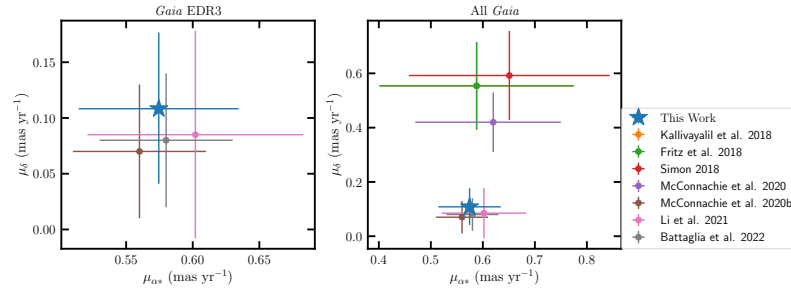


Figure 108. Same as Figure 65 but for Triangulum II.

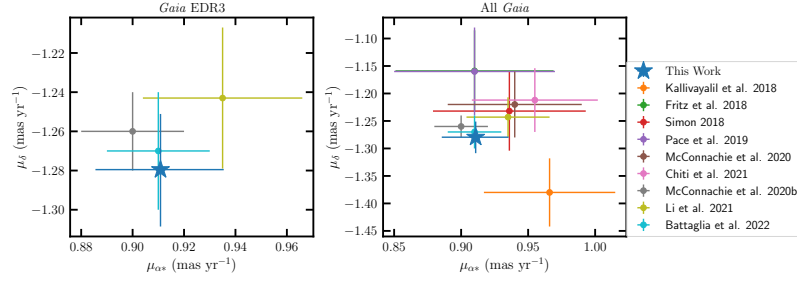


Figure 109. Same as Figure 65 but for Tucana II.

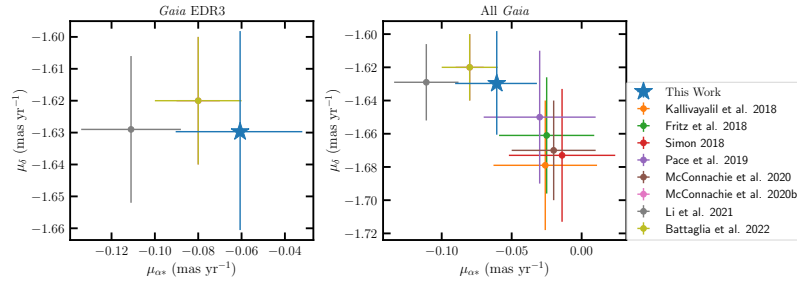


Figure 110. Same as Figure 65 but for Tucana III.

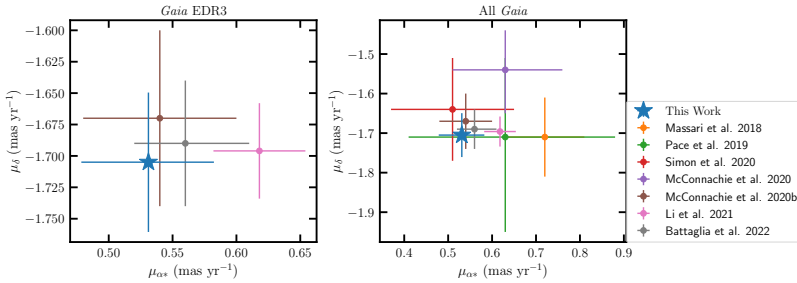


Figure 111. Same as Figure 65 but for Tucana IV.

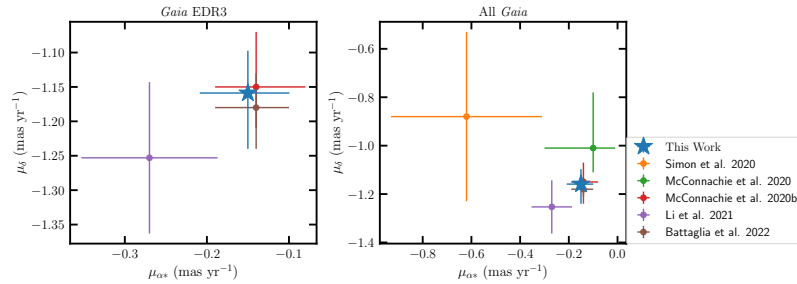


Figure 112. Same as Figure 65 but for Tucana V.

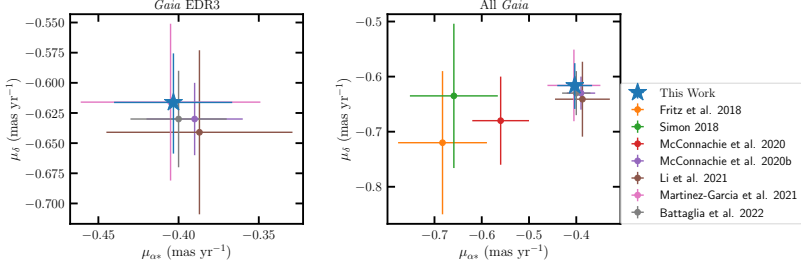


Figure 113. Same as Figure 65 but for Ursa Major I.

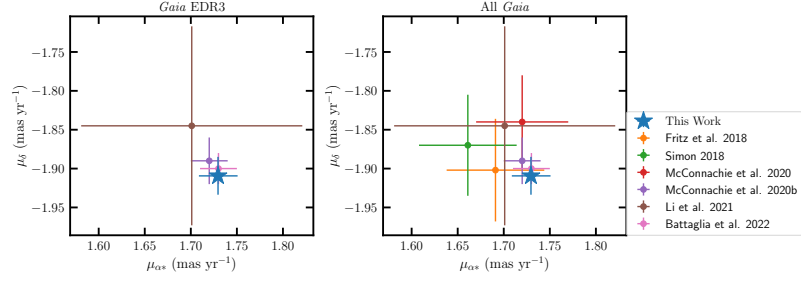


Figure 114. Same as Figure 65 but for Ursa Major II.

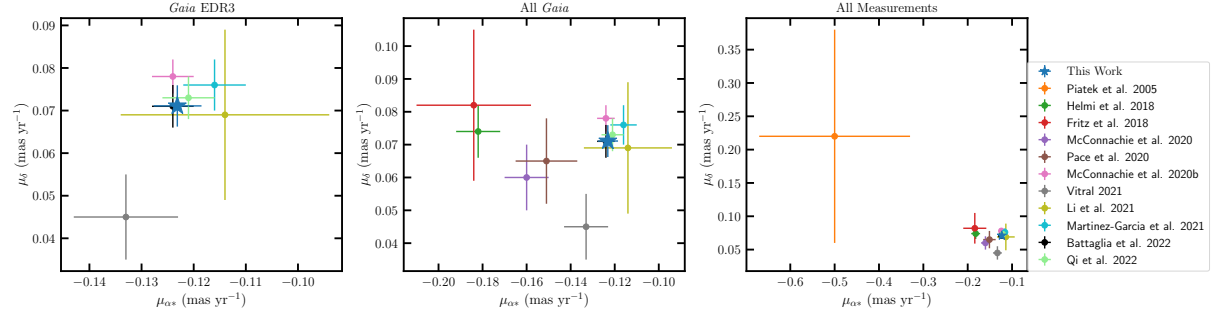


Figure 115. Same as Figure 65 but for Ursa Minor.

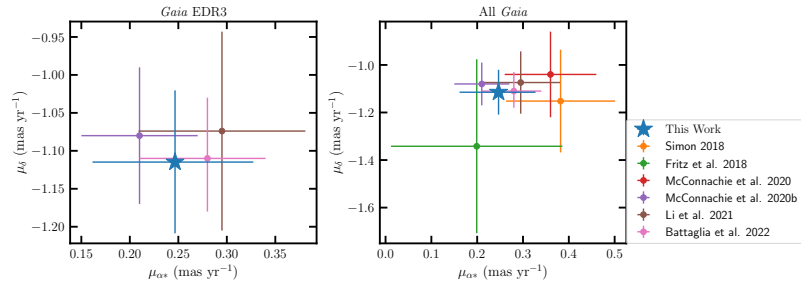


Figure 116. Same as Figure 65 but for Willman 1.